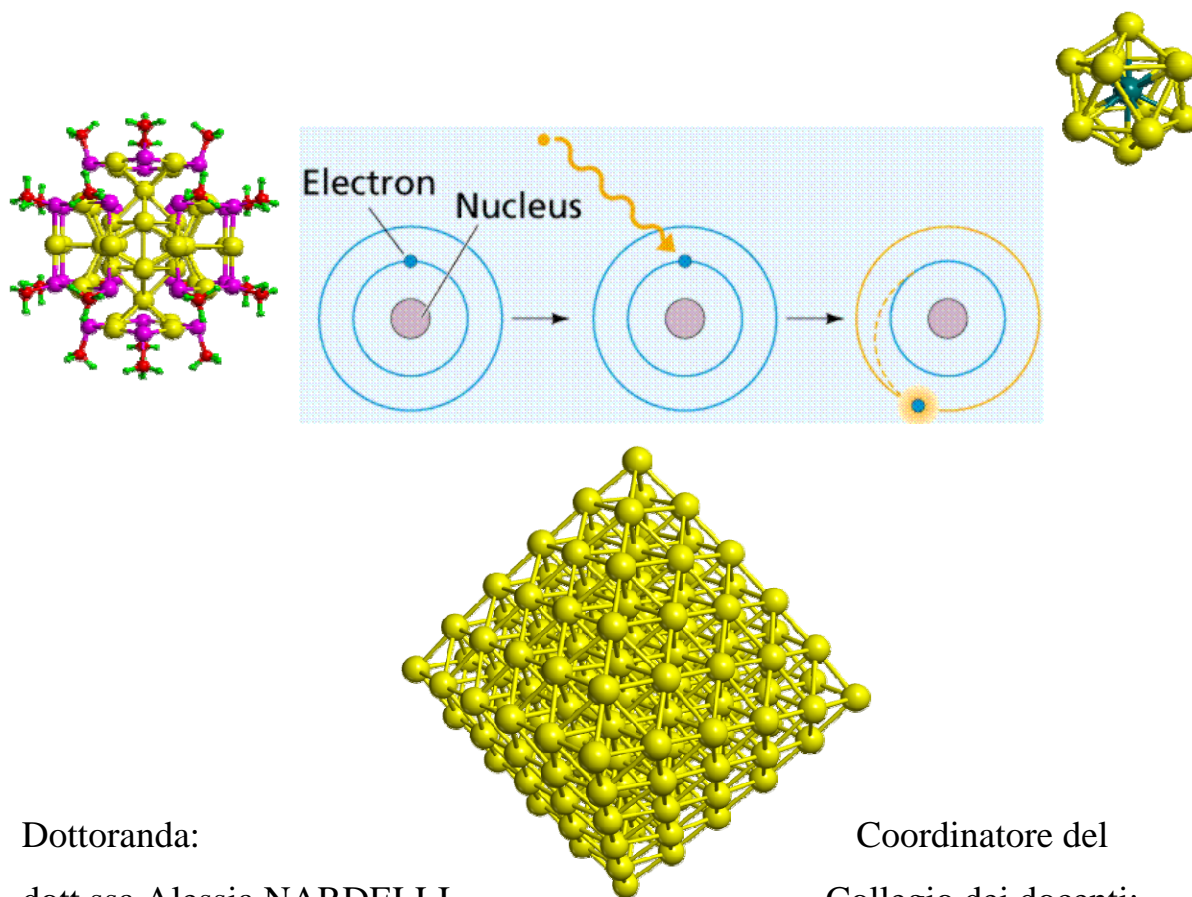




UNIVERSITÀ DEGLI STUDI DI TRIESTE

DOTTORATO DI RICERCA IN SCIENZE MOLECOLARI - XXI CICLO

Photoabsorption of gold nanoparticles: a TDDFT analysis by cluster model molecules



Dottoranda:
dott.ssa Alessia NARDELLI

Coordinatore del
Collegio dei docenti:
chiar.mo prof. Enzo ALESSIO

Relatore:
chiar.mo prof. Mauro STENER

ANNO ACCADEMICO 2007/2008



UNIVERSITÀ DEGLI STUDI DI TRIESTE

XXI CICLO DEL DOTTORATO DI RICERCA IN SCIENZE MOLECOLARI
Settore scientifico-disciplinare CHIM/02 – CHIMICA FISICA

Photoabsorption of gold nanoparticles: a TDDFT analysis by cluster model molecules

Dottorando:

dott.ssa Alessia NARDELLI

Coordinatore del

Collegio dei docenti:

chiar.mo prof. Enzo ALESSIO

Relatore:

chiar.mo prof. Mauro STENER

ANNO ACCADEMICO 2007/2008

CONTENTS

Contents	I
Overview of the thesis	IV
Riassunto della tesi	VI
1. Gold nanoparticles	1
1.1. Properties of the nanosystems	1
1.2. Optical properties: SPR bands	2
1.2.1. Theoretical studies and models	5
1.3. Functionalized gold clusters	6
1.4. Relativistic effects	8
1.4.1. Relativistic effects of gold	9
2. Electronic spectroscopy	12
2.1. General remarks	12
2.2. Absorption process	13
2.2.1. Electronic transitions: selection rules	15
2.3. Electronic excitations of nanosystems	16
2.4. XAS: general remarks	17
2.4.1. Theoretical approaches to XANES spectra	20
3. Theoretical method	22
3.1. DFT approach	22
3.2. TDDFT method	26
3.3. Computational aspects	29
3.4. Enhancement of the computational efficiency	31
3.4.1. Molecular symmetry	32
3.4.2. Basis sets	33
3.4.3. Frozen core approximation	33
3.4.4. Exchange-correlation potentials	34

3.5. SR and SO ZORA formalisms	36
3.5.1. SR ZORA	36
3.5.2. SO ZORA	37
4. Optical excitations of gold nanoparticles: a quantum chemical scalar relativistic Time Dependent Density Functional study	
Stener, M.; Nardelli, A.; De Francesco, R.; Fronzoni, G. <i>J. Phys. Chem. C</i> 2007 , <i>111</i> , 11862-11871	38
4.1. Introduction	38
4.2. Theoretical method	41
4.3. Computational details	42
4.4. Results and discussion	43
4.4.1. Au_6^{4+}	44
4.4.2. Au_{44}^{4+} and Au_{146}^{2+}	50
4.5. Conclusions	54
4.5.1. Acknowledgements	55
5. Spin-orbit effects in the photoabsorption of WAu_{12} and $MoAu_{12}$: a relativistic Time Dependent Density Functional study	
Stener, M.; Nardelli, A.; Fronzoni, G. <i>J. Chem. Phys.</i> 2008 , <i>128</i> , 134307	60
5.1. Introduction	60
5.2. Theoretical method	62
5.3. Computational details	63
5.4. Results and discussion	64
5.4.1. WAu_{12} electronic structure	64
5.4.2. WAu_{12} SR and SO TDDFT photoabsorption spectra	68
5.4.3. $MoAu_{12}$ electronic structure	72
5.4.4. $MoAu_{12}$ SR and SO TDDFT photoabsorption spectra	74
5.5. Conclusions	76
5.5.1. Acknowledgements	76
6. Theoretical study on the photoabsorption of MAu_{12}^- (M = V, Nb, Ta)	
Stener, M.; Nardelli, A.; Fronzoni, G., <i>Chem. Phys. Lett.</i> 2008 , <i>462</i> , 358–364	79
6.1. Introduction	79
6.2. Computational model	80

6.3. Results and discussion	81
6.3.1. Electronic structure	81
6.3.2. Photoabsorption spectra	84
6.3.3. Comparison with isoelectronic clusters $W_{Au_{12}}$ and $Mo_{Au_{12}}$	88
6.4. Conclusions	90
6.4.1. Acknowledgements	91
7. Theoretical study on the X-Ray absorption at the sulphur K-edge in gold nanoparticles	
Nardelli, A.; Fronzoni, G.; Stener, M. <i>J. Phys. Chem.</i> , 2009 , submitted	95
7.1. Introduction	95
7.2. Theoretical method	97
7.3. Computational details	98
7.4. Results and discussion	98
7.4.1. Model clusters	99
7.4.2. $[Au_{13}(SCH_3)_8]^{3+}$ S K-edge calculated XANES	100
7.4.3. $[Au_{25}(SCH_3)_{18}]^+$ (FCC1 isomer) S K-edge calculated XANES	103
7.4.4. $[Au_{25}(SCH_3)_{18}]^+$ (FCC2 isomer) S K-edge calculated XANES	104
7.4.5. $[Au_{14}[(AuSCH_3)_4]_6]^{2+}$ S K-edge calculated XANES	105
7.4.6. Comparison with experimental data	105
7.5. Conclusions	107
7.5.1. Acknowledgements	108
8. Conclusions	116
Bibliography	117

OVERVIEW OF THE THESIS

The optical properties of gold nanoparticles are the object of study of the present Ph. D. thesis. Different clusters in various conditions have been considered in order to simulate the absorption spectra at theoretical level and to correlate to the electronic structure the information obtained from the interpretation of the spectra. The study of electronic excitations has been carried out within the TDDFT theory implemented in the ADF code.

The gold nanoparticles have different and interesting physical and chemical properties and in the scientific community they have attracted great attention at both experimental and theoretical level. The properties for which they have been widely used, are mainly catalysis, absorption and selective oxidation, while those which are now being studied with increasing interest are optical, electronic and magnetic properties. Biology, biophysics and medicine are the applicative fields in which recently the gold nanoparticles have greater impact.

In order to contribute to the study of the optical properties of the gold nanoparticles, we have tried to propose theoretical models with the goal to rationalize the experimental findings and to realize a computational model for new nanostructured materials with specific optical properties. We have therefore addressed this issue by handling several aspects.

Below it will be described the path followed during the Ph. D. research indicating the chapters of the second part of the thesis in which the various arguments are treated in detail.

Starting with both experimental and theoretical data found in literature, we have focused at first on naked gold clusters, to simulate the note SPR absorption band ascribed to the electron collective oscillations. We have tried to push the size of the cluster to the maximum computationally allowed to reproduce the red-shift/size increasing trend, observed in the UV-visible spectra, and to draw as closely as possible to the minimum size of the systems synthesized in the laboratory. Within the limitations due to high density of states in the case of larger clusters, we have tried to rationalize the results in terms of conventional quantum chemistry arguments. (Chapter 4)

We have concentrated then on the refining of the computational technique, introducing the spin-orbit coupling in the calculation of valence excitation spectra of small regular icosahedral bimetallic systems with closed shell. In this context we have discussed the differences between a SR (Scalar relativistic) and a SO (spin-orbit) TDDFT calculation scheme and also those due to different heteroatoms present in the centre of the gold cage.

Thus, we have identified a diagonal trend between two elements of Group V B (V and Nb) and two from Group VI B (Mo and W) of the Periodic Table. (Chapters 5 and 6)

Finally we have moved to the study of the electronic excitation phenomena from the valence to the core, simulating the XANES spectra of systems functionalized with methylthiolate. The experimental molecular models that we have compared, were similar in size but different in composition (dodecanethiolate) and in structure. Nevertheless, grounded on calculations, we have given a more detailed interpretation of the intense experimental band: it is the result of two unresolved bands which involve both S-Au and S-C antibonding states. Moreover, depending on the structure of the cluster, and then the types of interactions present, we have observed changes in the spectral patterns. (Chapter 7)

In the first part of the thesis have been developed some general issues and some theoretical aspects with which deal the above chapters. In particular, in Chapter 1 is considered the wide nanoparticles main theme, in Chapter 2, the electronic spectroscopy and Chapter 3 the theoretical DFT and TDDFT methods with particular emphasis on aspects related to the relativistic formalism.

RIASSUNTO DELLA TESI

L'oggetto di studio della presente tesi di dottorato sono le proprietà ottiche di nanoparticelle d'oro. Diversi cluster in varie condizioni sono stati considerati al fine di simularne gli spettri di assorbimento a livello teorico e associare alle strutture elettroniche le informazioni ottenute dall'interpretazione degli spettri. Lo studio delle eccitazioni elettroniche è stato condotto a livello della teoria TDDFT implementata nel codice ADF.

Le nanoparticelle d'oro hanno proprietà fisiche e chimiche varie ed interessanti, quindi nella comunità scientifica hanno attratto grande attenzione sia a livello sperimentale che teorico. Le proprietà per le quali sono state ampiamente utilizzate sono soprattutto la catalisi, l'assorbimento e l'ossidazione selettiva, mentre quelle per le quali ora vengono studiate con sempre più interesse sono di tipo ottico, elettronico e magnetico. La biologia, la biofisica e la medicina sono i campi applicativi nei quali recentemente le nanoparticelle d'oro hanno avuto maggior impatto.

Al fine di dare un contributo allo studio delle proprietà ottiche delle nanoparticelle d'oro, noi abbiamo cercato di proporre schemi computazionali con lo scopo di razionalizzare i dati sperimentali e realizzare un modello possibilmente predittivo per nuovi materiali nanostrutturati con proprietà ottiche specifiche. Abbiamo, pertanto, affrontato questa tematica toccando più aspetti.

Di seguito verrà esposto il percorso di ricerca effettuato durante il dottorato indicando i capitoli della seconda parte della tesi nei quali i diversi argomenti vengono trattati in modo specifico.

Partendo da dati presenti in letteratura, sia sperimentali sia teorici, dapprima ci siamo concentrati su cluster "nudi" di oro, cercando di simulare la nota banda di assorbimento SPR attribuita ad oscillazioni elettroniche collettive. Abbiamo cercato di spingere le dimensioni dei cluster fino al massimo limite praticabile per riprodurre il trend red-shift/aumento di dimensioni, osservato negli spettri UV-visibile, e per avvicinarci il più possibile alle dimensioni minime dei sistemi sintetizzati in laboratorio. Con le limitazioni dovute all'alta densità degli stati nel caso dei cluster più grandi, abbiamo cercato di razionalizzare i risultati in termini di argomenti quantochimici convenzionali. (Capitolo 4)

Ci siamo poi concentrati sull'affinamento della tecnica computazionale, introducendo l'accoppiamento spin-orbita nel calcolo degli spettri di eccitazione di piccoli sistemi bimetallici icosaedrici regolari a guscio chiuso. In questo contesto abbiamo discusso le

differenze tra uno schema di calcolo TDDFT SR (Scalare Relativistico) e uno SO (Spin-Orbita) e anche quelle dovute ai diversi eteroatomi presenti al centro della gabbia di oro. Abbiamo potuto così individuare un andamento diagonale tra due elementi del gruppo V B (V e Nb) e due del gruppo VI B (Mo e W) della tavola periodica. (Capitoli 5 e 6)

Infine abbiamo spostato lo studio dei fenomeni di eccitazione degli elettroni dalla valenza al core, simulando gli spettri XANES di sistemi funzionalizzati con metiltiolati. I modelli molecolari sperimentali con i quali ci siamo confrontati erano analoghi per dimensione ma differenti per composizione (dodecantiolati) e struttura. Ciononostante, sulla base del calcolo, abbiamo dato un'interpretazione più dettagliata dell'intensa e allargata banda sperimentale: essa è il risultato di due bande non risolte nelle quali sono coinvolti orbitali antileganti di tipo S-Au e S-C. Inoltre, a seconda della struttura del cluster, e quindi dei tipi di interazioni presenti, si sono potuti osservare cambiamenti negli andamenti spettrali. (Capitolo 7)

Nella prima parte della tesi vengono sviluppati alcuni argomenti di carattere generale e alcuni aspetti teorici sui quali vertono i capitoli sopra illustrati. In particolare, nel Capitolo 1 viene inquadrata la vasta tematica delle nanoparticelle, nel Capitolo 2 la spettroscopia elettronica e nel Capitolo 3 i metodi teorici DFT e TDDFT con particolare attenzione per gli aspetti legati al formalismo relativistico.

1. GOLD NANOPARTICLES

1.1. PROPERTIES OF THE NANOSYSTEMS

Small clusters often have different physical and chemical properties than their bulk counterparts.^{1.1} In fact, in metal and semiconductor nanoparticles there are size-dependent properties, for example, electronic and optical phenomena such as single-electron charging and quantum size effects, fundamentally interesting and, in many cases, useful in technological applications.^{1.2} In most of their potential applications, the quality and the structure of the surface of nanoparticles will undoubtedly play the pivotal role in determining their functions. Being small could make the surface of a nanoparticle unstable due to the high surface energy and the large surface curvature. Thus, the properties change as these particles are used. Not only could the surface structure and shape change, but the chemical nature of their surface could be altered, too. In addition, for device applications, these nanoparticles need to be connected to our macroscopic world. The perturbation at interconnects could have larger effects on the properties of nanoparticles than quantum confinement or other physical forces involved within the nanoparticle space. Thus, it is clear that using these nanoparticles fully and effectively will depend on understanding of their general properties and also of their surface properties and stability.^{1.3} Transition metal nanoparticles, for example, are of special interest due in part to this fact: their optical properties differ substantially from those of the bulk metal. The optical responses of such clusters directly reflect their electronic structure, which is substantially dependent on the size and shape of the particle. Metal nanoparticles are important for fundamental studies,^{1.4} specially those pertaining to evolution of their properties with increasing particle dimension, ranging from molecular compounds to metals. Some applications that take advantages of the size-dependent properties of metal nanoparticle materials include catalysis, sensing and electronics. The metal nanoparticles with core diameters smaller than 1 nm are of considerable interest because they are small enough to possess discrete electronic states (and thus may exhibit electronic quantum confinement, useful for nanoelectronic, catalytic, or sensing applications) not found in larger particles.^{1.2} Therefore they can be used as building blocks for nanoscale devices because they can exhibit semiconductor-like electronic properties.^{1.4} One of the criteria for a cluster to be used as a potential building block for cluster-assembled materials is its chemical stability relative to other reagents and to other clusters of the same material. A common prerequisite, although

not general, for the chemical stability of a cluster is a closed shell electron configuration with a large energy gap between the Highest Occupied Molecular Orbital (HOMO) and the Lowest Unoccupied Molecular Orbital (LUMO). Gold is undoubtedly an important material, and small clusters of gold have also attracted great attention: it has been shown that gold clusters have unusual catalytic properties for selective oxidation of CO, are oxidation-resistant, enable selective binding of DNA, and have potential applications in nanoelectronics.^{1.1} The electronic structure of clusters is reflected directly by the optical response, because it strongly depends on the particle size and shape. Such nanostructured materials are produced and studied by many different techniques, as colloidal solution investigations, sol-gel or chemical synthesis, cosputtering, electrochemical deposition, ion implantation, electron-beam lithography, or low-energy cluster-beam deposition. The main feature in the optical response is the surface plasmon excitation.^{1.5}

1.2. OPTICAL PROPERTIES: SPR BANDS

As noble metals are reduced in size to tens of nanometers, a new very strong absorption is observed resulting from the collective oscillation of the electrons in the conduction band from one surface of the particle to the other. This oscillation has a frequency that absorbs the visible light and is called the surface plasmon absorption (SPR).^{1.3} For gold as well as for the other noble metals, the plasmon resonance occurs in the near-UV/visible region. It is therefore easier to perform the experimental optical study of such metal nanoparticles, and also interesting to use them for optical-device applications:^{1.5} both experimental results and theoretical calculations have indicated that the plasmonic absorption strongly depends on the detailed structure of the nanomaterials.^{1.6} The main features consist of a redshift and a damping of the plasmon resonance band with increasing cluster radius.^{1.5} Classically, the origin of this absorption is attributed to collective conduction band electron oscillation in response to the electrical field of the electromagnetic radiation of light. This optical absorption is termed surface plasmon, partly because net charges are displaced transiently on the particle surface during electron oscillation. This is illustrated in the Figure 1.1 (top) for spherical nanoparticles. When a particle is subject to an electromagnetic (EM) field, its electrons start to oscillate under resonant conditions, transforming energy from the incident EM wave into, for example, thermal energy in an absorption process.^{1.6}

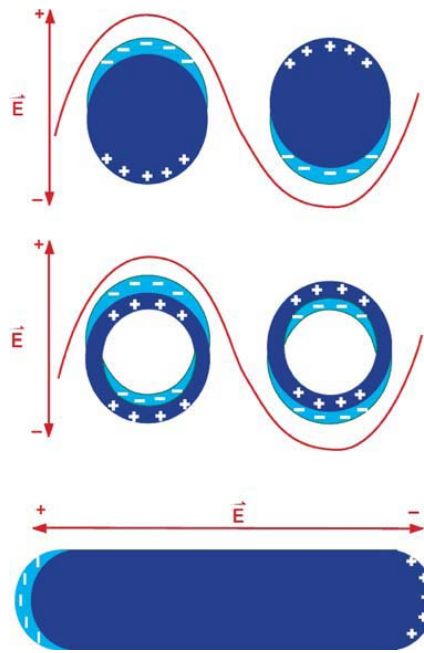


Figure 1.1 Schematic illustration of surface plasmon resonance in spherical nanoparticles (top), hollow nanospheres (middle), and nanorods (bottom) in a polarized light field. For the nanorod, only the longitudinal mode is shown. The transverse mode is essentially the same as in spherical nanoparticles. The lower the symmetry of the structure, the more nondegenerate modes there are. Both the solid spherical nanoparticles and hollow nanospheres have one resonance due to high symmetry. The nanorods with one symmetry axis have two nondegenerate modes. Complex structures such as strongly aggregated nanoparticles typically have multiple nondegenerate modes, resulting in broad plasmon absorption spectra.^{1,6}

By an incident radiation, the polarization of the electrons with respect to the much heavier ionic core of a spherical nanoparticle is induced by the electric field of the incoming light wave. In the simplest case, a dipolar oscillation of all the electrons with the same phase is created, as shown in the Figure 1.1:^{1,3} the electron cloud is displaced from the nuclei giving rise to a surface charge distribution. The Coulomb attraction between positive and negative charges results in restoring forces, characterized by oscillation frequencies of the electron cloud with respect to the positive background. Each collective oscillation associated to different surface charge distributions is known as SPR. The electron density, particle shape, size, dielectric function, and its environment determine the number, frequency, and width of SPRs.

As the colour as well surface plasmon absorption band is somewhat dependent on the size and on the shape of the nanostructures. For a metal such as gold, almost any colour or absorption in any part of the visible spectrum can be produced by controlling the shape or structure of the nanomaterial. The different-shaped nanostructures possess vastly different absorption spectra or colours. The rich colour or diverse absorption is the result of multiple resonances in the

complex structures. The Figure 1.1 (middle and bottom) illustrates different resonance modes of electrons in hollow nanospheres and nanorod.

In metallic nanoparticles of less than 30 nm of diameter, where scattering processes are usually negligible, the particle only absorbs energy through the following mechanisms:

1. collective excitations of the “free” electrons, which give rise to surface modes or surface plasmon resonances that are determined by the particle shape, size, environment, and material composition;
2. electronic transitions of bound electrons from occupied to empty bulk bands of different indexes, also called interband transitions;
3. surface dispersion or scattering of the “free” electrons, when their mean free path is comparable to the dimension of the nanoparticles.

Only the first two are fundamental absorption mechanisms. In contrast, surface scattering is one of several mechanisms for dissipating energy already absorbed by the first process, plasmon excitation. It should be recalled that bound electrons do not participate in the collective motion of the electron cloud; thus, the bound electron transitions contribute hardly anything to the origin of the SPRs. Furthermore, surface dispersion effects do not change the location of the SPRs but make the absorption spectrum wider and less intense since they affect the coupling of the proper modes to the applied field. Scattering effects become important only for nanoparticles of more than 30 nm in diameter, where electrons, accelerated due to the incident electromagnetic field, can radiate energy in all directions. This implies that, for larger particles, the resonance shifts to the red, decreases in magnitude, and is strongly broadened.^{1,6}

Noble metals such as copper, silver, and gold have a strong visible-light plasmon resonance, whereas most other transition metals show only a broad and poorly resolved absorption band in the ultraviolet region. This difference is attributed to the strong coupling between the plasmon transition and the interband excitation. In addition, the conduction band electrons of the noble metals can move freely, independently from the ionic background, and the ions act only as scattering centers. This gives the electrons in the noble metals a higher polarizability, which shifts the plasmon resonance to lower frequencies with a sharp bandwidth.

1.2.1. Theoretical studies and models

The surface plasmon resonance was theoretically explained by Mie in 1908, including linear optical properties such as extinction and scattering of small spherical metal particles. Mie's theory and experimental spectra agree well in the size regime > 20 nm until the normal incidence absorption no longer shows a plasmon resonance for bulk metals. Higher order modes become more dominant with increasing particle size, causing the plasmon absorption band to red shift and resulting in increased bandwidth, because for larger particles, the light cannot polarize the nanoparticles homogeneously and retardation effects lead to the excitation of higher order modes. But, when the size of nanoparticles is much smaller than the wavelength (< 20 nm) of the interacting light, this theory is contradicted with experimental results, because the plasmon band shows still a size dependence and even seems to disappear completely for nanoparticles of $< \sim 2$ nm. Thus, the Mie's theory is no longer valid in the size range below 2 nm. Very small nanoparticles are better treated as molecular clusters with discrete electronic states. Mie's theory for spherically shaped particles was extended also for cylindrical or oblate nanoparticles. The plasmon resonance for nanorods splits into two bands. As the aspect ratio increases (namely, it increases the length-to-width ratio of a nanoparticle), the energy separation between the resonance frequencies of the two plasmon bands also increases. The high energy band corresponds to the oscillation of the electrons perpendicular to the major axis of the rods and is referred to as the transverse plasmon absorption. The other absorption band, which is red-shifted to lower energies, is caused by the oscillation of the electrons along the major axis of the nanorods and is known as the longitudinal surface plasmon absorption.^{1,3}

In the present thesis we have considered as the first aspect the SPR of gold clusters, performing a theoretical computational model, to simulate the optical properties during the absorbing process of naked gold nanosystems of different size. Then we have examined also gold nanoparticles of different structure and geometry, to test out our computational model rationalizing experimental results found in the literature, hoping it can be used in the future as model for new nanostructured materials.

The Ph.D. study has been so developed:

1. in the first year have been considered three gold cluster in the same geometry but with different size. We have determined their electronic valence excitation energies and intensities to simulate the experimental optical response and the trends of the surface plasmon excitation, analyzing the nature of this absorptions;

2. in the second year and in a part of the third we have dealt with bimetallic small clusters in the same geometry and with the same structure. They are formed by a heteroatom encapsulated in a gold icosahedral Au₁₂ cage. The innovation in this case has been the introduction of the spin-orbit coupling in the calculations of the electronic valence absorption. We have selected these systems because they were before theory predicted and subsequently laboratory produced, therefore we had all the structural parameters and experimental results for a direct comparison. It has to be specified that the first isoelectronic systems studied are neutral, while the second group consists in three anionic nanoparticles structures;
3. the last efforts have been focused on the functionalized gold nanoparticles, in particular by methylthiolate ligands. Here we have dealt with the study of electronic excitations of core sulphur atoms, because interesting experimental spectroscopic data regarding the sulphur K-edge XANES spectra are available in the literature.^{1.7}

1.3. FUNCTIONALIZED GOLD CLUSTERS

It's worth paying attention to the functionalized gold clusters, because these are the nanosystems that are usually synthesized in the laboratories. One knows that the physical properties of nanoparticles are expected to be quite different from the bulk properties, because when the particle or cluster size is sufficiently small, degenerate energy levels split into discrete levels.^{1.8} Furthermore, monolayer-protected metal clusters (MPCs) provide significantly different physicochemical properties such as optical response, catalysis, and reactivity also from corresponding bare metal clusters.^{1.9} Until recently most of the studies employed metallic nanoparticles with core diameters greater than 1-2 nm, due, in some instance, to limited particle stability.^{1.2} Because of the difficulty of preparing samples with well-defined diameters, it has long been difficult to observe experimentally the differences among the various clusters. Of course, in the past two decades, a new class of materials, stabilized metal nanoclusters, have been extensively studied. In particular, noble metal nanoclusters have been synthesized using various stabilizer molecules,^{1.8} but the vast majority of the cluster capping ligands don't possess the functionality necessary to organize the particles through functional group directed assembly.^{1.2} Small (< 100 atoms) gold clusters protected by organic ligands have aroused interest as prototypical systems for fundamental studies on quantum size effects and as a building block of nanoscale devices. Conventionally,

phosphines have been used to stabilize gold clusters.^{1,10} Recently, a size adjustment method for noble metal (Pd, Pt, Au) nanoparticles embedded in linear alkyl chain polymers has been developed. This method ensures the generation of monodispersed metal nanoparticles with arbitrary diameter. So a wide range of particle diameters can be achieved, with a very small variance in the diameter. The ability of this method to adjust the cluster size allows a systematic investigation of the physical properties of metal clusters in the nanometer size range.^{1,8} Thiolates (RS) are another class of ligands that have been used extensively since the first report by Schiffrin.^{1,10} The thiolate groups have a strong affinity to a number of metals and have an ability to bridge two or more metal atoms. Accordingly, nanometer-sized metal-thiolate clusters show characteristic electronic structures and properties, which are strongly related to the nature of the clusters. Therefore, such metal-thiolate clusters have high potentialities for creating a new class of nanoparticle science and technology.^{1,9} The thiolated gold clusters are, in fact, of increasing importance in the rapidly growing area of nanotechnology because they are expected to be one of the prototypes of molecular-sized materials which might function as optical devices, electrical junctions, and chemical sensors.^{1,11} Several research groups have recently synthesized Au:SR clusters with well-defined chemical compositions, such as Au₂₅(SR)₁₈, Au₃₈(SR)₂₄, and Au₅₅(SR)₃₂, using size-separation techniques in combination with mass spectrometry. Nevertheless, geometric structures of Au:SR have not been determined experimentally mainly owing to the unavailability of single crystals of these compounds. The lack of structural information for small Au:SR clusters hinders a full understanding of the origin of their stability and novel properties (e.g., photoluminescence, magnetism, and optical activity).^{1,10} Very recently, it has been experimentally confirmed that Au₂₅(SG)₁₈ was unusually thermodynamically stable and chemically inert in comparison with the other Au-SG clusters (namely glutathione(GSH) protected gold clusters). The report of large-scale synthesis of Au₂₅(SG)₁₈ supports its extraordinarily high stability. It has been also found that the pattern of the absorption spectrum of Au₂₅(SG)₁₈ was rather insensitive to change of the ligand (SG) for other thiolate molecules, in sharp contrast to the other Au-SG clusters which showed ligand-sensitive absorption spectra. These experimental observations imply the existence of a characteristic Au₂₅S₁₈ framework.^{1,11} The interplay of structure and electronic properties of nanostructures is of paramount importance to the advancement of nanoscience and nanotechnology. In the nanoregime, two important factors come into play. One is the quantum confinement of the electrons, the size effect; the other is the increasing contribution of surface atoms, the surface effect. The surface atom to bulk atom ratio increases dramatically as the particles size

decreases (e.g., in a 2.5 nm particle, ~25% of all the atoms are on the surface). Both the quantum-size and the surface effects result in the electron redistribution (e.g., *s-d* rehybridization in *d*-band metals) of all nanoparticle atoms.^{1,12} XANES (X-ray Absorption Near Edge Structure) measurements of bulk Au has revealed features related to the existence of a small amount of itinerant holes at the *d* band caused by *s-p-d* levels hybridization. In gold nanoparticles, a noticeable lattice contraction due to size effect has been observed and reported. The decrease of Au interatomic distances yields enhancement of *d-d* electron interactions in such a way that the number of *d* holes decreases respect to that of bulk Au. It has been also shown that in gold nanoparticles capped with strong interacting thiols, the number of holes in the *5d* band increases. Therefore, in thiol-capped gold nanoparticles the counterbalance between size effect and ligand effect tunes the structure and the total number of *d* holes.^{1,13} Furthermore, since nanoparticle minimizes its surface energy, this behaviour leads to stability issues that are critical to the controlled fabrication of monodispersed nanoparticless.^{1,12} From the viewpoint of a theoretical study, it is necessary to fully understand electronic structures and properties of those clusters with a special emphasis on describing metal-ligand interactions.^{1,9} The purpose of our study has been to employ a series of model clusters, attempting to elucidate the XANES S K-edge of the nanoparticles by performing time-dependent density functional calculations.

1.4. RELATIVISTIC EFFECTS

It was long believed that valence electrons important for chemical reactions move rather slowly compared to the velocity of light ($v \ll c$) and should therefore not show significant effects coming from special relativity. In contrast, the importance of relativistic effects for inner K- or L-shell electrons of heavy elements was long recognized. Early Hartree calculations on closed shell Cu^+ however pointed towards the importance of relativistic effects in the valence shell and in the early seventies of the last century, as a result of the pioneering work of Pekka Pyykkö and Jean-Paul Desclaux, the importance of relativistic effects in the quantum chemical treatment of heavy element containing compounds became apparent and widely accepted.^{1,14} The atomic electronic structure of Cu, Ag, and Au, featuring a filled *d* shell and a singly occupied *s* shell [$nd^{10}(n+1)s^1$, with $n = 3, 4,$ and 5 for Cu, Ag, and Au], suggests that the properties of these metals could be treated to first approximation within a “simple metal” framework, that is, as s^1 -electron systems perturbed, with increasing

strength from Cu to Au, by the underlying filled *d* shell.^{1.15} However, the chemistry of heavy elements cannot be often understood without the inclusion of relativistic effects.^{1.14} Relativistic effects in chemistry can qualitatively be attributed to the high speeds of all electrons if they move near a heavy nucleus. The consequent mass increase will lead to an energetic stabilization and radial contraction. For the *s* and *p* orbitals this will be the main effect.^{1.16}

1.4.1. Relativistic effects of gold

The element gold has many “personalities”, of which the image of a noble but soft, yellow metal would first cross one’s mind. Thought to be noble, gold actually has a rich chemistry. Fascinating in its complexity for academic chemists, this chemistry has potential applications in materials science, medicine and, recently, in both heterogeneous and homogeneous catalysis. Some fresh promises are related to the optical properties of certain gold compounds or to the possibility of forming new nanostructures based on gold.

Gold is a unique element in that it has very large relativistic effects, larger than its neighbours, and larger than any other element with $Z < 100$.^{1.16} Neutral gold shows, in fact, an unusually large relativistic *6s*-orbital contraction compared to its neighboring atoms in the periodic table, resulting in a significantly increased ionization potential. This is now known as the “group 11 maximum of relativistic effects”. Because relativistic perturbation operators act in the vicinity of the nucleus where also valence *s*-electrons have a significant part of its density, and diffuse orbitals are more sensitive to relativistic perturbations than the more compact inner shell electrons, the *6s*-orbital of gold undergoes a rather large relativistic contraction (direct relativistic effect). Such effects roughly increase with the square of the nuclear charge Z . Because of the relativistic contraction of all *s*-shells, the nucleus becomes more screened resulting in a smaller effective nuclear charge, and the higher angular momentum orbitals expand (indirect relativistic effect). The third most important relativistic effect is spin-orbit coupling, which also increases roughly like Z^2 and becomes especially important for the *p*-block heavy elements. All three relativistic effects can be clearly seen when orbital energies are compared for the heavy elements. It is known since a long time that gold exhibits unusual features. Such anomalies down the group 11 elements have often been rationalized in terms of the lanthanide contraction. Early one-center expansion techniques applied to heavy element hydrides indicated that most of these unusual features in gold and its compounds can be traced back to relativistic effects.^{1.14} The lanthanide contraction (that is, the effect of filling the *4f*

shell on the subsequent $6s$ and $6p$ shells) works in the same direction as relativistic effects and is roughly comparable in size. If relativity is absent, it leads to a situation where the nonrelativistic (NR) $5d$ and $6s$ orbital energies of Au are similar to the $4d$ and $5s$ orbital energies of Ag, whereas the relativistic effects (R) are not. Thus the orbital-energy difference between silver and gold can be attributed to relativity and hence both lanthanide contraction and relativity are needed to reproduce the experimental trends down a column (i.e., a group of the periodic table).^{1,16} At theoretical level, different relativistic procedures currently in use are the Dirac equation or its two-component or scalar relativistically derived forms including relativistic pseudopotentials. One can observe how the atomic and molecular properties of gold change following the inclusion of relativistic effects. At atomic level, the relativistic valence s -contraction/stabilization results in an increase in both the first ionization potential (IP) and the electron affinity (EA). The (direct) relativistic stabilization of the $6s$ shell together with the (indirect) relativistic destabilization of the $5d$ shell leads to a substantially decreased $5d/6s$ gap. The strong relativistic $6s$ stabilization leads to a change in the electronic configuration from $^2S_{1/2} (d^{10}s^1)$ to $^2D_{5/2} (d^9s^2)$. Hence, d -participation in gold-ligand bonding becomes pronounced leading to the stabilization of the higher oxidation states +3 and +5. Because of the relativistic $6s$ -contraction the $6s$ shell becomes more compact and the (static dipole) polarizability decreases, but nonetheless the dispersive type of interactions between two gold units in compounds can increase substantially since it is in inverse proportion to r^6 and the Au–Au distance r decreases because of relativistic effects. At molecular level, as a result of the relativistic $6s$ contraction gold–ligand bond distances are shorter than expected.^{1,14} This contraction is able to pull in the Au-L (L=ligand) single-bond lengths to lengths similar to or less than those of the corresponding Ag-L bonds, and to simultaneously make the Au-L bond strengths larger than those of the corresponding Ag-L bonds.^{1,16} This is explained in terms of MOs: the stabilization of the $6s^1$ orbital and destabilization of the $5d^{10}$ ones brings them energetically closer determining, on one hand, an enhanced sd hybridization and, on the other hand, an increased overlap between the $5d$ orbitals of neighboring atoms. Consequently, in the relativistic clusters the molecular orbitals derived from the d electrons are more delocalized over the volume of the cluster and it is concomitant a significant shortening of the interatomic bond distances.^{1,15} This relativistic bond contraction is critically dependent on the occupancy of the gold $6s$ orbital: in fact, it is interesting that for the bulk $r_e(\text{Au}_\infty) \approx r_e(\text{Ag}_\infty)$ in contrast to the diatomic case. This indicates a reduced relativistic bond contraction for solid gold compared to Au_2 , which is not so easily understood.

In contrast to copper and silver, gold forms a wide range of different cluster compounds. Many of these gold clusters are unique in structure and chemical properties. Gold clusters are generally stabilized by phosphine ligands and the Au-Au bonding in such clusters is stabilized by relativistic effects. Properties of bare gold clusters in the gas phase have been studied intensively in the past. The available results emphasize that the chemistry and physics of gold cannot be understood without the inclusion of relativistic effects.^{1,14} According to such all motivations in our calculations we have employed a relativistic formalism to describe properly the electronic structure of gold compounds.

2. ELECTRONIC SPECTROSCOPY

2.1. GENERAL REMARKS

The spectroscopy is basically an experimental subject and it is concerned with the absorption, emission, or scattering of the electromagnetic radiation by atoms or molecules. Quantum mechanics, on the other hand, is a theoretical subject relating to many aspects of chemistry and physics, but particularly to the spectroscopy.

The optical signature of the nanoparticles is particularly interesting because the optical techniques are nondestructive, and with proper implementation, they can be used to perform measurements in situ and in real time, providing statistical properties of the whole sample. These attributes of the optical spectroscopies are important because the properties of nanoparticles depend on the environment and when the growth and the characterization are made in different conditions, the environment might be an additional uncontrollable variable for the optical interpretation. Thus, the optical spectroscopies can be used also as complementary tools of the structural characterization techniques like Atomic Force Microscopy (AFM), Scanning Tunneling Microscopy (STM), Transmission Electron Microscopy (TEM), etc., which provide the image of a small piece of the sample, giving information about local properties and characterizing few NPs at a time.^{2.1}

The electromagnetic radiation, as the name implies, contains both an electric and a magnetic component.

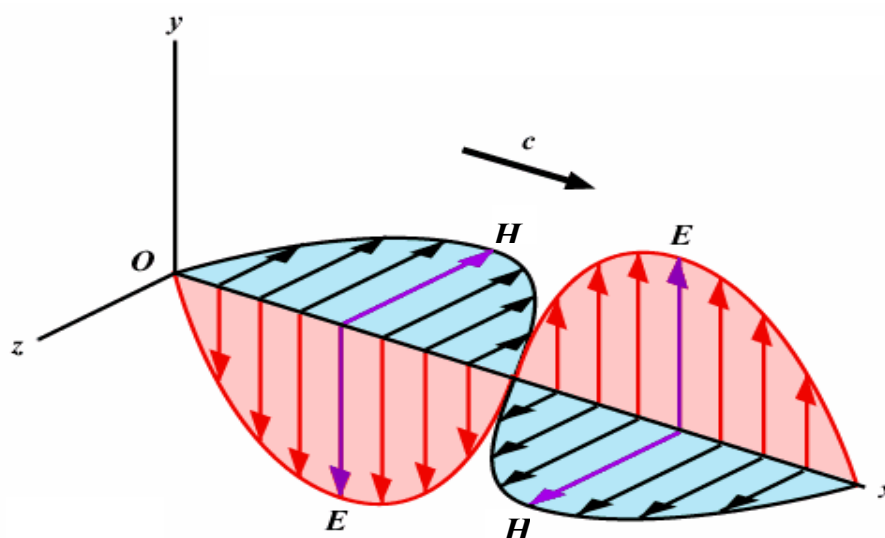


Figure 2.1 Plane polarized electromagnetic radiation propagating along the x axis. The electric field is confined to the xy plane and the magnetic field is confined to the xz plane

The electric component of the radiation is in the form of an oscillating electric field of strength E and the magnetic component is in the form of an oscillating magnetic field of strength H . These oscillating fields are orthogonal each other and the plane of polarization is conventionally taken to be the plane containing the direction of E and that of propagation, as shown in the Figure 2.1

2.2. ABSORPTION PROCESS

Since by our calculations on the examined gold nanosystems we have dealt with the absorption spectroscopy, we consider here the induced absorption process, when a generic system is subjected to a radiation of frequency ν . One attends an energy separation ΔE :

$$\Delta E = E_n - E_m = h\nu \quad (2.1)$$

with reference to the process indicated by the arrow 1 in the Figure 2.2, in which the molecule (or atom) M absorbs a quantum of the radiation and it is excited from the state m to the state n :

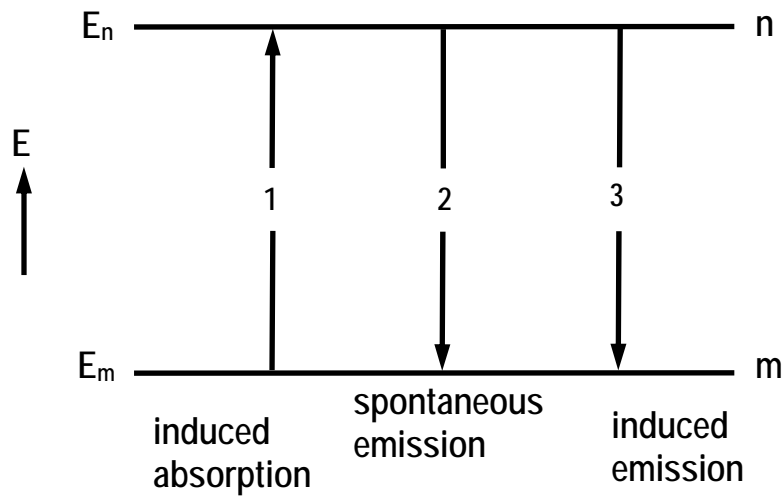


Figure 2.2 Absorption and emission processes between states m and n .

The rate of change of population N_n of the state n due to induced absorption is given by

$$\frac{dN_n}{dt} = N_m B_{mn} \rho(\tilde{\nu}) \quad (2.3)$$

where B_{mn} is a so-called Einstein coefficient and $\rho(\tilde{\nu})$ the spectral radiation density.

The Einstein coefficients are related to the wave functions ψ_m and ψ_n of the combining states through the transition moment M^{mn} , a vector quantity given by

$$M^{mn} = \int \psi_m^* \boldsymbol{\mu} \psi_n d\tau \quad (2.4)$$

for interaction with the electric component of the radiation. The quantity $\boldsymbol{\mu}$ is the electric dipole moment operator

$$\boldsymbol{\mu} = \sum_i q_i \mathbf{r}_i \quad (2.5)$$

where q_i and \mathbf{r}_i are the charge and position vector of the i th particle (electron or nucleus). The transition moment can be thought of as the oscillating electric dipole moment due to the transition.

We are interested in the electronic absorption spectroscopy which is, in general, the study of the transitions between electronic states of an atom or molecule. In such a context it is important to distinguish between configuration and state. A configuration describes the way in which the electrons are distributed among various orbitals but a configuration may give rise to more than one state. Therefore in discussing orbitals and electronic states becomes almost essential the use of symmetry arguments for non-linear polyatomic molecules. In fact, the promotion of an electron from one orbital to another, in an electronic transition obeys symmetry selection rules. For this reason the orbitals used to describe the difference between two electronic states of a molecule must be MOs (Molecular Orbitals) which belong to symmetry species of the point group to which the molecule belongs.

2.2.1. Electronic transitions: selection rules

In a oscillating electromagnetic field the probability of a transition between two electronic states, initial and final, of a molecule is proportional to the square of the electronic transition moment M :

$$M_{if} = \int \psi_f \bar{\mu} \psi_i d\tau \quad (2.6)$$

In the case of a electronic transition this integral can be broken down in a part which depends on the nuclear coordinates and in one depending on the spin. The final expression is:

$$M_{if} = \int \psi_{vf} \psi_{vi} d\tau_n \underbrace{\int \psi_{ef} \bar{\mu}_e \psi_{ei} d\tau_e}_{\text{orbital selection rule}} \underbrace{\int \psi_{sf} \psi_{si} d\tau_s}_{\text{spin selection rule}} \quad (2.7)$$

So that a transition between two states can take place, it is obliged that the transition moment is non-zero. Then, the second integral gives the orbital selection rule, while the third gives that of spin.

The spin selection rule is

$$\Delta S = 0 \quad (2.8)$$

that is, it is forbidden any variation of the spin state.

The orbital selection rule, instead, demands that the direct product of the irreducible representations of the initial and final wave functions and of the transition moment contains the total symmetric representation of the molecule symmetry group:

$$\Gamma_f \otimes \Gamma_\mu \otimes \Gamma_i \supset \Gamma_{ts} \quad (2.9)$$

Actually, the transition moment has three components along the three cartesian axes

$$|M_{if}|^2 = (M_{if,x})^2 + (M_{if,y})^2 + (M_{if,z})^2 \quad (2.10)$$

where, for example

$$M_{if,x} = \int \psi_f \bar{\mu}_x \psi_i d\tau \quad (2.11)$$

Then it is sufficient that any of $M_{if,x}$, $M_{if,y}$ or $M_{if,z}$ is non-zero, that is, for example

$$\Gamma_f \otimes \Gamma_{\mu,x} \otimes \Gamma_i \supset \Gamma_{ts} \quad (2.12)$$

Fortunately, there is also a simplification: if the direct product of two symmetric species is totally symmetric, then those species must be the same. In other words, when $\Gamma_f \otimes \Gamma_i = \Gamma_{\mu,x}$, their direct product is totally symmetric. A further simplification is the case of the lower state corresponding to the ground state: the latter has only filled orbitals, therefore, it is totally symmetric. For example, it is sufficient that $\Gamma_f = \Gamma_{\mu,x}$.^{2,2}

2.3. ELECTRONIC EXCITATIONS OF NANOSYSTEMS

In the last years, light-matter interactions at the nanoscale are receiving a great deal of attention because of their fundamental/cognitive and applied/technological interest. The last decade has witnessed a significant progress in experimental and theoretical studies of optical properties of nanostructures. The goal of the theoretical studies is to provide interpretation of the experimental data and to suggest new systems with potentially useful applications. TDDFT theory is one among the state-of-the-art techniques that have been employed successfully to compute optical excitations in nanostructures. Many nanostructures, in which the d electrons may play a significant role in the optical excitations, are of practical interest. Computationally, these pose extra challenges because inclusion of the d electrons requires utilization of larger basis sets. Although some physical and chemical properties of group IB noble metal (Cu, Ag, Au) systems can be explained qualitatively by invoking only the single valence s electron of the atoms, the close proximity of the filled d shells may and, in fact does, have important implications regarding their structural, electronic, and optical properties. At the subnanometer and nanometer scales, these implications can be magnified due to the extra coupling between the different properties. For example, the geometric structure of the systems plays an important role in defining their electronic and optical features.^{2,3}

The absorption spectroscopy at electronic level can be divided essentially in two type: of the valence and of the core, depending on the excitation induced by the radiation interests the core or the valence electrons, respectively. Schematically:

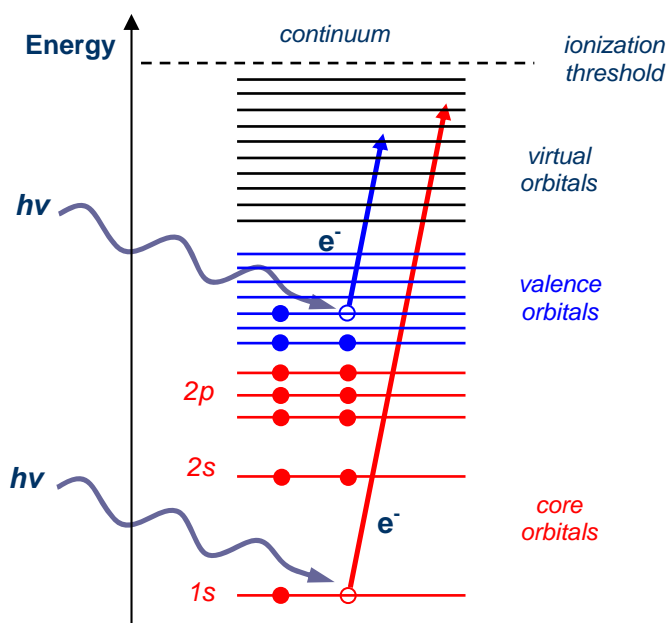


Figure 2.3 The absorption phenomenon. A photon can be absorbed either a core-level electron or a valence-level electron. In both cases the electron is promoted to bound unoccupied below-edge states.

During the Ph.D. we have dealt with both spectroscopies, but here following it will be shortly illustrated the core spectroscopy.

2.4. XAS: GENERAL REMARKS

X-ray Absorption Spectroscopy (XAS) is a local process and then it constitutes a powerful tool for the achievement of both electronic and structural information in particular selected sites in complex systems. In visible and UV spectroscopy electrons are promoted from the occupied valence MOs into the unoccupied MOs, whereas the more strongly bound core electrons can only be promoted with X-rays, which have much higher energies. Then, XAS spectra yield information about a whole series unoccupied MOs below (and sometimes also above) the ionization limit, and hence also about the overall structure of the molecule. In XAS spectra adverse to UV-spectra the lines are discrete, that is the transitions from different starting core levels don't overlap, because the energies of the core levels are generally far apart. Furthermore, the interaction of the low-lying hole state produced by the X-ray

excitation with the excited electron is relatively small and can be disregarded or taken into account easily by perturbation theory.^{2.4} When the incident X-ray photon energy is equal to the binding energy of a core electron of the sample, a sharp rise in absorption is observed, called absorption edge, corresponding to the ejection of this core electron into the continuum (photoelectric effect). Experimentally, the sample is irradiated by X-rays of variable frequency and it is measured the entity of absorption, that is the ratio between the number of electrons excited in the time unit and the number of photons absorbed in the time and area units. At determined energy values one observes a net increase of the absorption (absorption edge), which depends on the bound energy of excited core level (K, L, M...), namely on the energy necessary to produce a determined photoelectron.

A X-ray absorption spectrum is commonly divided into three regions, depending on the photon energy and following on the distinct interpretation of the spectral features and on the kind of information they can provide:^{2.5}

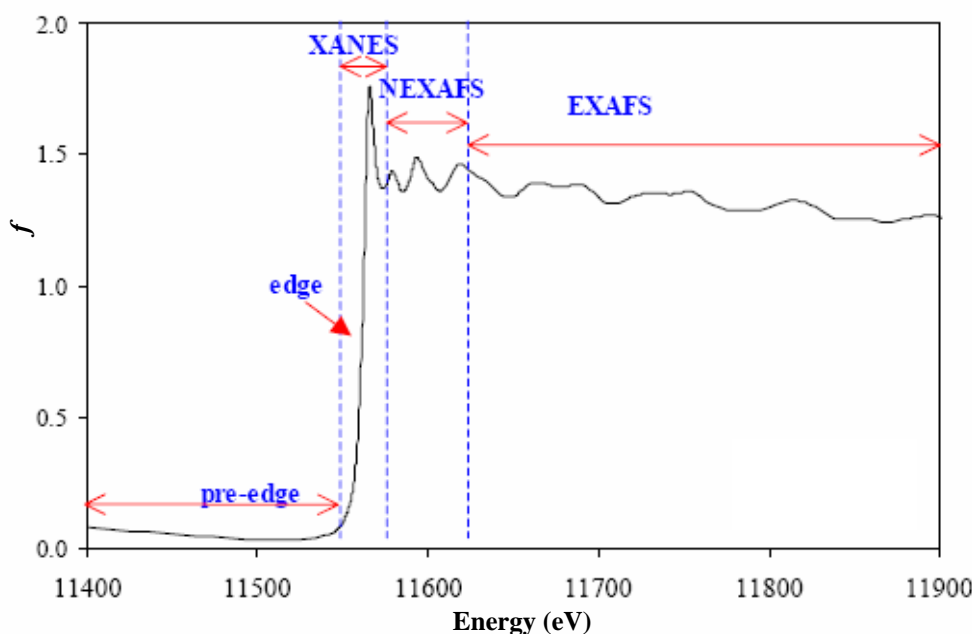


Figure 2.4 X-ray absorption spectrum and the regions in which it can be approximately divided In practice there is not an obvious division of these regions and the XANES and NEXAFS regions are often modelled together.

1. pre-edge with $E < E_0$ (where E_0 is the energy absorption edge)

The spectral structures result usually from transitions from the core levels to bound or semi-bound orbitals. One obtains information about:

- local geometry around the absorbing atom
- oxidation state and characteristics of the bonds

2. XANES and/or NEXAFS with $E_0 - 10 \text{ eV} < E < E_0 + 50 \text{ eV}$

(X-ray Absorption Near Edge Structure ; Near Edge X-ray Absorption Fine Structure)

Here there are transitions from the core to non-bound levels with energies near those of the edge. The probability of these transitions is high, then the absorption is rather intense. In particular, the absorption-edge give a very intense peak because very high is the probability that the electron is removed. Actually, the first non-bound levels have the characteristics of those bound, because also they depend on the geometric structure and on the particular bond situation. The acronyms XANES and NEXAFS should be interchangeable, even of over the years NEXAFS has become the main terminology for low-Z molecules absorbed on surface,^{2,6} while the term XANES has been more often employed for solids and inorganic complexes.^{2,7} Currently NEXAFS is by far the most used terminology, and the term XANES indicate rather the lower NEXAFS region, but since we have dealt with clusters experimentally investigated by XANES spectroscopy, in the thesis the latter term will be used. Then, at such energies one can recognize two regions:

– edge or XANES or low NEXAFS

The physical origin of the absorption features in the edge region is different in different classes of materials: Rydberg states (orbitals with principle quantum number larger than any bound orbitals of the ground-state) in atoms, bound valence states (or bound multiple-scattering resonances) in molecules, core excitations in ionic crystals, many-body singularities in metals, bond atom-like localized excitation in solids.^{2,8} The position and the intensity of these structures give information about:

- symmetry of the absorbing site
- oxidation state
- nature of the ligands and of the bonds

– NEXAFS or multiple scattering

The transitions concern all the unoccupied states from the Fermi level up to the EXAFS limit. The features of this high energy region are essentially explained by means of multiple-scattering resonances (with large cross sections) of the photoelectrons ejected at low kinetic energy. Here the interactions between electrons and atoms are very strong: in the language of the scattering theory, already at low energy the scattering of electrons is so strong that the wave function of the final state near the absorbing atom depends largely on the way

in which the electron is multiple scattered. Then, the analysis of such oscillations is extreme susceptible to the spatial arrangements of the atoms near that absorbing and can give information about:

- non-occupied orbitals
- electronic configuration
- symmetry site of the absorbing atom, bond distances and bond angles with the other atoms.^{2,7}

3. EXAFS with $E_0 + 50 \text{ eV} < E < E_0 + 1000 \text{ eV}$

(Extended X-ray Absorption Fine Structure)

The energies in this region are so high that the core electrons reach the delocalized states of the continuum, as well sensitive to the environment of the absorbing atom. The EXAFS is due to the single scattering of the ejected photoelectron, which now has a very high kinetic energy, so this part of the XAS spectrum permits the determination of:

- interatomic distances
- coordination numbers
- species of neighbors surrounding the absorbing atom.

2.4.1. Theoretical approaches to XANES spectra

XANES is a much larger signal than EXAFS, so it can be measured at lower concentrations and at less-than-perfect sample conditions; furthermore, it is one of the few non-destructive structural probes available for non-crystalline and highly disordered materials, including solutions and complex systems. However, XANES is considerably harder to fully interpret than EXAFS, mainly due to the difficulty to calculate both the pre-edge and post-edge energy regions where the excited electron is resonantly scattered by the surrounding atoms in the molecules.^{2,5}

The core spectroscopy is extremely useful for a punctual analysis, since the core electrons to be excited are situated very close to the nucleus^{2,4} and so they are essentially the same as in free atoms.^{2,7} The influence of the chemical environment on this core AO largely depends on the absolute strength and the symmetry of the field produced in the vicinity of the nucleus by the directly bonded atoms.^{2,4}

Precise and accurate calculations are mandatory for a correct and non-ambiguous interpretation of the spectral features. The theoretical description of XANES spectra, at least

of the pre-edge region, can be made through the one-electron model.^{2,7} That is each near-edge absorption structure can be investigated in terms of discrete transitions of the core electron into the unoccupied orbitals of the molecule characterized by well defined excitation energies and oscillator strengths.^{2,5} From the theoretical point of view the X-ray absorption transition rate depends on a matrix element between the initial and the final states of the many-electron system. To construct these states one would have to solve the many-electron Schrödinger equation, and this is, of course, not a practical scheme. The one-electron approximation represents the many-particle wave functions as products of single-particle wave functions, which are eigenfunctions of an effective one-electron Hamiltonian. In order to observe the absorption phenomenon, the transition moment must be non-zero, namely the orbital and spin selection rules must be respected:

- $\Delta L = \pm 1$ namely $s \rightarrow p$; $p \rightarrow d$; $p \rightarrow s$
- $\Delta J = \pm 1$
- $\Delta S = 0$

So, for example, for the K edge ($1s$ core electron) the primary transitions are $s \rightarrow p$ (the only dipole-allowed ones). In other words, a K edge XANES spectrum maps the atomic np content of the absorbing atom in the unoccupied electronic states.

Following an absorption event, the atom is said to be in an excited state, with one of the core electron levels left empty: a core hole has been created. It can be important to take into account the so-called relaxation effect, that is the modification of the molecular orbitals following the core-hole creation. From a theoretical point of view, different strategies can be introduced in order to include relaxation effects and therefore to obtain more correct values for the calculated ionization thresholds and excitation energies.^{2,5}

3. THEORETICAL METHOD

3.1. DFT APPROACH

The absorption structures in a spectrum can be investigated at theoretical level in terms of discrete below edge transitions of the electron into the unoccupied orbitals of the molecule characterized by well defined excitation energies and oscillator strengths, and of continuum transitions which generate the photoionization cross section profiles above the ionization limit.

The starting point for a quantum mechanical calculation on an N -particle system is the Schrödinger equation:

$$H\Psi(\mathbf{r}_1, \mathbf{r}_2, \dots, \mathbf{r}_N) = E\Psi(\mathbf{r}_1, \mathbf{r}_2, \dots, \mathbf{r}_N) \quad (3.1)$$

The total wavefunction Ψ is very complicated, as it depends upon the coordinates of all particles (nuclei and electrons) in the system. The problem is reduced if the electronic motion is separated from the much slower nuclear motion, the so-called Born-Oppenheimer approximation. In this case, the problem reduces to the determination of the electronic wavefunction at fixed nuclear positions. Although easier than the original problem, this equation is still unsolvable and additional approximations are needed in order to obtain a solution. The approximation made in the Hartree-Fock (HF) theory is that the total electronic wavefunction can be written in the form a single Slater-determinant of N_{el} spin orbitals, where N_{el} is the number of electrons in the system. The orbitals are optimized so that the Hartree-Fock energy (E^{HF})

$$E^{\text{HF}} = \frac{\langle \Psi^{\text{HF}} | H | \Psi^{\text{HF}} \rangle}{\langle \Psi^{\text{HF}} | \Psi^{\text{HF}} \rangle} \quad (3.2)$$

is minimal, under the constraint that the orbitals remain orthonormal: the resulting orbitals are called the Hartree-Fock orbitals. The Hartree-Fock approach is called often SCF approach, because the self-consistent field equations have to be solved. Furthermore it provides a cheap and relatively simple *ab initio* approach for the calculation of electronic structures. The

Hartree-Fock approach neglects the *electron correlation*, being the correlation energy defined as the difference between the HF energy and exact energy, therefore many *ab initio* approaches have been formulated to include the *electron correlation*. On the other hand all these accurate *ab initio* approaches are very time consuming, forbidding the treatment of large molecules. Therefore there has been a wide-spread interest in Density Functional Theory (DFT) in the last decades. DFT provides a first principle approach in which correlation effects are approximately taken into account, while the computational efficiency is at least as good as for HF theory.^{3.1} It represents a very popular method in quantum chemistry, because it gives a good compromise between accuracy of the results and computational economy. DFT provides a variational principle which can be rigorously employed to describe the Ground State (GS) of electronic systems such as atoms, molecules and solids.^{3.2-3.4}

The key point of DFT is that it is not necessary to calculate the very complicated complete electronic wavefunction $\Psi_{el}(\mathbf{r}_1, \mathbf{r}_2, \dots, \mathbf{r}_N)$ for a full description of the system. In fact, it is sufficient the knowledge of the electron density, $\rho(\mathbf{r})$, a simple function of three spatial coordinates. Once the electron density is known, the external potential, and consequently the Hamiltonian of the system are in principle uniquely determined. The knowledge of Hamiltonian in its turn determines the total electronic wavefunction. Consequently, every quantum mechanical observable is a functional of the ground-state density.

For a system without external perturbations the cusps in the electronic density determine the positions of the nuclei, the gradients of the density at the nuclei their nuclear charges and the integrated density the total number of electrons in the system. For this system the Hamiltonian can be written down, but it isn't obvious how to generalize the argument to a system in an external potential.

The exact electron density is that density which minimizes the energy functional and it can be obtained from a variational principle which involves only the density.

Now consider a system of fictitious noninteracting particles, each particle moves in an effective local potential and let us require the density to be identical to the associated interacting particle real system: this potential is called Kohn-Sham (KS) potential (V_{KS}). It, then, can be subdivided in three parts:

1. the external potential (V_{ext}),^{3.1} that is the Coulomb field of the nuclei and external fields if present,^{3.5}
2. the Hartree potential from the Coulomb interaction with the electron cloud;
3. the exchange-correlation potential (V_{xc}), which is unknown.

$$V_{\text{KS}}(\mathbf{r}) = V_{\text{ext}}(\mathbf{r}) + \int \frac{\rho(\mathbf{r}')}{|\mathbf{r} - \mathbf{r}'|} d^3\mathbf{r}' + V_{\text{xc}}(\mathbf{r}) \quad (3.3)$$

The third part of Kohn-Sham potential (V_{xc}) is an unknown functional of the density and contains all the many-body exchange and correlation effects,^{3,1} due to non-classical interactions electron-electron.

In the effective field V_{KS} move the KS orbitals, eigenfunctions of the KS-equations:

$$\hat{H}_{\text{KS}}\varphi_i(\mathbf{r}) = \varepsilon_i \varphi_i(\mathbf{r}) \quad (3.4)$$

where the KS Hamiltonian is the following local operator:

$$\hat{H}_{\text{KS}} = -\frac{1}{2}\nabla^2 - \sum_i^{\text{nuclei}} \frac{Z_i}{|\mathbf{r}_i - \mathbf{r}|} + \int d\mathbf{r}' \frac{\rho(\mathbf{r}')}{|\mathbf{r} - \mathbf{r}'|} + V_{\text{xc}}[\rho](\mathbf{r}) \quad (3.5)$$

It is composed of, respectively, the kinetic energy, the nucleus-electron attraction, the Coulomb electron-electron classic repulsion (expressed in terms of the density $\rho(\mathbf{r})$) and the exchange-correlation potential.^{3,6}

The effective field V_{KS} depends upon the electron density $\rho(\mathbf{r})$. This density is exactly obtained by summing the squares of the Kohn-Sham orbitals and multiplying by their occupation numbers n_i and is a function of \mathbf{r} :

$$\rho(\mathbf{r}) = \sum_{i=1}^{\text{occ}} n_i |\varphi_i(\mathbf{r})|^2 \quad (3.6)$$

As the KS potential $V_{\text{KS}}(\mathbf{r})$ and the density $\rho(\mathbf{r})$ are interdependent, the equations have to be solved in a SCF scheme, which means that one iteratively adapts the effective potential V_{KS} and the density ρ until the difference in, for example, the energy between two subsequent cycles is sufficiently small.^{3,5} So, at the end, one obtains the molecular orbitals φ_i and the corresponding eigenvalues ε_i , representing the orbital energies.^{3,6}

The accuracy of DFT calculations largely depends on the appropriateness of the approximations made for the xc potential^{3,1} (which is a relatively small term with respect to the other contributions^{3,6}) and related xc functionals, such as the xc energy functional.

$$V_{xc}(\mathbf{r}) = \frac{\delta E_{xc}[\rho(\mathbf{r}')]]}{\delta \rho(\mathbf{r})} \quad (3.7)$$

The first approximation used for the xc potential was the Local Density Approximation (LDA), either in exchange-only form or with inclusion of correlation effects. The LDA is based upon the theory of the homogeneous electron gas. For this simple system the exchange energy and potential are known exactly, and accurate approximations for the correlation parts are known from analytical parametrizations.

$$E_{xc}[\rho(\mathbf{r}')] = \int \varepsilon_{xc}(\rho(\mathbf{r}')) \rho(\mathbf{r}') d^3 r' \quad (3.8)$$

where $\varepsilon_{xc}(\rho)$ is the exchange-correlation energy per particle of a static uniform electron gas of density ρ .^{3,7}

The approximation is that a system can locally be described as an electron gas with a density equal to the local density of the system. This assumption seems reliable in systems with slowly varying densities (such as certain metals), but not in molecules where the density changes rapidly. Another approximations are the Generalized Gradient Approximations (GGAs) that are based upon the theory of the (weakly) inhomogeneous electron gas and take the gradient of the density in addition to the density itself. Very good accuracy is reached for many systems and properties with the GGAs, although cases are known in which also these GGAs give qualitatively incorrect results, because the description of some effects requires an ultra-nonlocal density dependence in the functionals, for which a gradient expansion is insufficient.^{3,1} GGA allow a much improved accuracy in the results for energies and geometries.^{3,5}

The DFT method is rigorous only for the GS configuration, therefore in principle the treatment of electronic excited states is not justified but in some particular cases,^{3,2} however the KS scheme is suitable also for the description of excited states, in fact the occupation numbers (n_i) defining the density (see equation 3.6) can be properly selected to represent whichever mono-determinant electronic configuration, different from the GS. Although there is no theoretical justification for this procedure, the remarkable accuracy of the results represents a good reason for employing this pragmatic scheme. The simplest approach is the neglect of relaxation effects by means of a frozen-orbital assumption: excitation energies are simply calculated as the differences between the energy eigenvalues relative to the initial occupied level and the final virtual level:

$$\Delta E_{\text{in} \rightarrow \text{fin}} = \varepsilon_{\text{fin}} - \varepsilon_{\text{in}} \quad (3.9)$$

while the IP is directly obtained as the opposite eigenvalue of the initial level:

$$\text{IP}(i) = -\varepsilon_i \quad (3.10)$$

in other words this approximation assumes that, upon removal of an electron from some orbital φ_i , none of the other φ_k 's change, i.e. they remain frozen.

Although a great development is in progress to confer more formal validation to a DFT treatment of excited states,^{3,8,3.9} when dealing with electronic transitions, the most accurate theoretical approach has proven to be the Time-Dependent Density Functional Theory (TDDFT)

3.2. TDDFT METHOD

The application of the TDDFT method to the calculation of electronic excitations and its implementation in the ADF code is by now well-consolidated and largely described in the literature,^{3,10,3.5} so the main goal of this discussion is an overview of its fundamentals and also of extension to the core excitation,^{3.11} which has been recently inserted into the distributed ADF code (release 2005.01).

The starting point is the time-dependent Schrödinger equation:

$$i \frac{\partial}{\partial t} \Psi(t) = \hat{H}(t) \Psi(t) \quad (3.11)$$

The Hamiltonian \hat{H} consists of the kinetic energy \hat{T} , the Coulomb interaction \hat{W} and the time-dependent external potential $\hat{V}(t)$:

$$\hat{H}(t) = \hat{T} + \hat{W} + \hat{V}(t) \quad (3.12)$$

The external potential $\hat{V}(t)$ may consist of several external time-dependent potentials, each of which is required to be expandable in a Taylor series around the finite time t_0 . It is

demonstrable that the densities $\rho(\mathbf{r}, t)$ and $\rho'(\mathbf{r}, t)$ of two systems evolving from the same initial state $\Psi(t_0)$ under the influence of, respectively, the scalar potentials $V(\mathbf{r}, t)$ and $V'(\mathbf{r}, t)$, both Taylor expandable about t_0 and differing by more than a purely time-dependent function, will always differ.^{3.1} As a consequence, the time-dependent density determines the external potential uniquely up to within an additive purely time-dependent function. On the other hand, the potential uniquely determines the time-dependent wavefunction, which can therefore be considered as a functional of the time-dependent density:

$$\Psi(t) = \Psi[\rho](t) \quad (3.13)$$

where $\Psi[\rho]$ is unique up to within a purely time-dependent phase factor. As a consequence, the expectation value of any quantum mechanical operator $O[\rho](t)$ is a unique functional of the density:[34]^{3.7}

$$O[\rho](t) = \langle \Psi[\rho](t) | \hat{O}(t) | \Psi[\rho](t) \rangle \quad (3.14)$$

In TDDFT in order to arrive at a formal method for obtaining the electron density, a stationary action principle is required.

Solving the time-dependent Schrödinger equation at t_0 is equivalent to finding the stationary point of the quantum mechanical action integral

$$A = \int_{t_0}^n dt \left\langle \Psi(t) \left| i \frac{\partial}{\partial t} - \hat{H}(t) \right| \Psi(t) \right\rangle \quad (3.15)$$

which, in view of the correspondence between the time-dependent densities and wavefunctions, can be regarded as a density functional $A[\rho]$:

$$A[\rho(\mathbf{r}, t)] = \int_{t_0}^n dt \left\langle \Psi[\rho](t) \left| i \frac{\partial}{\partial t} - \hat{H}(t) \right| \Psi[\rho](t) \right\rangle \quad (3.16)$$

which must have a stationary point at the exact time-dependent density, corresponding to the Hamiltonian $\hat{H}(t)$ and the initial state $\Psi(t_0)$. The exact density can be found by solving the Euler equation:

$$\frac{\partial A[\rho]}{\partial \rho(\mathbf{r}, t)} = 0 \quad (3.17)$$

However this formalism isn't a practical algorithm, so a set of time-dependent KS equations has to be introduced. The treatment is the same viewed in the DFT, but with the addition of the time dependency. The time-dependent Kohn-Sham (KS) equations are:

$$\hat{H}_{\text{KS}}(t)\varphi_i(\mathbf{r}, t) = \varepsilon_i \varphi_i(\mathbf{r}, t) \quad (3.18)$$

$$i \frac{\partial}{\partial t} \varphi_i(\mathbf{r}, t) = \left(-\frac{\nabla^2}{2} + V_{\text{KS}}[\rho](\mathbf{r}, t) \right) \varphi_i(\mathbf{r}, t) \quad (3.19)$$

with the density obtained from the noninteracting orbitals:

$$\rho(\mathbf{r}, t) = \sum_{i=1}^N n_i |\varphi_i(\mathbf{r}, t)|^2 \quad (3.20)$$

The potential $V_{\text{KS}}(\mathbf{r}, t)$ is usually called the time-dependent KS potential and written as:

$$V_{\text{KS}}[\rho](\mathbf{r}, t) = V_{\text{ext}}(\mathbf{r}, t) + \int d^3 \mathbf{r}' \frac{\rho(\mathbf{r}', t)}{|\mathbf{r} - \mathbf{r}'|} + V_{\text{xc}}(\mathbf{r}, t) \quad (3.21)$$

$V_{\text{ext}}(\mathbf{r}, t)$ is the external field and $V_{\text{xc}}(\mathbf{r}, t)$ is the time-dependent exchange-correlation potential, the unknown part of $V_{\text{KS}}(\mathbf{r}, t)$, which has to be approximated for practical applications and which is related to the xc part A_{xc} of the action functional A by the relation:

$$V_{\text{xc}}[\rho](\mathbf{r}, t) = \frac{\partial A_{\text{xc}}[\rho]}{\partial \rho(\mathbf{r}, t)} \quad (3.22)$$

where A_{xc} is the xc part of the action functional.^{3,1}

The density functionals are well-defined only for densities that come from some time-dependent potential, so a number of extensions of the time-dependent density-functional formalism to physically different situations have been developed.^{3,7}

For the determination of properties like polarizabilities and excitation energies is required a perturbative solution to the time-dependent KS equations, starting from the ground-state. In

general, the first-order time-dependent density has to be calculated and it depends on the KS potential in first-order of external field which in its turn depends on the kernel xc (f_{xc}). f_{xc} is the functional derivative of the time-dependent xc potential $V_{xc}(\mathbf{r}, t)$, with respect to the time-dependent density $\rho(\mathbf{r}, t)$:

$$f_{xc}(\mathbf{r}, t; \mathbf{r}', t') = \frac{\partial V_{xc}(\mathbf{r}, t)}{\partial \rho(\mathbf{r}', t')} \quad (3.23)$$

Given some approximations for the exchange-correlation kernel f_{xc} , the KS equations for non-interacting system can be resolved, providing a selfconsistent scheme to calculate the first-order time-dependent density response. The knowledge of the latter is important because from it can be calculated the first-order density shift, which provides the frequency-dependent polarizability.^{3,7}

When a system is perturbed by a radiation with a given frequency, between two electronic states may occur a transition which has the same frequency of the radiation. When this happens the molecular property polarizability (α), defined as the tensor which relates the dipole electric moment (μ) with the external electric field (E)

$$\bar{\mu} = \alpha \bar{E} \quad (3.24)$$

explodes to infinite values: in fact, the frequency-dependent polarizability is directly related to (vertical) excitation energies, oscillator strengths and transition dipole moments.^{3,5}

3.3. COMPUTATIONAL ASPECTS

For a linear response polarizability calculation, it is useful to reduce the TDDFT formalism to one traditional KS in which the potential is time-independent and the initial state is the ground state of the potential:^{3,7} so it is enough to expand the KS equations to first order in the applied field and to consider the response due to a external perturbation δV . At an excitation energy, a finite external perturbation δV leads to the eigenvalue equation (3.25),^{3,5} whose resolution is the crucial point of the TDDFT method for the calculation of electronic excitations:

$$\Omega \mathbf{F}_i = \omega_i^2 \mathbf{F}_i \quad (3.25)$$

where the eigenvalues ω_i^2 are the squared excitation energies, while the oscillator strengths are properly extracted from the eigenvectors \mathbf{F}_i . The oscillator strengths,^{3,7} which determine the magnitudes of the peaks in an absorption spectrum,^{3,12} are calculated using the transition dipole integrals between the eigenfunctions corresponding respectively to the ground (Ψ_0) and the excited (Ψ_{exc}) state:

$$f_{\text{in} \rightarrow \text{fin}} = \frac{2}{3} \cdot \Delta E_{\text{in} \rightarrow \text{fin}} \cdot \left| \left\langle \Psi_0 \left| \hat{\mathbf{R}} \right| \Psi_{\text{exc}} \right\rangle \right|^2 \quad (3.26)$$

being $\hat{\mathbf{R}}$ the n-particle dipole operator.

The $\mathbf{\Omega}$ matrix, defined within the 1h-1p space, is a four-index matrix of elements $\Omega_{ia\sigma,jb\tau}$, in which the indexes i and j refer to KS occupied orbitals, a and b to KS virtual (unoccupied) orbitals, σ and τ to the spin variable; these matrix elements can be expressed in terms of the KS eigenvalues (ε):

$$\Omega_{ia\sigma,jb\tau} = \delta_{\sigma\tau} \delta_{ab} \delta_{ij} (\varepsilon_a - \varepsilon_i)^2 + 2\sqrt{(\varepsilon_a - \varepsilon_i)} K_{ia\sigma,jb\tau} \sqrt{(\varepsilon_b - \varepsilon_j)} \quad (3.27)$$

where the elements of the coupling matrix K are defined through the KS orbitals (φ):

$$K_{ia\sigma,jb\tau} = \int d\mathbf{r} \int d\mathbf{r}' \varphi_{i\sigma}(\mathbf{r}) \varphi_{a\sigma}(\mathbf{r}) \left[\frac{1}{|\mathbf{r} - \mathbf{r}'|} + f_{\text{xc}}^{\sigma\tau}(\mathbf{r}, \mathbf{r}', \omega) \right] \varphi_{j\tau}(\mathbf{r}') \varphi_{b\tau}(\mathbf{r}') \quad (3.28)$$

being $f_{\text{xc}}^{\sigma\tau}(\mathbf{r}, \mathbf{r}', \omega)$ the exchange-correlation kernel.^{3,13} Considering some elements, TDDFT response equations more simple can be obtained.^{3,5} At this level, the exchange-correlation kernel is commonly approximated in the ALDA (Adiabatic Local Density Approximation), which is a approximation local in time and space for $A_{\text{xc}}[\rho]$. In this way also the xc kernel f_{xc} is simplified,^{3,7} because it is nonzero only for $t = t'$ (that is only for slow time-dependent processes)^{3,5} and because it is independent of the frequency.^{3,13}

The monoexcited (1h-1p) configuration space is described by occupied-virtual couples of indexes (like ia or jb); since core excitations are to a very large extent decoupled from valence excitations, if the occupied index i is allowed to span only core orbitals, while no limitations are set for the virtual index a , all and only the core excitations are included. The restriction of the initial functions to only core orbitals brings a drastic reduction of the $\mathbf{\Omega}$ matrix

dimensions, through the suppression of rows and columns referring to non-core orbitals (thus obtaining a considerable computational save, see Figure 3.1). Such an implementation allows the calculation of excitation energies as the lowest eigenvalues of a given matrix, so that very efficient iterative procedures for the Ω matrix diagonalization (like the Davidson algorithm^{3,14}) can be opportunely employed. At this level the calculation of the valence excitations differ from that of core.^{3,6}

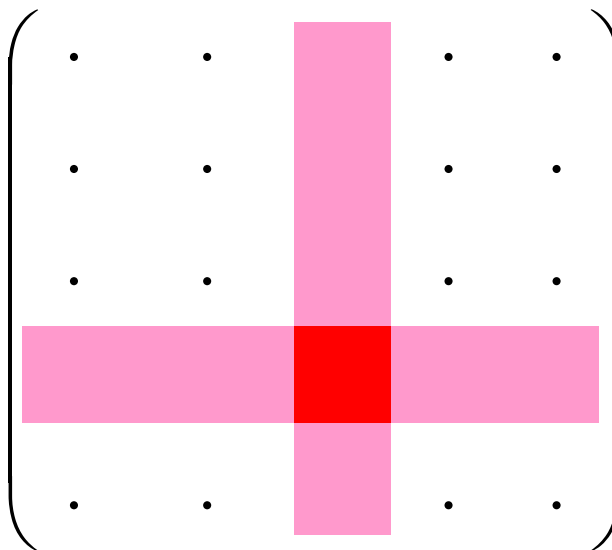


Figure 3.1 The core-valence decoupling allows a considerable reduction of the dimensions of the matrix to be diagonalized.

3.4. ENHANCEMENT OF THE COMPUTATIONAL EFFICIENCY

The TDDFT formalism implemented in the conventional quantum chemical Linear Combination of Atomic Orbital (LCAO) method joins the reliability of modern TDDFT approaches to describe electron excitations, with the accuracy of the LCAO implementation which avoids the drastic approximation of the effective molecular potential operated by other approaches (i.e. *jellium*). The LCAO-TDDFT method is computationally much more demanding than *jellium* methods; however, it represents the state-of-the-art approach for the theoretical description of the optical spectra for large molecules, and therefore, it is a potential tool to understand in detail the electron excitation process and a valid instrument to help the design of new nanoparticles with specific optical properties. To reduce the computational efforts, it is important to exploit the molecular symmetry and to set the requirements of the

TDDFT, namely the basis set size, the frozen core level of approximation and the exchange correlation potential choice, depending on the considered system.

ADF applies numerical integration not only to those integrals that cannot be done analytically, such as the matrix elements of the xc potential, but to most other integrals as well. This approach has two major advantages. In the first place, simplicity, and hence efficiency, as well as reduced chances of implementation errors. In the second place, it creates the freedom to select the types of basis functions that are intrinsically the most suitable for electronic structure calculations, but which might cause difficulties in analytical integration schemes, for instance Slater-Type Orbitals (STOs) or numerical atomic orbitals. It makes it almost trivial to implement the computation of all kinds of properties, as long as these are expressible as integrals over space of an integrand that one can evaluate without too much difficulty at an arbitrary point \mathbf{r} . The numerical integrals can be reduced if the integration is carried out over the symmetry-unique region in the space and the number of integrations points is thereby reduced by a factor equal to the number of symmetry operators.^{3,12}

3.4.1. Molecular symmetry

According to the irreducible representations (irreps) to which the orbitals and the operator belong, one can predict many integrals to be zero. Entire blocks of integrals do not need to be calculated for this reason. Equivalent symmetry blocks can be treated at the same time. This implies that, for example, the x and y directions of a molecule with cylinder symmetry around the z -axis can be treated simultaneously.^{3,5} Almost all of the commonly encountered point group symmetries that have real irreps have been implemented in ADF. The Kohn–Sham–Fock matrix is constructed on the basis of functions that transform according to a particular irrep and subspecies of the point group. The symmetry-adapted functions are combinations of the original functions, orthogonalized on the frozen core and orthonormalized among themselves, resulting in an orthonormal and symmetry-adapted basis set in which the Fock matrix is block-diagonal. Diagonalization - block by block - yields the MOs grouped by symmetry representation.^{3,12}

3.4.2. Basis sets

In many quantum chemical calculations one would like to use the largest possible basis sets, but often one can only afford to use basis sets of limited quality. In any case, one would like to know the accuracy of the basis set used. One of the advantages to have several basis sets is that one can have a better idea of how the results of calculations of a certain property converge with respect to the basis set size.^{3.15} The basis sets employed by us to solve a conventional Scalar Relativistic (SR) calculation consist in finite basis sets of Slater-Type Orbitals (STO). In the first Ph. D. year we have dealt with testing the basis sets both in the geometry optimizations and in electronic excitation calculations, so to choose the more suitable calculation schemes to our aims. In quantum chemical calculations one often needs a smaller number of Slater-type functions than Gaussian-Type functions (GTOs), to obtain the same accuracy.^{3.15} Both are centred on the atoms, but STOs resemble the atomic orbitals more closely, because of their cusps at the nucleus and their slower decay in the outer region of the atom.^{3.5} However, the evaluation of the integrals with GTOs can be implemented analytically, at variance with STOs. Also in the literature Gaussian basis sets are more common than Slater-type basis sets. STOs are sometimes used in calculations where integrals can be numerically calculated. To reduce the number of basis functions methods are available where only the valence electrons are treated explicitly, like the frozen core approximation.^{3.15}

We have used the basis sets DZ and TZP for the geometry optimizations and the electronic valence excitations, and QZ3P-1DIFFUSE for the electronic core excitations, included in the database of the molecular ADF program. The all-electron DZ and TZP basis sets all are double zeta in the core, whereas in the valence region the DZ basis sets are double zeta and the TZP are triple zeta. QZ3P-1DIFFUSE includes diffuse functions in the basis set for a better description of molecular orbitals: these extra functions include functions that are unoccupied in the atom but have the same principal quantum number as an occupied atomic orbital. In general, these basis sets are not adequate for an accurate calculation of (highly) excited states, for which one needs to include extra diffuse basis functions.^{3.15}

3.4.3. Frozen core approximation

To reduce the sizes of the basis sets and therefore for saving computer time, we have utilized, where possible, the Frozen Core (FC) approximation. Two different types of frozen core basis sets were used: FC-DZ and FC-TZP. In the valence region these basis sets are the same as the

corresponding all-electron basis sets. However, in the core region these optimized frozen core basis sets have a single-zeta quality, whereas the corresponding all electron ones all have a double-zeta quality in this region. The basis functions in the frozen core calculations are orthogonalized on the accurately calculated core orbitals, coming from atomic calculations.^{3,15} To ensure orthogonality between the frozen core orbitals and the valence basis functions, the valence basis set used in the SCF equations is explicitly orthogonalized to the frozen core. This is achieved by adding to the valence set a series of auxiliary “core functions” χ_{μ}^{core} , precisely one for each frozen core orbital. Each valence function is replaced by a linear combination

$$\chi_v^{\text{valence}} \Rightarrow \chi_v^{\text{valence}} + \sum_{\mu} c_{\mu v} \chi_{\mu}^{\text{core}} \quad (3.29)$$

The condition that each such modified valence function be orthogonal to each frozen core orbital determines exactly all the coefficients $c_{\mu v}$. The frozen core orbitals are taken from very accurate single-atom calculations with large STO basis sets. The core functions don’t add variational freedom to the (valence) basis set, and hence, don’t increase the size of the secular (Fock) matrix to be diagonalized.^{3,12} In the scalar relativistic case, one needs extra core-like basis functions, to get high accuracy for the heavier systems. This is due to the fact that the core wiggles of especially the *s*-type valence electrons do not behave like Slater-type orbitals near the nucleus. For this reason an extra *1s*-type STO with large exponent is included in all the frozen core TZP basis sets. For the lighter elements the nonrelativistic optimized exponents were not changed in the DZ and TZP basis sets, only the description of the frozen core orbitals were changed from nonrelativistic to scalar relativistic.^{3,15}

3.4.4. Exchange-correlation potentials

To calculate the self-consistent solutions of the Kohn–Sham equation the exchange–correlation potential V_{xc} is derived from an approximate expression E_{xc} for the exact xc energy. Various approximations have been implemented in ADF, at the level of the Local Density Approximation (LDA), and with corrections from the Generalized Gradient Approximation (GGA) included.^{3,12} In calculations of geometry optimization of the naked gold clusters we have chosen the Vosko–Wilk–Nusair (VWN) parameterization of electron gas data at the LDA level, whereas in the others the formula Perdew–Wang (PW91) at the GGA level. In the TDDFT part of the calculation we have employed the Van Leeuwen–

Baerends exchange-correlation potential (LB94), since its correct Coulombic asymptotic behaviour has been proven important for an accurate description of virtual orbitals involved in the valence electron excitations. This has been further improved with the orbital-dependent SAOP (Statistical Average of Orbital Potentials), which have yielded very good results for response properties.^{3,12} For this reason in our first work we have considered both exchange correlation potentials. The calculated spectra were almost insensitive to this choice (see the Figure 3.2).

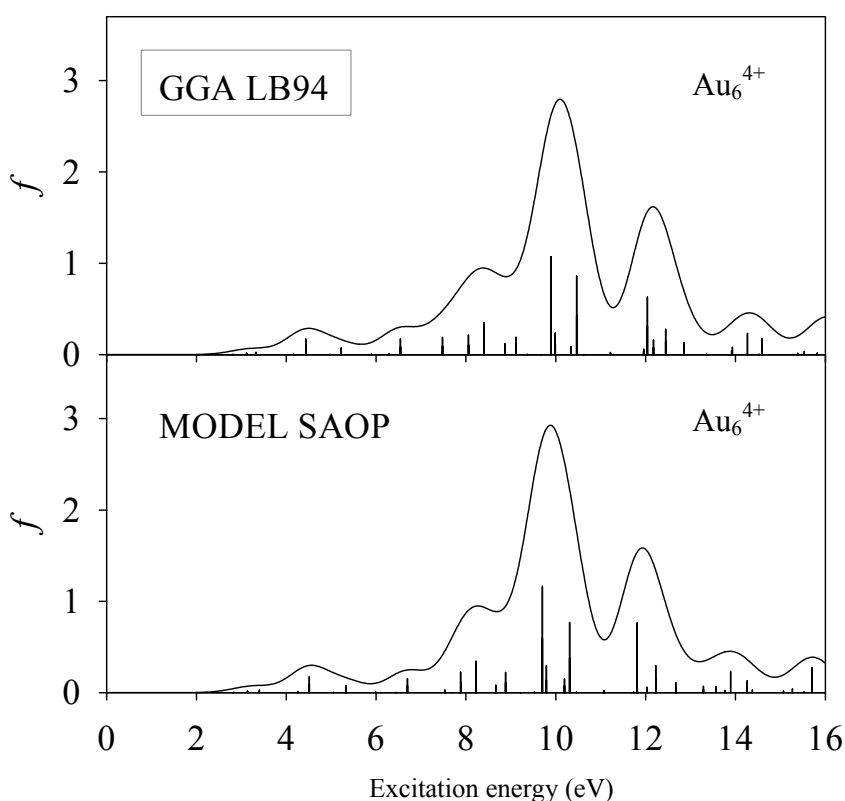


Figure 3.2 Comparison between the absorption spectra of the naked gold cluster Au_6^{4+} calculated with two different potentials. It has been framed that potential which then we have chosen for our following calculations.

Although SAOP is a more recent potential and is considered in general better than LB94, we have preferred to adopt LB94 for the successive calculations. This choice has been suggested because the SAOP doesn't allow us to employ a frozen core basis set, which is instead possible with LB94. So in order to exploit the computational economy of the frozen core basis and considering the negligible differences between the two potentials, the LB94 has been chosen.

3.5. SR AND SO ZORA FORMALISMS

5.5.1. SR ZORA

The STOs of the basis sets used in our calculations have exponents which has been optimized for the use in Scalar Relativistic Zeroth-Order Regular Approximated (SR-ZORA) equations.^{3,15}

It is well-known that the inclusion of relativistic effects is mandatory to describe properly the electronic structure of gold compounds, so we have employed this formalism. Excitation energies based on the scalar-ZORA TDDFT method has, in fact, shown to afford accurate results.^{3,13} The ZORA method is obtained by rewriting the energy expression and expanding in the term $E/(2mc^2-V)$, which remains small even close to the nucleus. Retaining only the zeroth order term one gets

$$E = \frac{p^2 c^2}{2mc^2 - V} + V \quad (3.30)$$

The ZORA Hamiltonian reads^{3,12}

$$H_{\text{ZORA}} = \boldsymbol{\sigma} \cdot \mathbf{p} \frac{c^2}{2c^2 - V} \boldsymbol{\sigma} \cdot \mathbf{p} + V \quad (3.31)$$

where $\boldsymbol{\sigma}$ is the Pauli spin matrix vector, c is the speed of light, \mathbf{p} is the moment operator and V is the total potential that equals the sum of the nuclear-attraction potential, the electronic-repulsion potential and the xc potential. As an experience with ZORA for ground-state calculations has indicated that only the near-nuclear part of the potential in the kinetic operator has a significant effect on the valence electron properties, the transitions involving valence electrons should have negligible effects on the near-nuclear part of the total potential. From this argument one can neglect the contribution of the ZORA kinetic term to the excitation energy terms.^{3,13} After mathematic reprocessing one obtains the approximation equation reported in the section 3.3. on the TDDFT calculations of the excitation energies, which can be solved with Davidson's algorithm in ADF program.

3.5.2. SO ZORA

In two works we have employed also the recent formalism based on the relativistic two-component ZORA with Spin-Orbit (SO) coupling. Such choice, to our knowledge, should represent at the moment the scheme that includes all the most relevant physical effects involved in the photoabsorption, ranging from the configuration mixing of TDDFT to the SO coupling, and, thanks to its excellent performance, can be applied to the cluster of moderate size and high symmetry with reasonable efforts. In this case the Hamiltonian has a additional term: the spin-orbit (H_{so}). It results from the interaction of the electron magnetic moments with the magnetic field generated by its own orbital motion. The computation becomes more involved than for the scalar relativistic terms because the spin-orbit term doesn't have the ordinary molecular symmetry. Instead, it is invariant under the molecular point double group, which affects both spin and spatial coordinates. From the orbitals (or basis functions) that are adapted to the irreps of the ordinary point group are obtained the spin orbitals adapted to the double group by coupling the space and spin parts with the double group coefficients.^{3,12} In practice, when the SO is included in the calculation, both the electronic structure and the electronic excitations undergo more or less pronounced complications, because now the non-s molecular orbital ($l \neq 0$) generate doubly-split states (see the Figure 3.3).

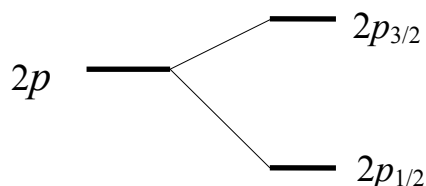


Figure 3.3 The splitting of $2p$ levels after the introduction of the spin-orbit coupling.

As concerns the SO coupling, the electronic structure is described in terms of spinors and the most relevant effect is the reduction of the degeneracy going from the MOs to the SO spinors. Spinors consist of one-electron functions, expressed as the sum of two products between a spatial and a spin function:

$$\chi(\mathbf{r}, \omega) = \varphi_{\alpha}(\mathbf{r})\alpha(\omega) + \varphi_{\beta}(\mathbf{r})\beta(\omega) \quad (3.32)$$

\mathbf{r} corresponds to the electron spatial coordinates and ω to the spin coordinate.

4. OPTICAL EXCITATIONS OF GOLD NANOPARTICLES: A QUANTUM CHEMICAL SCALAR RELATIVISTIC TIME DEPENDENT DENSITY FUNCTIONAL STUDY

Stener, M.; Nardelli, A.; De Francesco, R.; Fronzoni, G. *J. Phys. Chem. C* **2007**, *111*, 11862-11871.

The valence optical excitation spectra of the gold clusters series Au_6^{4+} , Au_{44}^{4+} and Au_{146}^{2+} have been calculated at the scalar relativistic Time Dependent Density Functional Theory level. Optical spectra have been calculated at the optimized geometries, the electronic structure has been described in terms of Density of States and optical spectra have been discussed in terms of electronic structure features. The well known blue shift with decreasing cluster size has been successfully predicted by the theory.

4.1. INTRODUCTION

The interest in the optical properties of gold nanoparticles has recently experienced an important development, both experimentally and theoretically.^{4.1} In fact such systems are characterized by specific properties which make them unique as optical materials. This is due to the extreme versatility of gold to form well-defined nanosized structures, whose shapes can be tuned and controlled, to some extent, already at the level of a conventional chemical synthesis.^{4.2-4.5} This allows to routinely produce gold nanoparticles samples with well defined shape and size distributions, which can be easily characterized with conventional electron microscope techniques, such as TEM and SEM. Such samples are usually synthesized in solution, and gold nanoparticles must therefore be stabilized with proper ligands: among them thiolates play a central role, due to their specific high tendency to form strong Au-S chemical bonds. Alternative protective agents, such as surfactants, can also be employed to stabilize nanoparticles with weaker chemical bonds. The uniqueness of the Au-S interaction plays an important role not only for the stabilization of gold nanoparticles, but also in the Self Assembled Monolayers (SAM) of thiolates on gold surfaces.

The optical properties of gold nanoparticles are dominated by a strong absorption band which, for sufficiently large size of the nanoparticle, falls in the visible region.^{4.1} This feature is very sensitive to specific characteristics of the sample, namely the particle size, its shape, the nature of the stabilizing ligand and the nature of the solvent where the nanoparticles are dispersed in. Such strong absorption band is generally referred as the Surface Plasmon Resonance (SPR)^{4.6} and is interpreted as a collective excitation of the conduction electrons of the metal particle. Moreover, since SPR is localized at the surface of the nanoparticle, it is a typical quantum size effect which is absent in bulk material, therefore standard methods of solid state physics based on periodic boundary conditions are not suited to investigate such phenomenon.

Due to the importance of the SPR as a leading optical nanoparticle property, it has emerged the necessity to propose theoretical models with the aim to simulate this effect in order to rationalize the experimental findings and, with a more ambitious goal, to perform a computational design of novel nanostructured materials with specific optical properties.

In this context, the first proposed and widely used method is the Mie's theory, which treats the light scattering by a conducting sphere in a pure classical manner. Although this approach is quite simple, computationally cheap and qualitatively correct, it suffers of two obvious shortcomings: first the model does not consider at all the discrete atomic structure of the real nanoparticle which is treated as a homogeneous conducting medium, and second the model is based on classical electrodynamics and therefore quantum size effects are completely neglected. Moreover, Mie's theory can be applied analytically only to spherical, ellipsoidal and core-shell structures, if different shapes are considered numerical techniques as electromagnetic Finite Differences Time Domain (FTTD)^{4.7} or Discrete Dipole Approximation (DDA)^{4.8} must be employed.

A first improvement beyond classical Mie's theory is represented by the Time Dependent Local Density Approximation (TDLDA) implemented within the *jellium* model,^{4.9} that is the metal nanoparticle is modellized as a background consisting of a spherical positive charge density which describes the average nuclei positions; such positive background supports the electrons whose motion is treated in terms of quantum mechanics. Also in this case the *jellium* model misses the discrete atomic structure of the cluster, but the TDLDA method gives a quantum mechanical description of the electron excitations of the model system: the SPR is described as a collective excitation of the electrons, that is as free electron oscillations. Moreover, the TDLDA *jellium* model offers a practical tool to consider more specific effects

which can be included in the method, namely the effect of an embedding medium to simulate, for example, the solvent effects.^{4,10}

In order to improve the theoretical description, it is therefore appealing to consider an approach able to retain the atomic structure of the cluster, and a possible choice would be the Time Dependent Density Functional Theory (TDDFT) formalism implemented in the conventional quantum chemical Linear Combination of Atomic Orbital (LCAO) method. This choice joins the reliability of modern TDDFT approaches to describe electron excitations, with the accuracy of the LCAO implementation which avoids the drastic approximation of the effective molecular potential operated by the *jellium* approach. Very recently optical spectra of metal clusters protected by ligands have been calculated by the TDDFT method using finite basis set of contracted Gaussian-type orbitals^{4,11,4,12} and plane wave basis set;^{4,13} in the latter case a cluster with a size up to 39 gold atoms has been considered. Of course the LCAO-TDDFT method is computationally much more demanding than *jellium* methods, however it represents the state-of-the-art approach for the theoretical description of the optical spectra for large molecules, and therefore it is a potential tool to understand in detail the electron excitation process and a valid instrument to help the design of new nanoparticles with specific optical properties.

In this work we have considered a series of three positively charged gold clusters of increasing size: Au_6^{4+} , Au_{44}^{4+} and Au_{146}^{2+} . As a preliminary goal, we have assessed the requirements of the TDDFT method for gold clusters, namely the basis set size, the exchange correlation potential choice and the frozen core level of approximation to reduce computational efforts. Although a series of neutral clusters would have been preferable, we have been forced to consider charged systems in order to obtain a closed shell electronic structure, in fact current TDDFT implementations are often limited to closed shell systems. Recent extensions to the open-shell TDDFT formalism are actually available^{4,14} but are limited to the excitation energy calculations and do not support the extraction of the intensity in terms of the oscillator strength which is a key ingredient for the present study.

Although most of the experiments are actually relative to gold nanoparticles protected by ligands, we have restricted our study to naked gold cluster, in fact the phenomenology, at least as the SPR is concerned, is essentially an effect of the gold core. Of course ligands can induce relevant changes on the electronic structure of the metallic core and, as a consequence, on the optical spectra, however as an initial study, we preferred to limit our attention to the simplest systems which carry the essence of the phenomenon and consider only size variations along the series. Naked gold clusters, in any case, represent an active research field, for example it

has recently found both experimentally and theoretically the exceptional stability and unusual properties of a tetrahedral Au₂₀ cluster^{4.15} also in the second-order optical properties.^{4.16} Other issues, like for example the effect of the cluster shape, of the gold oxidation state as well as of the protecting ligands will be possible objects for further studies.

4.2. THEORETICAL METHOD

The first step consists to solve a conventional Scalar Relativistic (SR) Self-Consistent Field (SCF) Kohn-Sham (KS) calculation, employing a finite basis set of Slater Type Orbitals (STO) with the ADF code.^{4.17,4.18} It is well known that the inclusion of relativistic effects is mandatory to describe properly the electronic structure of gold compounds,^{4.19} so we have employed the SR Zero Order Regular Approximation (ZORA) formalism.^{4.20}

The results of the SR-KS calculation (KS eigenvalues and orbitals) are then used as input for the following TDDFT section. The TDDFT approach for electron excitations and its implementation in the ADF code has been described in detail the literature,^{4.21} so here we just recall the salient steps.

The general problem is cast in the following eigenvalue equation:

$$\Omega \mathbf{F}_I = \omega_I^2 \mathbf{F}_I \quad (4.1)$$

where Ω is a four indexes matrix with elements $\Omega_{ia\sigma, jb\tau}$, the indexes consist of products of occupied-virtual (ia and jb) KS orbitals, while σ and τ refer to the spin variable. The eigenvalues ω_I^2 correspond to squared excitation energies while the oscillator strengths are extracted from the eigenvectors \mathbf{F}_I .^{4.22} The Ω -matrix elements can be expressed in terms of KS eigenvalues (ε) and the coupling matrix K:

$$\Omega_{ia\sigma, jb\tau} = \delta_{\sigma\tau} \delta_{ij} \delta_{ab} (\varepsilon_a - \varepsilon_i)^2 + 2\sqrt{(\varepsilon_a - \varepsilon_i)} K_{ia\sigma, jb\tau} \sqrt{(\varepsilon_b - \varepsilon_j)} \quad (4.2)$$

the elements of the coupling matrix K are given by:

$$K_{ij\sigma,kl\tau} = \int d\mathbf{r} \int d\mathbf{r}' \varphi_{i\sigma}(\mathbf{r}) \varphi_{j\sigma}(\mathbf{r}) \left[\frac{1}{|\mathbf{r}-\mathbf{r}'|} + f_{xc}^{\sigma\tau}(\mathbf{r}, \mathbf{r}', \omega) \right] \varphi_{k\tau}(\mathbf{r}') \varphi_{l\tau}(\mathbf{r}') \quad (4.3)$$

where φ are the KS orbitals and $f_{xc}^{\sigma\tau}(\mathbf{r}, \mathbf{r}', \omega)$ is the exchange-correlation kernel. In this work the kernel is approximated according to the Adiabatic Local Density Approximation (ALDA).^{4.23}

4.3. COMPUTATIONAL DETAILS

In the present work the first step to consider is to obtain the optimized geometries of the clusters under study. To this end, we have optimized the cluster geometries with the scalar relativistic ZORA formalism^{4.20} employing the ADF program.^{4.17,4.18} Different basis sets have been tested, namely the ZORA DZ and TZP optimized basis sets included in the ADF program. In order to reduce the computational effort, we have also tried different schemes of frozen core basis sets: in the following we designate with AE the All Electron set, and with FC 4*d* and FC 4*f* the sets whose inner core orbitals have been kept frozen in the molecular calculation, up to the 4*d* and the 4*f* shells respectively. For the geometry optimizations, we have always employed the Local Density Approximation (LDA)^{4.24} to the exchange correlation functional, according to the VWN parametrization.^{4.25} The very good performances of the LDA geometry optimization with respect to the experimental bulk limit interatomic distance for gold clusters of increasing size has been demonstrated previously.^{4.26}

The TDDFT calculations have been performed at the optimized geometries, and also in this case the same ZORA basis sets have been tested, including the frozen core. Moreover, in TDDFT calculations two exchange correlation potentials have been considered, namely the LB94^{4.27} and the SAOP.^{4.28} In fact it is well known that to obtain accurate TDDFT valence electron spectra, it is necessary to employ an exchange correlation potential with the correct Coulomb asymptotic behaviour.^{4.29} Such requirement is not fulfilled by the LDA, at variance with LB94 and SAOP which instead display the correct asymptotic decay. Other asymptotically correct potentials are actually available, like for example the Gradient Regulated Asymptotic Correction LB (GRACLB),^{4.30} however its use has been rather occasional in the literature, so we prefer to limit our attention only to well tested exchange correlation potentials.

As it will be justified in the next section, all calculations (geometry optimization as well as TDDFT optical spectra) has been performed employing the D_{4h} point group symmetry.

A critical point of the present TDDFT approach is the number of the lowest roots to be extracted from Equation (4.1). In fact such number has a decisive impact on the computational effort required for the calculation and must be adequate in order to have a proper description of the calculated spectrum, namely it controls the upper limit of the excitation energy range. In the present work the spectra calculated with DZ basis set were obtained extracting the following number of roots for each active dipole symmetry: for Au_6^{4+} 62 E_u and 38 A_{2u} , for Au_{44}^{4+} 609 E_u and 391 A_{2u} , for Au_{146}^{2+} 500 E_u and 300 A_{2u} , such choices allowed to calculate the optical spectra up to 15.94, 7.48 and 3.68 eV for the three clusters respectively.

4.4. RESULTS AND DISCUSSION

As a preliminary remark, it must be considered that the main focus of the present work is to assess the performances of a modern molecular TDDFT approach for the calculation of the optical spectra of gold nanoparticles. The first issue is to obtain a series of closed shell gold clusters, possibly highly symmetric for computational economy. The most natural choice would have been the series of octahedral clusters Au_6 , Au_{44} and Au_{146} , but all they are open shell, being their Highest Occupied Molecular Orbital (HOMO) partially filled: t_{1u}^4 for Au_6 and Au_{44} , and t_{1u}^2 for Au_{146} . In order to remove degeneracy and to favour shell closing, we tried to reduce the symmetry from O_h to D_{4h} . Although the symmetry lowering worked for Au_6 , for the other two larger clusters it did not work, since only a very small energy gap between initially degenerate orbitals was introduced by the symmetry reduction, not enough to favour a closed shell electron configuration. Therefore we have been forced to consider charged clusters, simply removing the electrons lying in the partially filled orbitals t_{1u} , so our final series consists of the three charged clusters Au_6^{4+} , Au_{44}^{4+} and Au_{146}^{2+} . The necessity to employ charged clusters in order to limit the analysis to closed shell electronic structure is a general problem for TDDFT approaches.^{4.11,4.31} Moreover we have also noticed that although all these charged clusters have closed shell O_h structures, a symmetry lowering to D_{4h} symmetry gives further stabilization, so finally we have decided to employ the D_{4h} symmetry for all calculations.

We underline that the symmetry constraint presently adopted is reasonable for the two larger systems, in fact it is well known that large gold cluster prefer tridimensional geometries^{4.19,4.32} while smaller cluster prefers a planar geometry.^{4.33} In the present case we have considered a tridimensional structure also for Au_6^{4+} in order to have a cluster series with the same geometry. It is also known that large tridimensional clusters may prefer disordered structures,^{4.34} so in this work we do not attempt a discussion on the cluster geometries, but we will limit our analysis to the electronic structure and the optical spectra.

The shapes of the three Au_6^{4+} , Au_{44}^{4+} and Au_{146}^{2+} D_{4h} clusters optimized at the SR-ZORA DZ level are reported in Figure 4.1; to give an idea of their dimensions, we report the maximum distances between two opposite vertexes: 4.00 Å, 11.7 Å and 19.35 Å respectively.

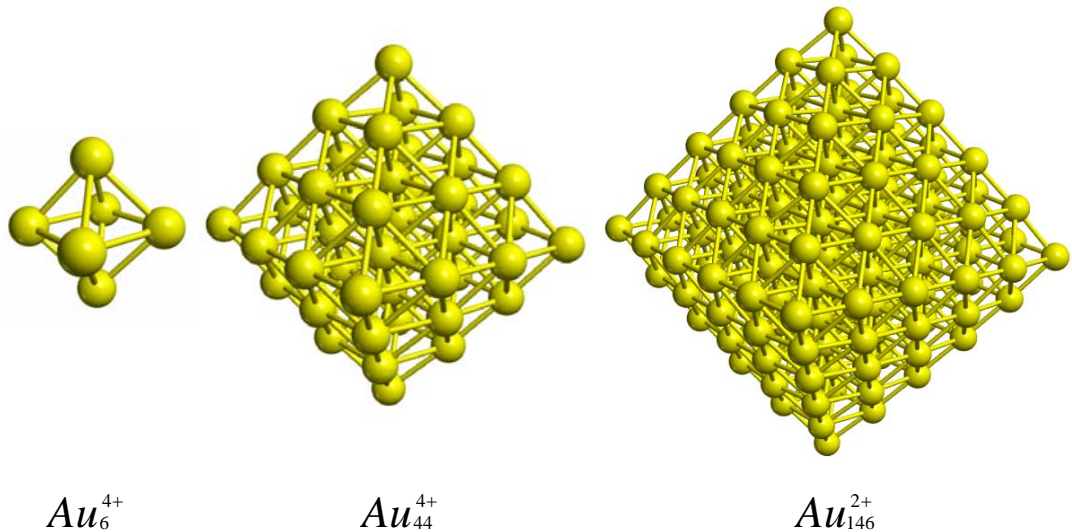


Figure 4.1 The optimized geometries of the clusters Au_6^{4+} , Au_{44}^{4+} and Au_{146}^{2+} .

4.4.1. Au_6^{4+}

The first cluster of the series has been used to assess the computational scheme to be employed also for the larger clusters, in order to choose the basis set and the exchange correlation potential. In figure 4.2, we have reported the valence excitation spectrum of Au_6^{4+} employing both ZORA-DZ and ZORA-TZP basis sets, employing the optimized geometry at the DZ level. In preliminary test calculations we have also calculated the spectra employing the geometry optimized at the TZP level, finding negligible differences with respect to the spectra calculated employing the DZ optimized geometry.

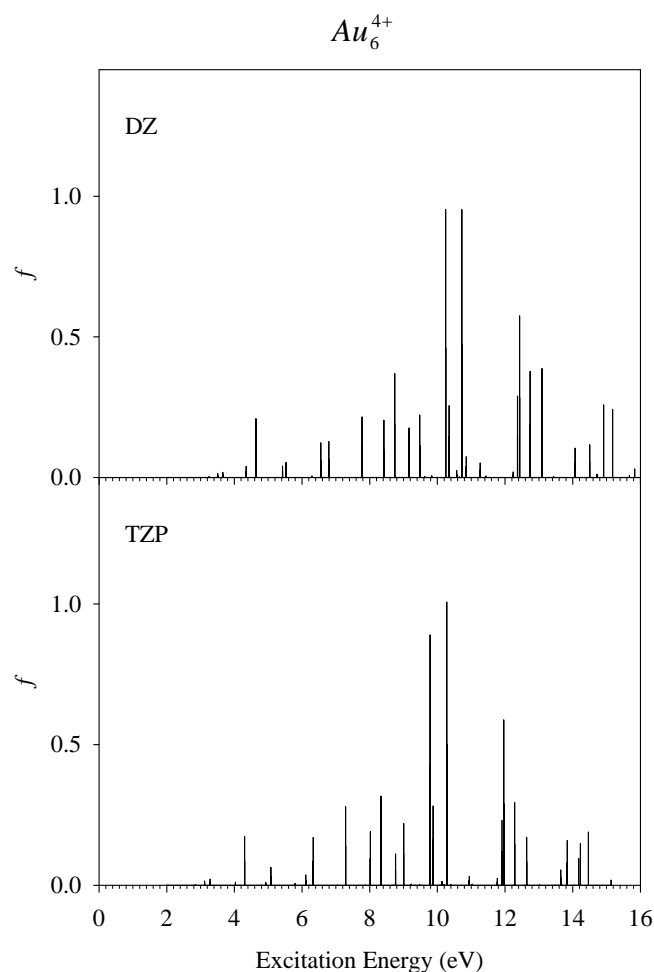


Figure 4.2 TDDFT valence excitation spectra (oscillator strength vs excitation energy) of Au_6^{4+} calculated with DZ and TZP basis set.

In figure 4.2 the comparison between the DZ and the TZP basis clearly indicates that both choices furnish essentially the same results, so we are lead to the conclusion that DZ basis set can be profitably employed for both geometry optimization and TDDFT calculations. Only tiny differences are revealed in the high energy spectral region (beyond roughly 12 eV), however this is of less relevance if we consider that for larger clusters the energy region of general interest is usually confined to few eV's, say up to 4 - 5 eV. As a preliminary conclusion of this analysis, we can say that the DZ basis set is enough accurate for the present purposes and therefore will be employed also for the larger clusters.

Another important choice with a decisive impact on the computational economy, is the possibility to freeze inner atomic orbitals, with the so-called "frozen core" (FC) procedure. We have considered therefore additional test calculations on the spectra relative to Au_6^{4+} but with different frozen core levels: an all electron calculation, that is all electrons are explicitly included in the calculations, and FC 4d and FC 4f calculations, where inner atomic shells up to 4d and 4f atomic orbitals, respectively, have been kept frozen in the molecular calculation.

The effect of the frozen core procedure did not worsen the results at all, so in the following we will always employ the ZORA DZ FC 4*f* basis set.

The next fundamental choice to be considered regards the exchange correlation potential: it is well known^{4,29} that to obtain reliable TDDFT valence excitation spectra it is mandatory to employ an exchange correlation potential with correct coulombic asymptotic behaviour: this is important to describe correctly the virtual orbitals. Both LB94^{4,27} and SAOP^{4,28} have been considered: the calculated spectra are almost insensitive to this choice. Although SAOP is a more recent potential and is considered in general better than LB94, we have preferred to adopt LB94 for the successive calculations. This choice has been suggested because the SAOP does not allow to employ frozen core basis set, which is instead possible with LB94. So in order to exploit the computational economy of the frozen core basis and considered the negligible differences between the two potentials the LB94 has been chosen.

Once all the relevant computational choices have been fixed, we may start the discussion of the actual results, considering first the electronic structure of the Au_6^{4+} cluster. The cluster is small enough to enable an easy conventional description in terms of molecular orbitals, however this would become soon impracticable for larger clusters. So we have preferred to present the electronic structure in terms of Partial Density Of States (PDOS) in Figure 4.3, obtained with a Lorentzian broadening of FWHM = 0.12 eV.

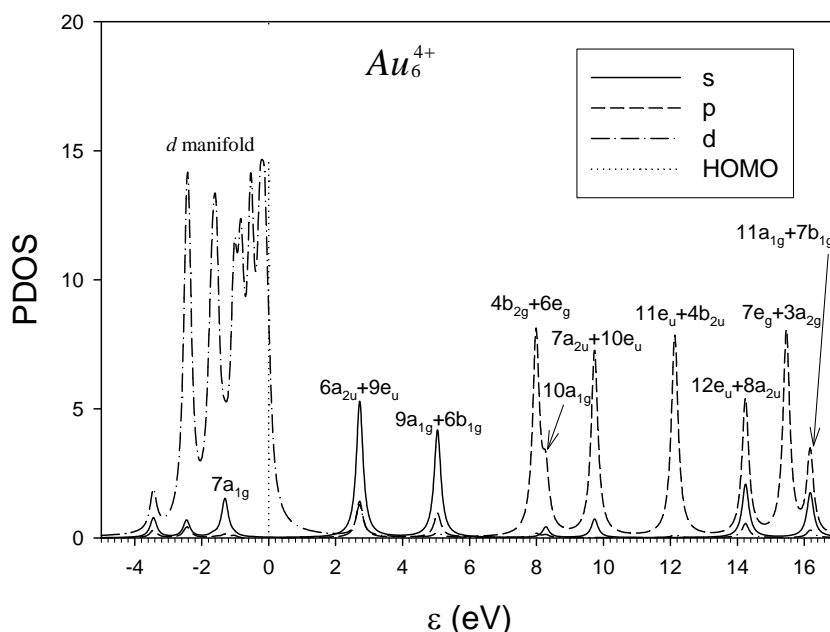


Figure 4.3 Partial DOS profiles of Au_6^{4+} calculated with DZ basis set, obtained with a lorentzian broadening of FWHM = 0.12 eV.

We have employed a relative energy scale with respect to the HOMO (showed as a vertical dotted line) at zero energy: this is useful to compare clusters with different charges as in the

present case, since the major effect of different cluster charges is a strong shift of the orbital energies. In principle PDOS plots may be further split in order to discriminate contributions from different non-equivalent atoms, i.e. axial and equatorial ones in D_{4h} symmetry. We did not report such analysis because the deviation from a pure octahedral symmetry is so small that the contributions from different sites are in practice equal.

The most prominent PDOS feature is the group of states with essentially pure d character which lie below the HOMO and are therefore completely filled, the corresponding band is indicated as d manifold in the figure and originates from the completely filled $5d^{10}$ atomic shell of gold atoms. Its wideness is 3.44 eV as an effect of the interaction among the $5d$ shells belonging to the different atoms. Notice that only very minor d atomic contributions are calculated for the empty states, with the exception of the LUMO ($6a_{2u}$) at 2.72 eV where the d contribution is around 15%.

The partial s DOS is distributed between both occupied and empty states. Below the HOMO, only the $7a_{1g}$ molecular orbital at -1.31 eV shows predominant s character (57%), while two empty s bands are observed. The first s empty band at 2.72 eV (LUMO) is constituted by two orbitals ($6a_{2u}$ and $9e_u$) with 67% s character, as well as the second one at 5.05 eV ($9a_{1g}$ and $6b_{1g}$) with 79% s character. Such situation can be very easily rationalized in terms of symmetrized group orbitals built with the six $6s$ gold atomic functions in octahedral symmetry, in fact although the cluster has actually D_{4h} symmetry, the deviation from the octahedron is small enough to give only negligible splitting of degenerate orbitals. Therefore the six $6s$ atomic functions in octahedral environment are split in three groups: the a_{1g} representation at low energy (the occupied $7a_{1g}$ orbital), followed by the t_{1u} (split in $6a_{2u}$ and $9e_u$) and finally by the e_g (split in $9a_{1g}$ and $6b_{1g}$) both unoccupied. The partial occupation of the $6s$ band is the result of the electron budget: to the six $6s^1$ electrons arising from the atomic shell must be subtracted four electrons due to the cluster total charge, the remaining two electrons fill the lower $7a_{1g}$ orbital leaving the uppermost ones unoccupied. Moreover, it is worth noting that, for the filled $7a_{1g}$ orbital, a noticeable 39% d contribution and a small 5% p contribution are calculated. The p and d contributions are reversed for the two unoccupied virtual bands: a 18% p contribution is predicted for both bands, while d contribution is 15% and 2% for t_{1u} and e_g respectively. This analysis of the band with high s character may be summarized as follows: the occupied s state is strongly hybridized with d orbitals, while for virtual s bands a moderate hybridization with p orbitals is observed. The role of s - d hybridization for gold chemistry is of crucial importance in determining the properties of its compounds,^{4,19} and its accurate description is one of the most relevant success of the

relativistic quantum chemistry approaches. In fact non-relativistic gold calculations give a too wide $5d$ - $6s$ energy gap, which prevent efficient hybridization. Present scalar relativistic ZORA calculations guarantee a proper and accurate treatment of this effect. Another interesting s - d hybridization effect is also found within the d manifold: at -2.45 and -3.44 eV the preponderant d character states are mixed with 8% and 30% s contribution.

The partial p DOS is now considered: such states are all empty, and lie in a rather wide energy range between 7.99 and 16.19 eV above the HOMO. Seven distinct peaks are clearly observed, which can be classified according to the symmetrized group orbitals arising from the $6p$ atomic functions on the octahedron vertexes, namely four states from the $6p\pi$ orbitals t_{2g} ($4b_{2g} + 6e_g$), t_{1u} ($7a_{2u} + 10e_u$), t_{2u} ($11e_u + 4b_{2u}$), t_{1g} ($7e_g + 3a_{2g}$) and three states from the $6p\sigma$ orbitals a_{1g} ($10a_{1g}$), t_{1u} ($8a_{2u} + 12e_u$), e_g ($11a_{1g} + 8a_{2u}$). Actually the t_{1u} symmetry appears twice and therefore the character of all t_{1u} orbitals is mixed σ and π . It is worth noting the almost pure p character of such states, the most important hybridization is observed for the second t_{1u} band ($8a_{2u} + 12e_u$) whose s contribution is around 25%.

For Au_6^{4+} we may summarize the electronic structure as follows: a completely filled d band covers the range between HOMO (taken as zero energy reference) and -3.44 eV, a completely empty p band lies high in energy and covers a wide range between 7.99 and 16.19 eV, and a partially filled s band lies from -1.31 eV to 5.05 eV. The d band is the narrowest, due to the rather compact shape of the $5d$ functions, the p band is the widest due to the more diffuse $6p$ functions, while the s band lies in between them.

Having assessed in detail the electronic structure of Au_6^{4+} , it is now possible to discuss the DZ excitation spectrum of previous Figure 4.2. From the electronic structure and by simple eigenvalue difference argument, we should expect to identify $s \leftarrow d$ interband transitions in the excitation energy range from 2.72 eV up to 8.49 eV, $p \leftarrow d$ interband transitions in the excitation energy range from 7.99 eV up to 19.63 eV, together with some additional intraband $s \leftarrow s$ and interband $p \leftarrow s$ transitions. This picture is of course simplified, since TDDFT couples several one-electron $1h$ - $1p$ excited configurations and therefore excitation energy may deviate with some extent with respect to the eigenvalue difference, but may be employed as a rule of thumb to identify various spectral regions. In order to analyze in detail the excitation spectrum, we have reported in Table 4.1 (reported at the end of the chapter) the results of the TDDFT calculations, for the two dipole allowed symmetries A_{2u} and E_u up to 13 eV of excitation energy. In particular we have considered only the transitions with oscillator strength $f > 0.1$, and for each transition we have also reported the main terms of the specific

one-electron excited configurations which contribute to the transition. It is apparent that all the excitations up to 7.77 eV are essentially $s \leftarrow d$ interband excitations, with rather weak intensity, see also Figure 4.2 to compare the whole spectrum (upper panel, DZ basis set). It is worth noting that all the most intense transitions in this region reported in Table 4.1 contains some contribution of $s \leftarrow s$ intraband configuration, although among these only the $5A_{2u}$ has major s - s character, and can be ascribed mainly to the $6a_{2u} \leftarrow 7a_{1g}$ configuration. In summary we may say that very weak photoabsorption is found for energy below 8 eV for the $s \leftarrow d$ intraband excitations, with the exception of occasional $s \leftarrow s$ intraband effects which increases the intensity.

The excitations above 8 eV are all ascribed to $p \leftarrow d$ interband transitions, in particular $36E_u$ and $42E_u$ are the most intense, with intensity up to $f = 0.952$. However it is very interesting that also very weak $p \leftarrow d$ transitions are calculated (not reported in Table 4.1), so the interband $p \leftarrow d$ nature is a necessary but not sufficient condition to give strong intensity. As a general remark about the composition of the transitions in terms of one-electron excited configurations, it must be noted that almost always a rather strong mixing is observed, this finding reveals the "collective" nature of the electron excitation, a key effect included in the TDDFT formalism. As a final comment, we observe that actually A_{2u} and E_u excitation spectra are in practice equivalent, apart the doubled oscillator strengths calculated for the latter as a consequence of the degeneracy. This is not surprising due to the slightly distorted octahedral optimized geometry of the Au_6^{4+} cluster.

The present Au_6^{4+} cluster has been employed mainly as a simple model test case to introduce the larger members of the series, so there are no direct experimental data for comparison. However we may check the consistency of the present results comparing them with the experimental optical absorption spectra of a series of small gold clusters and their cations obtained in molecular beam experiments with van der Waals xenon complexes.^{4,35} In such experiment a maximum around 3.7 eV is observed, followed by and abrupt increase of the cross section for energies higher than 5 eV. This is consistent with our results: the high energy (> 5 eV) feature may be ascribed to the opening of the wide $p \leftarrow d$ interband transitions, while the feature around 3.7 eV might be related to an isolated $s \leftarrow s$ intraband transitions.

4.4.2. Au_{44}^{4+} and Au_{146}^{2+}

In this section we will consider together both clusters Au_{44}^{4+} and Au_{146}^{2+} : in fact their complex electronic structures prevent detailed analysis as performed for Au_6^{4+} and we will be rather more interested in the evolution of the properties with respect to the cluster size.

In Figure 4.4 the partial DOS obtained with a Lorentzian broadening of FWHM = 0.12 eV of both clusters is reported: the first observation is that, at variance with Au_6^{4+} , not only the partial contribution are much broader as an effect of the larger number of overlapping states, but also it is not easy to identify precise regions with pure contribution. The only band which retains a strong pure character is the d manifold, which contributes at energies 2 eV below the HOMO.

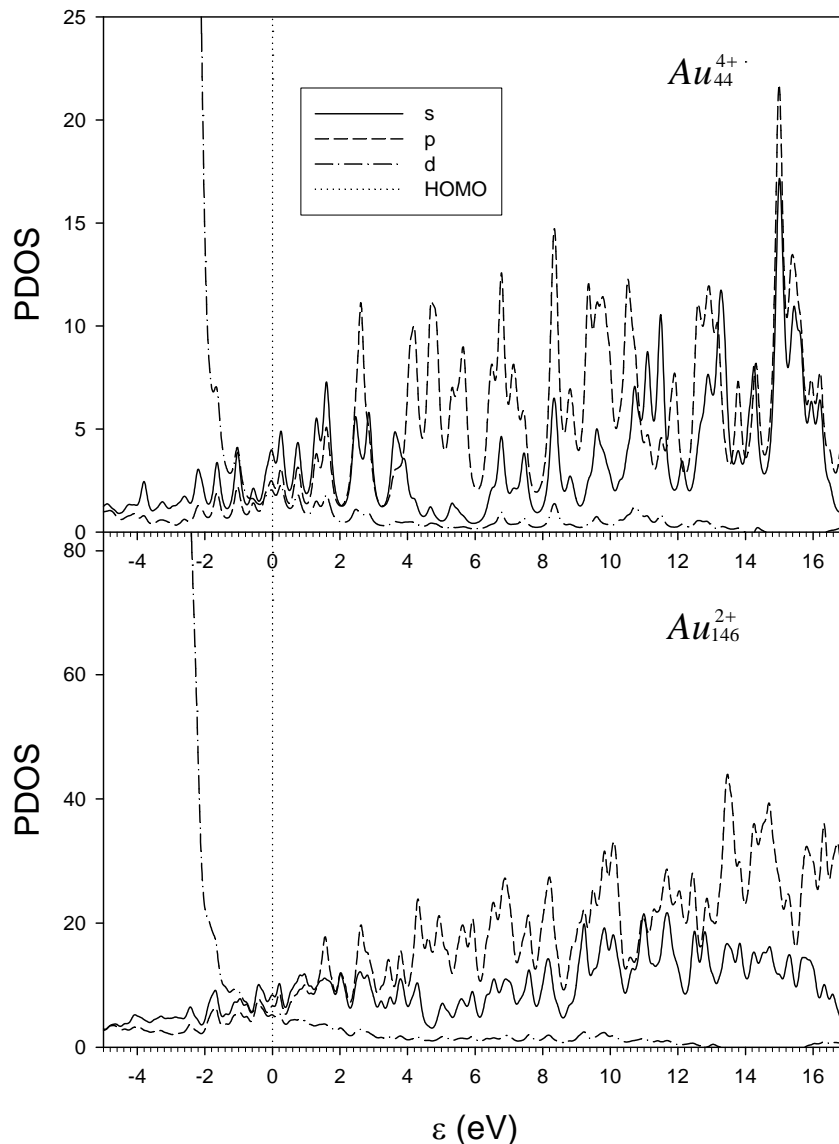


Figure 4.4 Partial DOS profiles of Au_{44}^{4+} and Au_{146}^{2+} calculated with DZ basis set, obtained with a Lorentzian broadening of FWHM = 0.12 eV.

Near the HOMO the states are strongly mixed, as well as in the region of the unoccupied orbitals. In particular for Au_{44}^{4+} the lowest virtual states have a predominant s character up to about 2 eV, then p character is dominant up to 10 eV where s contribution becomes again to gain importance. In Au_{146}^{2+} the PDOS profiles are even smoother than in Au_{44}^{4+} , and both s and p contribute with comparable weight up to 2 eV, then the p contribution is always the dominant. The broadening of the bands with cluster size is an obvious effect of the interactions of the successive atomic shells which constitute the clusters, however this effect is particularly enhanced by the small $5d$ - $6s$ gap which favours s - d hybridization and makes the states near the HOMO really very mixed. This will complicate the assessment of the optical spectra, in fact the region of practical interest for the optical properties of the clusters is confined to few eV's of excitation energy.

In Figure 4.5 we have reported the TDDFT excitation spectra of both Au_{44}^{4+} and Au_{146}^{2+} , calculated up to about 7 eV and 3.5 eV respectively: for Au_{146}^{2+} we have not been able to extract more roots from equation (4.1) due to the excessive computational effort needed to enlarge the energy range. In the present case this shortcoming does not represent a serious problem, since the spectral features of experimental relevance are still below 3.5 eV, but for larger or less symmetric systems this may represent a limitation of the present algorithm: we will come back later on this point to explore possible solutions.

The excitation spectrum of Au_{44}^{4+} (Figure 4.5 upper panel) is characterized by an extremely congested series of discrete lines, so we have convoluted the calculated spectrum with gaussian functions of FWHM = 0.12 eV, not only to allow an easier comparison with an eventual experimental spectrum, but also to identify more easily the regions where most of the intensity is distributed. The first absorption starts at 1.6 eV and remains very weak up to 2.7 eV where it starts to grow up to a strong maximum at 4.6 eV, then around 5.4 eV a minimum is predicted due to the rarefaction and weakening of the discrete lines, the intensity then increases again showing maxima around 5.8 and 6.5 eV.

The TDDFT spectrum of Au_{146}^{2+} is considered in the lower panel of Figure 4.5: the spectral pattern qualitatively resembles that calculated for Au_{44}^{4+} in the low energy region, in fact also for this case we may identify several energy ranges characterized by increasing intensity: an extremely weak absorption is calculated from 1.0 up to 1.3 eV, followed by a rather flat intensity from 1.4 to 2.0 eV, then a stronger structure is found from 2.2 to 2.5 eV and finally the intensity grows rapidly from 2.7 eV to reach two maxima around 3.0 eV. We do not attempt to discuss the region above 3 eV since we do not have extracted roots above 3.6 eV

and therefore the convoluted profile, considering the employed FWHM = 0.12 eV, may be considered reliable only up to roughly 3.3 eV: this at least guarantees the existence of the maxima at 3.0 eV.

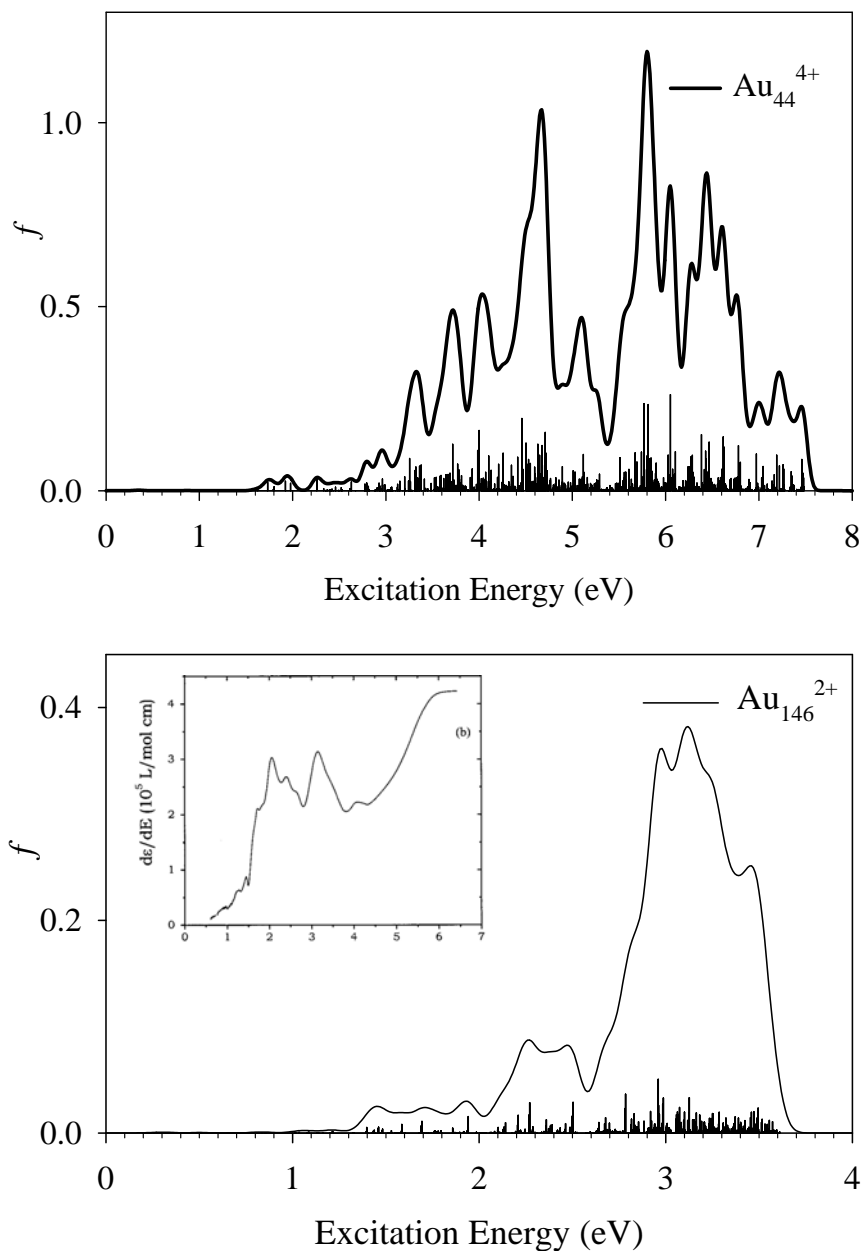


Figure 4.5 TDDFT valence excitation spectra (oscillator strength vs excitation energy) of Au_{44}^{4+} (upper panel) and Au_{146}^{2+} (lower panel) calculated with DZ basis set (vertical lines), convoluted spectra obtained with gaussian broadening with FWHM = 0.12 eV are reported as solid line (thick line for Au_{44}^{4+} and thin line for Au_{146}^{2+}). Experimental differential absorption spectrum taken from ref. 4.36 (with permissions) of 29kDa Au:SR is reported as inset of lower panel.

It is interesting to compare the calculated optical spectrum of Au_{146}^{2+} with the experimental data^{4.36} obtained for a gold cluster protected by thiol groups having the same nuclearity (29 kDa of mass of the metal core), which are reported in the inset of Figure 4.5 as well. Of

course we must consider that the calculated cluster is not protected by ligands, and therefore only qualitative comparison is possible, since we expect that the formation of strong covalent Au-S bonds perturb to some extent the electronic structure of the metal core and therefore the optical spectrum. However, we can easily identify in the calculated spectrum the counterparts of the experimental features: the sudden increase of absorbance measured at 1.6 eV is fairly well reproduced by the calculation at 1.4 eV. The experimental differential spectrum displays also two maxima around 2.0 eV and 3.0 eV, which should correspond to regions of maximum slope of absorption, such stepwise increase is actually reproduced by the calculation at 2.1 eV and 2.8 eV respectively. Such behaviour has been already discussed^{4.36-4.38} in terms of weak $sp \leftarrow sp$ intraband transition below 1.6 eV and stronger interband $sp \leftarrow d$ transition for higher energy. This is consistent with the electronic structure of the cluster previously discussed in terms of PDOS (Figure 4.4 lower panel): the huge d onset starts to overcome the other contributions around -1.5 eV (with respect to the HOMO) therefore excitation of d band is expected to enhance abruptly for energies larger than 1.5 eV.

In the next Figure 4.6 we compare together the results of the two clusters Au_{44}^{4+} and Au_{146}^{2+} in order to identify possible trends between the spectra. In fact, at least for gold clusters of larger size, it is well known for example that the SPR is subjected to a *blue shift* with *decreasing* size.

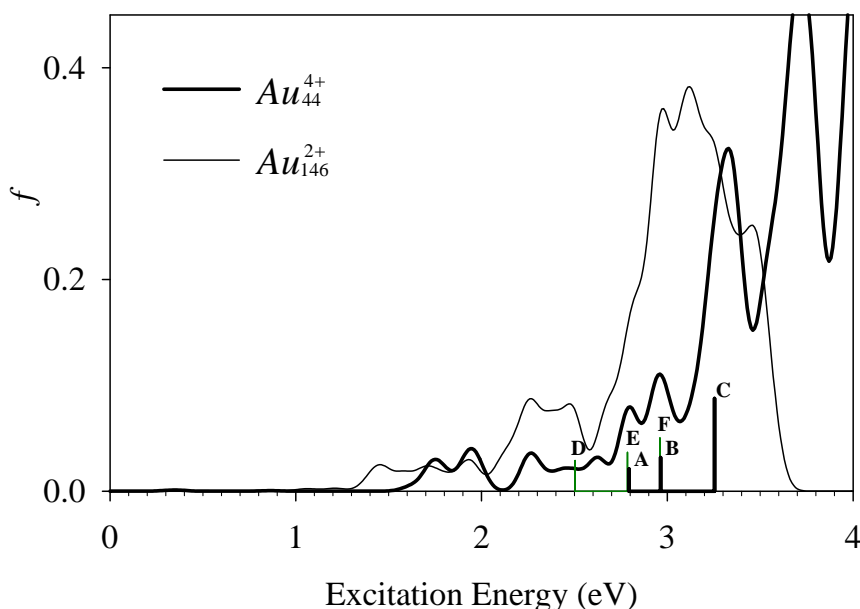


Figure 4.6 TDDFT valence excitation spectra (oscillator strength vs excitation energy) of Au_{44}^{4+} and Au_{146}^{2+} calculated with DZ basis set, convoluted spectra obtained with gaussian broadening with FWHM = 0.12 eV are reported as solid lines (thick line for Au_{44}^{4+} and thin line for Au_{146}^{2+}). Only the most intense discrete transitions are reported as vertical lines, labelled as **A B C** and **D E F** respectively for Au_{44}^{4+} and Au_{146}^{2+} .

Such effect seems to be present also in this case: in fact the spectrum of Au_{44}^{4+} resembles to some extent the spectrum of Au_{146}^{2+} , apart a blue shift to higher energy. Notice that the shift is about 0.2 eV in the low energy region and is more pronounced (around 0.4 eV) for the spectral features at 3 eV of excitation energy. It is not easy to give a simple interpretation of the theoretically predicted blue shift with decreasing size, in fact the effect might be rationalized in two different ways: one possibility could be that in Au_{146}^{2+} the transitions do not change appreciably their energy positions with respect to Au_{44}^{4+} but gain intensity in the low energy region, the other possibility could be that in Au_{146}^{2+} the transitions keep their nature but are actually shifted to lower energy. The second possibility is usually employed in the literature to discuss the blue shift, and is rationalized in terms of the "spilling out" of the electrons outside the cluster surface: this effect is expected to gain importance with increasing cluster size and should decrease the transition energy. In order to describe the nature of the electron transitions involved in the optical spectra, we have selected three excitations with major intensity, labelled **A** ($26E_u$), **B** ($34E_u$), **C** ($53E_u$), and **D** ($162E_u$), **E** ($209E_u$), **F** ($262E_u$), respectively for Au_{44}^{4+} and Au_{146}^{2+} , reported in Figure 4.6 and whose nature is considered in detail in Tables 4.2 and 4.3 (reported at the end of the chapter). The analysis of the excited state composition indicates immediately the collective nature of the excitation, each transition considered is contributed by many different excited configurations. Moreover the nature of the final orbitals for both clusters is of sp type with rather low d contribution, while the initial orbitals display a more pronounced d contribution, which is higher in Au_{44}^{4+} with respect to Au_{146}^{2+} . This is consistent with the assignment of such features to $sp \leftarrow d$ interband transitions, but with a non negligible amount of $sp \leftarrow sp$ intraband transitions, these latter are more important in Au_{146}^{2+} .

4.5. CONCLUSIONS

The valence optical excitation spectra of the series Au_6^{4+} , Au_{44}^{4+} and Au_{146}^{2+} have been calculated at the scalar relativistic TDDFT level of the theory. For Au_6^{4+} it has been possible to give a rationalization of the results in terms of conventional quantum chemistry arguments: analysis of the excited states in terms of one-electron excited configurations and the molecular

orbitals involved. For the larger clusters such procedure is much less practical, due to the much higher density of states in the valence region and to the superposition of all three s , p and d bands in the region near the Fermi level. Although experimental data for comparison are available only for gold clusters protected by ligands, they are consistent with present calculations.

Future theoretical work in this field may be considered in various directions: for example thiolic ligands may be added to the present gold clusters and their effect on the optical properties may be discussed in terms of the transition density. Another possibility could be an analogue study on naked silver clusters: for silver it is well known that the $4d$ manifold does not play a fundamental role like in gold clusters, so by appropriate frozen core scheme up to $4d$ it could be possible to study clusters of even larger size, approaching the regime where the SPR becomes to appear.

Another possible field for future developments could be the design of new computational TDDFT algorithms to treat much larger systems with reasonable efforts, keeping an accurate treatment of the electronic structure (avoiding crude approximation like the *jellium*) necessary to reproduce correctly the effects of chemical bonds, but solving the response TDDFT equations with a simplified scheme, for example avoiding to work in the large $1h-1p$ space of the density matrix. A very promising scheme in this direction has recently appeared in the literature.^{4.39} Another possible solution may be to extract the excitation spectrum performing many calculations of the dynamic polarizability at complex frequencies with an algorithm based on the density instead of the density matrix.^{4.40}

We may conclude saying that the recent diffuse and growing interest on nanosized systems is challenging quantum chemists to apply traditional algorithms discussing their results with new paradigms and to propose new algorithms to extend the frontier of applicability of accurate methods.

4.5.1 Acknowledgements

This work has been supported by grants from MIUR (Programmi di Ricerca di Interesse Nazionale COFIN 2004 and FIRB 2001) of Italy, from Consorzio Interuniversitario Nazionale per la Scienza e Tecnologia dei Materiali (INSTM) (Progetto PRISMA 2004) and CNR of Rome (Italy) and from INFN DEMOCRITOS National Simulation Center, Trieste, Italy.

Table 4.1

Excitation	E_{exc} (eV)	f^a	excited state composition ^b
10E _u	4.64	0.208	27% 3b _{1g} (6s 1%, 5d 99%) → 9e _u (6s 67%, 6p 18%, 5d 15%) 47% 7a _{1g} (6s 57%, 6p 5%, 5d 39%) → 9e _u (6s 67%, 6p 18%, 5d 15%) 11% 6a _{1g} (5d) → 9e _u (6s 67%, 6p 18%, 5d 15%)
5A _{2u}	4.64	0.104	47% 7a _{1g} (6s 57%, 6p 5%, 5d 39%) → 6a _{2u} (6s 67%, 6p 18%, 5d 15%) 38% 6a _{1g} (5d) → 6a _{2u} (6s 67%, 6p 18%, 5d 15%)
17E _u	6.55	0.123	67% 5a _{1g} (6s 30%, 6p 12%, 5d 61%) → 9e _u (6s 67%, 6p 18%, 5d 15%) 18% 6e _u (5d) → 9a _{1g} (6s 79%, 6p 18%, 5d 2%) 6% 6e _u (5d) → 6b _{1g} (6s 79%, 6p 18%, 5d 2%)
19E _u	6.79	0.127	51% 6e _u (5d) → 9a _{1g} (6s 79%, 6p 18%, 5d 2%) 19% 6e _u (5d) → 6b _{1g} (6s 79%, 6p 18%, 5d 2%) 14% 5a _{1g} (6s 30%, 6p 12%, 5d 61%) → 9e _u (6s 67%, 6p 18%, 5d 15%)
21E _u	7.77	0.215	58% 5e _u (6s 8%, 6p 3%, 5d 88%) → 6b _{1g} (6s 79%, 6p 18%, 5d 2%) 18% 5e _u (6s 8%, 6p 3%, 5d 88%) → 9a _{1g} (6s 79%, 6p 18%, 5d 2%) 7% 8e _u (5d) → 4b _{2g} (6p 99%, 5d 1%) 7% 3b _{2u} (5d) → 6e _g (6p)
11A _{2u}	7.77	0.107	77% 4a _{2u} (6s 8%, 6p 3%, 5d 88%) → 9a _{1g} (6s 79%, 6p 18%, 5d 2%) 13% 8e _u (5d) → 6e _g (6p)
23E _u	8.42	0.203	29% 1a _{1u} (5d) → 6e _g (6p) 29% 3b _{2u} (5d) → 6e _g (6p) 27% 8e _u (5d) → 4b _{2g} (6p 99%, 5d 1%) 10% 2b _{1u} (5d) → 6e _g (6p)
26E _u	8.74	0.369	39% 1a _{1u} (5d) → 6e _g (6p) 13% 2b _{1u} (5d) → 6e _g (6p) 10% 3b _{2u} (5d) → 6e _g (6p) 10% 8e _u (5d) → 4b _{2g} (6p 99%, 5d 1%) 6% 7e _u (5d) → 4b _{2g} (6p 99%, 5d 1%) 6% 5a _{2u} (6p 2%, 5d 98%) → 6e _g (6p)
13A _{2u}	8.74	0.189	51% 2b _{1u} (5d) → 4b _{2g} (6p 98%, 5d 1%) 20% 8e _u (5d) → 6e _g (6p) 12% 7e _u (5d) → 6e _g (6p)
28E _u	9.16	0.176	39% 7e _u (5d) → 4b _{2g} (6p 99%, 5d 1%) 38% 5a _{2u} (6p 2%, 5d 98%) → 6e _g (6p) 9% 7e _u (5d) → 10a _{1g} (6s 17%, 6p 80%, 5d 1%)
29E _u	9.48	0.222	75% 7e _u (5d) → 10a _{1g} (6s 17%, 6p 80%, 5d 1%) 8% 5e _g (5d) → 7a _{2u} (6s 9%, 6p 90%) 8% 2a _{2g} (5d) → 10e _u (6s 9%, 6p 90%)
15A _{2u}	9.48	0.114	75% 5a _{2u} (6p 2%, 5d 98%) → 10a _{1g} (6s 17%, 6p 80%, 5d 1%) 16% 5e _g (5d) → 10e _u (6s 9%, 6p 90%)
36E _u	10.24	0.952	29% 2a _{2g} (5d) → 10e _u (6s 9%, 6p 90%) 28% 5e _g (5d) → 7a _{2u} (6s 9%, 6p 90%) 8% 4e _g (5d) → 7a _{2u} (6s 9%, 6p 90%) 8% 3b _{2g} (5d) → 10e _u (6s 9%, 6p 90%) 7% 4b _{1g} (5d) → 10e _u (6s 9%, 6p 90%) 4% 7e _u (5d) → 10a _{1g} (6s 17%, 6p 80%, 5d 1%)
18A _{2u}	10.24	0.461	56% 5e _g (5d) → 10e _u (6s 9%, 6p 90%) 10% 8a _{1g} (5d) → 7a _{2u} (6s 9%, 6p 90%) 15% 4e _g (5d) → 10e _u (6s 9%, 6p 90%)

19A _{2u}	10.34	0.143	6% 5e _g (5d) → 10e _u (6s 9%, 6p 90%) 81% 8a _{1g} (5d) → 7a _{2u} (6s 9%, 6p 90%) 4% 4e _g (5d) → 10e _u (6s 9%, 6p 90%) 5% 5e _u (6s 8%, 6p 3%, 6d 88%) → 6e _g (6p)
38E _u	10.35	0.254	61% 4b _{1g} (5d) → 10e _u (6s 9%, 6p 90%) 22% 8a _{1g} (5d) → 10e _u (6s 9%, 6p 90%)
42E _u	10.72	0.952	38% 3b _{2g} (5d) → 10e _u (6s 9%, 6p 90%) 32% 4e _g (5d) → 7a _{2u} (6s 9%, 6p 90%) 5% 7a _{1g} (6s 57%, 6p 5%, 5d 39%) → 10e _u (6s 9%, 6p 90%) 5% 5e _g (5d) → 7a _{2u} (6s 9%, 6p 90%) 4% 2a _{2g} (5d) → 10e _u (6s 9%, 6p 90%)
21A _{2u}	10.72	0.472	9% 5e _g (5d) → 10e _u (6s 9%, 6p 90%) 5% 7a _{1g} (6s 57%, 6p 5%, 5d 39%) → 7a _{2u} (6s 9%, 6p 90%) 71% 4e _g (5d) → 10e _u (6s 9%, 6p 90%) 4% 5e _u (6s 8%, 6p 3%, 6d 88%) → 6e _g (6p)
50E _u	12.37	0.289	40% 5e _g (5d) → 4b _{2u} (6p 98%, 5d 2%) 36% 2a _{2g} (5d) → 11e _u (6p 98%, 5d 2%) 9% 2b _{2g} (6s 1%, 5d 99%) → 10e _u (6s 9%, 6p 90%) 8% 3e _g (5d) → 7a _{2u} (6s 9%, 6p 90%)
26A _{2u}	12.37	0.148	76% 5e _g (5d) → 11e _u (6p 98%, 5d 2%) 17% 3e _g (5d) → 10e _u (6s 9%, 6p 90%) 2% 5b _{1g} (5d) → 4b _{2u} (6p 98%, 5d 2%) 2% 5a _{1g} (6s 30%, 6p 12%, 5d 61%) → 7a _{2u} (6s 9%, 6p 90%)
51E _u	12.43	0.574	45% 5b _{1g} (5d) → 11e _u (6p 98%, 5d 2%) 12% 2b _{2g} (6s 1%, 5d 99%) → 10e _u (6s 9%, 6p 90%) 11% 3e _g (5d) → 7a _{2u} (6s 9%, 6p 90%) 11% 8a _{1g} (5d) → 11e _u (6p 98%, 5d 2%)
27A _{2u}	12.43	0.284	3% 5e _g (5d) → 11e _u (6p 98%, 5d 2%) 24% 3e _g (5d) → 10e _u (6s 9%, 6p 90%) 46% 5b _{1g} (5d) → 4b _{2u} (6p 98%, 5d 2%) 15% 4b _{1g} (5d) → 4b _{2u} (6p 98%, 5d 2%) 5% 4e _g (5d) → 11e _u (6p 98%, 5d 2%) 2% 5a _{1g} (6s 30%, 6p 12%, 5d 61%) → 7a _{2u} (6s 9%, 6p 90%)
53E _u	12.74	0.377	61% 8a _{1g} (5d) → 11e _u (6p 98%, 5d 2%) 18% 4b _{1g} (5d) → 11e _u (6p 98%, 5d 2%) 6% 5b _{1g} (5d) → 11e _u (6p 98%, 5d 2%) 6% 3b _{2g} (5d) → 11e _u (6p 98%, 5d 2%) 5% 4e _g (5d) → 4b _{2u} (6p 98%, 5d 2%)
28A _{2u}	12.74	0.187	1% 3e _g (5d) → 10e _u (6s 9%, 6p 90%) 6% 5b _{1g} (5d) → 4b _{2u} (6p 98%, 5d 2%) 79% 4b _{1g} (5d) → 4b _{2u} (6p 98%, 5d 2%) 11% 4e _g (5d) → 11e _u (6p 98%, 5d 2%)
55E _u	13.09	0.387	36% 4e _g (5d) → 4b _{2u} (6p 98%, 5d 2%) 35% 3b _{2g} (5d) → 11e _u (6p 98%, 5d 2%) 16% 5a _{1g} (6s 30%, 6p 12%, 5d 6%) → 10e _u (6s 9%, 6p 90%)
29A _{2u}	13.09	0.191	1% 3e _g (5d) → 10e _u (6s 9%, 6p 90%) 3% 5b _{1g} (5d) → 4b _{2u} (6p 98%, 5d 2%) 4% 4b _{1g} (5d) → 4b _{2u} (6p 98%, 5d 2%) 1% 3b _{1g} (6s 1%, 5d 99%) → 4b _{2u} (6p 98%, 5d 2%) 71% 4e _g (5d) → 11e _u (6p 98%, 5d 2%) 17% 5a _{1g} (6s 30%, 6p 12%, 5d 61%) → 7a _{2u} (6s 9%, 6p 90%)

Table 4.1 E_u and A_{2u} valence excitation spectrum of Au_6^{4+} . Excitation energy (E_{exc}), oscillator strength (f) and excited state composition in terms of monoexcited configurations are reported.

^a: only the transitions with $f > 0.1$ are reported.

^b: the main contributions to the initial and final orbitals are reported in parenthesis

Table 4.2

Excitation	E_{exc} (eV)	f	excited state composition ^a
26E _u (A)	2.79	0.0210	41% 40a _{1g} (6s 5%, 5d 90%) → 59e _u (6s 50%, 6p 29%, 5d 13%) 21% 31b _{1g} (6s 6%, 6p 1%, 5d 89%) → 59e _u (6s 50%, 6p 29%, 5d 13%) 19% 20b _{1u} (6s 45%, 6p 35%, 5d 14%) → 47e _g (6s 6%, 6p 89%) 5% 58e _u (6s 42%, 6p 20%, 5d 26%) → 44a _{1g} (6s 57%, 6p 28%, 5d 10%)
34E _u (B)	2.96	0.0318	61% 57e _u (6s 38%, 6p 20%, 5d 38%) → 26b _{2g} (6s 53%, 6p 35%, 5d 7%) 15% 17a _{2g} (5d) → 59e _u (6s 50%, 6p 29%, 5d 13%) 6% 41e _g (6s 7%, 5d 87%) → 34a _{2u} (6s 50%, 6p 30%, 5d 16%) 5% 20b _{1u} (6s 45%, 6p 35%, 5d 14%) → 47e _g (6s 6%, 6p 89%)
53E _u (C)	3.25	0.0877	25% 13a _{1u} (5d) → 45e _g (6s 48%, 6p 32%, 5d 9%) 17% 55e _u (5d) → 20a _{2g} (6s 49%, 6p 35%, 5d 10%) 11% 57e _u (6s 38%, 6p 20%, 5d 38%) → 34b _{1g} (6s 57%, 6p 28%, 5d 10%) 9% 37a _{1g} (5d) → 59e _u (6s 50%, 6p 29%, 5d 13%) 9% 57e _u (6s 38%, 6p 20%, 5d 38%) → 44a _{1g} (6s 57%, 6p 28%, 5d 10%) 4% 42a _{1g} (6s 51%, 6p 34%, 5d 8%) → 62e _u (6s 61%, 6p 28%)

Table 4.2 Main contributions to E_u valence excitation spectrum of Au_{44}^{4+} . Excitation energy (E_{exc}), oscillator strength (f) and excited state composition in terms of monoexcited configurations are reported.

^a: the main contributions to the initial and final orbitals are reported in parenthesis

Table 4.3

Excitation	E_{exc} (eV)	f	excited state composition ^a
162E _u (D)	2.50	0.0289	35% 98b _{1g} (5d) → 188e _u (6s 41%, 6p 22%, 5d 1%) 18% 119a _{1g} (6s 33%, 6p 21%, 5d 19%) → 191e _u (6s 47%, 6p 19%) 9% 156e _g (6s 41%, 6p 21%, 5d 6%) → 107a _{2u} (6s 47%, 6p 37%, 5d 1%) 8% 99b _{1g} (6s 26%, 6p 5%, 5d 49%) → 189e _u (6s 38%, 6p 24%, 5d 4%) 5% 71a _{2g} (6s 42%, 6p 27%, 5d 17%) → 194e _u (6s 43%, 6p 24%) 4% 100b _{1g} (6s 34%, 6p 26%, 5d 20%) → 191e _u (6s 47%, 6p 19%) 3% 83b _{2u} (6s 31%, 6p 13%, 5d 41%) → 158e _g (6s 44%, 6p 29%) 3% 183e _u (6s 31%, 6p 5%, 5d 30%) → 72a _{2g} (6s 45%, 6p 35%, 5d 10%)
209E _u (E)	2.78	0.0366	23% 186e _u (6s 40%, 6p 14%, 5d 14%) → 89b _{2g} (6s 48%, 6p 35%, 5d 2%) 21% 121a _{1g} (6s 45%, 6p 28%, 5d 7%) → 196e _u (6s 14%, 6p 67%) 18% 84b _{2g} (6s 36%, 6p 21%, 5d 28%) → 162e _g (6s 47%, 6p 34%) 4% 185e _u (6s 35%, 6p 15%, 5d 10%) → 105b _{1g} (6s 50%, 6p 28%, 5d 3%) 3% 155e _g (6s 36%, 6p 19%, 5d 15%) → 87b _{2u} (6s 50%, 6p 36%, 5d 3%)
262E _u (F)	2.95	0.0504	35% 187e _u (6s 33%, 6p 29%, 5d 3%) → 128a _{1g} (6s 54%, 6p 33%, 5d 1%) 16% 182e _u (5d) → 72a _{2g} (6s 45%, 6p 35%, 5d 10%) 7% 95b _{1g} (6s 3%, 5d 79%) → 189e _u (6s 38%, 6p 24%, 5d 4%) 7% 82b _{2u} (6s 1%, 5d 90%) → 158e _g (6s 44%, 6p 29%) 6% 115a _{1g} (6s 3%, 5d 80%) → 189e _u (6s 38%, 6p 24%, 5d 4%) 4% 95b _{1g} (6s 3%, 5d 79%) → 188e _u (6s 41%, 6p 22%, 5d 1%) 3% 115a _{1g} (6s 3%, 5d 80%) → 188e _u (6s 41%, 6p 22%, 5d 1%) 3% 154e _g (6s 36%, 6p 12%, 5d 20%) → 73b _{1u} (6s 48%, 6p 38%, 5d 1%)

Table 4.3 Main contributions to E_u valence excitation spectrum of Au_{146}^{2+} . Excitation energy (E_{exc}), oscillator strength (f) and excited state composition in terms of monoexcited configurations are reported.

^a: the main contributions to the initial and final orbitals are reported in parenthesis

5. SPIN-ORBIT EFFECTS IN THE PHOTOABSORPTION OF WAU₁₂ AND MOAU₁₂: A RELATIVISTIC TIME DEPENDENT DENSITY FUNCTIONAL STUDY

Stener, M.; Nardelli, A.; Fronzoni, G. *J. Chem. Phys.* **2008**, *128*, 134307.

The electronic structure of both WAu₁₂ and MoAu₁₂ has been calculated at the Density Functional Theory (DFT) level, employing the Zero Order Regular Approximation (ZORA) at both scalar relativistic level and including spin orbit coupling. The effect of the inclusion of the spin orbit coupling is discussed and the differences assigned to the nature of the encaged atom (W or Mo) are identified. Then the excitation spectra of both clusters are calculated at the TDDFT level, also in this case at both scalar relativistic and spin orbit level. The inclusion of spin orbit coupling is mandatory for an accurate description in the low energy region. At higher energy, where the density of states is higher, the convoluted intensity can be properly described already at the scalar relativistic level. The consequences of the spin orbit coupling on the excitation spectrum of the clusters indicates that while in WAu₁₂ the lowest excitations are essentially shifted in energy with respect to the scalar relativistic results, in MoAu₁₂ a dramatic splitting in many lines is actually predicted, revealing a quite different behaviour of the two clusters.

5.1. INTRODUCTION

Gold has a very rich chemistry, with many different aspects which have attracted the attention of both experimentalists^{5.1} and theoreticians.^{5.2,5.3} One of the most striking gold chemical property is its ability to surround main-group atoms to form cage-like structure,^{5.4} like, for example, in the octahedral cluster [(LAu)₆C]²⁺.^{5.5,5.6} More recently, Pyykkö and Runeberg^{5.7} have theoretically predicted the existence of the bimetallic cluster WAu₁₂, whose structure consists of a tungsten atom surrounded by an icosahedral cage of gold atoms. Soon after the monoanions of WAu₁₂ and its isoelectronic omologue MoAu₁₂ have been produced in

laboratory and characterized by mass spectrometry and photodetachment.^{5.8} The existence of such stable closed-shell $W\text{Au}_{12}$ system has encouraged speculations on the possibility to produce new materials built with repeated $W\text{Au}_{12}$ units,^{5.7} such possibility becomes to be realistic nowadays, as demonstrated by the recent discovery of a biicosahedral Au_{25} cluster stabilized by ligands:^{5.9} in the latter case two icosahedral Au_{13} cluster units are condensed with a common vertex.

The interest on gold clusters and in their potential usage to build new materials, is also due to their optical properties, in particular photoabsorption, which may present peculiar behaviours especially in nanosized systems.^{5.10} Therefore we have considered interesting to perform a theoretical study on the photoabsorption of both $W\text{Au}_{12}$ and MoAu_{12} , in order to assess the importance of spin-orbit coupling effects, the connection of the spectral features with the electronic structure and, more specifically, to identify the main differences induced by the nature of the encapsulated metal.

The theoretical description of gold compounds, requires the inclusion of relativistic effects, whose role has been exhaustively discussed in a recent review by Pyykkö.^{5.2} In particular it is known since almost 30 years that gold atom suffers the largest relativistic relative $6s$ contraction for elements up to an atomic number $Z = 100$,^{5.11} a phenomenon caused by the direct relativistic contraction of $1s$ core orbital. Therefore the valence $6s$ orbital is stabilized by the relativistic contraction of the core $1s$ orbital as an effect of orthogonality, while the same contraction is a more efficient screen of the nuclear charge felt by the $5d$ orbital, which is in turn destabilized. The major chemical implication of these two effects is the strong reduction of the $5d - 6s$ energy gap, therefore a strong hybridization is observed between d and s bands in gold clusters.

The relatively recent awareness of the importance of relativity in quantum chemistry has promoted the development of various theoretical schemes and their implementation in computer codes. Despite gold chemistry, also applications to compounds of actinides and trans-uranic elements have recently bloomed, sometime giving very surprising results like, for example, the presence of a quintuple bond in U_2 .^{5.12}

Since the main goal of the present work is the accurate description of the photoabsorption spectra of both $W\text{Au}_{12}$ and MoAu_{12} , we have employed the recent formalism based on the relativistic two-component Zeroth-Order Regular Approximation (ZORA) with Spin Orbit (SO) coupling and Time-Dependent Density Functional Theory (TDDFT), as implemented in the ADF code.^{5.13} Such choice, to our knowledge, should represent at the moment the scheme which includes all the most relevant physical effects involved in the photoabsorption, ranging

from the configuration mixing of TDDFT to the SO coupling, and thanks to its excellent performance can be applied to cluster of moderate size and high symmetry with reasonable efforts.

5.2. THEORETICAL METHOD

In this section we briefly recall the relativistic two-component ZORA-TDDFT method, which is extensively described in the literature,^{5,13} to which we refer the reader for further details. This method allows the calculation of excitation energies and intensities for closed shell molecules, including spin-orbit coupling and with full use of symmetry. The equation which is actually solved is the eigenvalue equation:

$$\Omega F_I = \omega_I^2 F_I \quad (5.1)$$

$$\Omega_{ia\sigma,jb\tau} = \delta_{\sigma\tau} \delta_{ij} \delta_{ab} (\varepsilon_a - \varepsilon_i)^2 + 2\sqrt{(\varepsilon_a - \varepsilon_i)} \frac{\partial F_{ia}}{\partial P_{jb}} \sqrt{(\varepsilon_b - \varepsilon_j)} \quad (5.2)$$

in (5.2) indices i and j indicate occupied spinors and indices a and b indicate virtual spinors, ε_i and ε_a are molecular spinor energies, while F and P are Fock matrix and density matrix respectively.

In Equation (5.1) the eigenvalues ω_I^2 correspond to the squared of the excitation energies, while from the eigenvectors F_I the oscillator strengths can be extracted according to standard TDDFT method.^{5,14} An explicit expression in terms of spinors and exchange-correlation functional can be given for the coupling matrix elements $\frac{\partial F_{ia}}{\partial P_{jb}}$ for closed shell systems,^{5,13} if

the Adiabatic Local Density Approximation (ALDA) is employed for the exchange correlation kernel, the noncollinear scheme is used for the exchange correlation potential and the ZORA kinetic term is neglected in the construction of the response matrix.

The Equation (5.1) is solved with Davidson's iterative algorithm. The implementation takes advantages of auxiliary basis function, which are used to fit the induced density and to calculate efficiently the product between the Ω matrix and a trial vector.^{5,15} Another

fundamental aspect of the implementation is the use of molecular symmetry, which is very convenient if the molecule is highly symmetric, as in the present case.

5.3. COMPUTATIONAL DETAILS

In the present calculations we have employed both Scalar Relativistic (SR) as well as SO ZORA formalism, implemented in the ADF^{5.16} code (version 2006.01). Basis sets consisting of Slater Type Orbitals (STO) have been employed, of triple-zeta plus polarization (TZP) size for valence, while core electrons have been kept frozen up to $4f$ for Au and W, and up to $4p$ for Mo. In all calculations we have employed the LB94 exchange-correlation potential,^{5.17} since its correct coulombic asymptotic behaviour has proven important for an accurate description of virtual orbitals involved in the valence electron excitations.^{5.18} The more recent asymptotically correct SAOP^{5.19} potential has not been considered here because it performs like LB94 for gold clusters TDDFT calculations,^{5.20} furthermore it does not allow the frozen core scheme, so for computational economy we have chosen LB94. For gold clusters we did not observe the deterioration of performances of LB94 with respect to SAOP recently reported for uranium compounds.^{5.21} A promising alternative exchange-correlation functional suited for TDDFT calculations is the hybrid CAM-B3LYP functional,^{5.22} which has the correct asymptotic behaviour and has proven successful for the description of charge transfer transitions.^{5.23} However at the moment the ADF program cannot employ hybrid functionals in the TDDFT calculations, so we cannot test its performances in the present systems. Future extensions of the ADF code to include hybrid functionals in the TDDFT routines are therefore worth considering.

The optimized geometries of the clusters, employed in the present calculations, have been taken from the literature.^{5.8}

5.4. RESULTS AND DISCUSSION

5.4.1. WAu₁₂ electronic structure

The rationalization of the photoabsorption spectrum in terms of electronic excitations needs the knowledge of the electronic structure of the system under study. Therefore we start the discussion with an analysis of the electronic structure of WAu₁₂ in more detail than previous works.^{5.7,5.8,5.24} The Molecular Orbitals (MO) obtained from a Scalar Relativistic (SR) ZORA TZP LB94 calculation are reported in the left side of Figure 5.1, ordered according to the KS eigenvalues. The MO's have been labelled according to the Irreducible Representations (Irreps) of the icosahedral point group I_h .

It is very natural to rationalize the electronic structure of WAu₁₂ as the interaction between the W atom and a Au₁₂ cage, the latter previously formed by 12 Au atoms, such process is considered as well in the correlation diagram reported in Figure 5.1.

Let's start with the formation of the Au₁₂ cage from free Au atoms: from each gold atom with electronic configuration $5d^{10}6s^1$ a set of symmetrized molecular orbitals are formed: a completely filled $5d$ manifold and an open shell from the atomic $6s$ orbitals, while $6p$ orbitals contribute to the higher energy virtual orbitals. More precisely, from twelve $6s$ atomic functions at the vertexes of an icosahedron, the following symmetry adapted linear combinations are obtained: $a_g + t_{1u} + h_g + t_{2u}$ (ordered by increasing energy) which are occupied according the aufbau giving the following electron configuration: $a_g^2 t_{1u}^6 h_g^4$ so the five-fold degenerate h_g orbital is partially filled by 4 electrons. The energy positions of such orbitals (obtained from a restricted calculation) have been reported individually in Figure 5.1 for the Au₁₂ cage. This picture is actually simplified, in fact the SR $5d - 6s$ atomic energy gap is only 1.63 eV, therefore a significant hybridization occurs between molecular orbitals of s and d atomic character belonging to the same Irrep. The five $5d$ atomic functions belonging to the twelve gold atoms can be properly adapted to the I_h point group symmetry: they give rise to sixty symmetrized functions belonging to the following Irreps: $a_g + t_{1g} + t_{2g} + 2g_g + 3h_g + 2t_{1u} + 2t_{2u} + 2g_u + 2h_u$. They have not been reported individually in Figure 5.1, but rather we have indicated the energy region they span by a shaded dark grey area. Finally virtual orbitals with main atomic $6p$ contribution span the high energy region, reported as a light grey area, only lowest orbitals (involved as final states in the photoabsorption process) are individually reported in the figure.

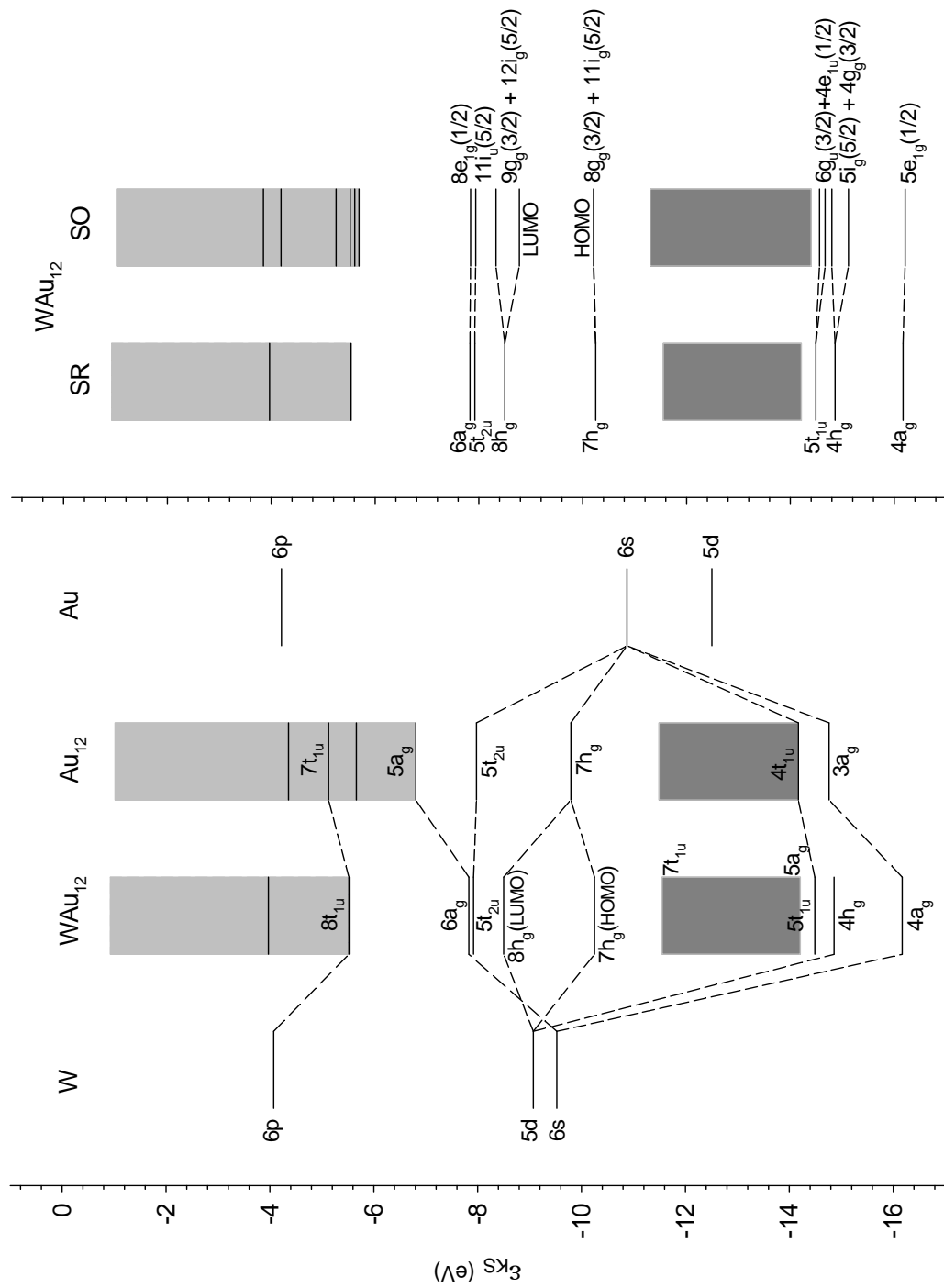


Figure 5.1 Left side: correlation diagram of the molecular orbitals of WAu₁₂ in terms of Au₁₂ cage and W atom, scalar relativistic eigenvalues are reported, orbitals are classified according to I_h point group symmetry. Right side: correlation diagram between the scalar relativistic molecular orbitals and the spin orbit spinors of WAu₁₂, orbitals and spinors are classified according to I_h and I_h^2 point group symmetry respectively.

The next step consists in the inclusion of the W atom within the cage and also this is considered in Figure 5.1. Let's start with the 6s W orbital, which can interact only with cage orbitals with a_g symmetry: the $W_{Au_{12}} 4a_g$ MO results from a bonding interaction between the W 6s atomic orbital (19%) and the $3a_g Au_{12} 6s$ (49%) with some Au 5d (25%), confirming a significant degree of 6s - 5d hybridization. Interestingly, the next $5a_g$ MO retains its Au 5d cage character and does not interact with the W atom, while the virtual $6a_g$ MO has a significant participation of W 6s (20%), Au 6p (49%) and Au 6s (29%).

The 5d W atomic orbital plays a key role in the electronic structure of the $W_{Au_{12}}$ cluster, in fact it transforms according to the h_g Irrep and therefore can profitably interact with the Au_{12} fragment $7h_g$ MO which lies near in energy and contains 4 electrons. For this reason it is easy to understand the high stability of the $W_{Au_{12}}$ cluster: the inclusion of a transition metal (W) with d^6 configuration furnishes 6 additional electrons to completely fill the h_g orbital, obtaining a stable closed shell electronic structure. The result is a couple of MOs, $7h_g$ (HOMO) and $8h_g$ (LUMO), being the bonding and antibonding counterparts of the interaction between W 5d and $Au_{12} 7h_g$, the W 5d contribution is roughly twice higher in the LUMO (47%) than in the HOMO (23%).

Above the $8h_g$ (LUMO) orbital, there are two almost degenerate orbitals: the $6a_g$ which has been already discussed, and $5t_{2u}$ one with 78% Au 6s and 14% Au 6p composition. Going at higher energies, the $4g_u$ orbital is formed essentially by only Au 6p atomic functions, while next $8t_{1u}$ contains a significant contribution (20%) of W 6p. As already observed in pure gold clusters,^{5,20} the atomic 6p contribution starts to become important in virtual orbitals well above the LUMO. This completes the electronic structure description at the SR ZORA level.

The next step is to consider the inclusion of the spin orbit coupling in the electronic structure calculation of $W_{Au_{12}}$, which we have performed at the SO ZORA level. Before to discuss the results, it is important to assess the effects of the SO coupling in terms of symmetry: when the SO is included in the calculation, the electronic structure is described in terms of spinors, whose symmetry behaviours are obtained from the icosahedral double group. A complete discussion of the icosahedral double group I_h^2 , including character tables, is available in the literature.^{5,25} The most relevant effect of the SO coupling is the reduction of the degeneracy going from the molecular orbitals to the SO spinors, from character tables^{5,25} it can be shown that the splitting takes place according to Table 5.1. With this in mind, it is possible to start the discussion of the SO results, and to compare the energy levels between SR and SO $W_{Au_{12}}$ results in the right side of Figure 5.1. The most interesting feature is the different effect of the SO coupling over the HOMO ($7h_g$) and LUMO ($8h_g$) molecular orbitals, which belong to the

same Irrep: $7h_g$ is split in $8g_g(3/2)$ and $11i_g(5/2)$ with an energy gap of less than 0.01 eV, while $8h_g$ is split in $9g_g(3/2)$ and $12i_g(5/2)$ with an energy gap of 0.45 eV, in good agreement with previous calculations.^{5,8} This different behaviour may be ascribed to the larger participation of W $5d$ atomic contribution in the $8h_g$ (LUMO), thus reflecting the W $5d_{3/2}/5d_{5/2}$ atomic gap which we have calculated to be 0.64 eV. The d band is also affected by SO coupling, in fact (Figure 5.1) the energy range of the d band is larger in SO (3.15 eV) than in SR (2.72 eV) calculations. For the inner orbitals $5t_{1u}$ and $4h_g$ a SO splitting of 0.11 eV and 0.32 eV is calculated respectively. The two virtual molecular orbitals just above the LUMO, $5t_{2u}$ and $6a_g$, are not affected by SO splitting (see Table 5.1), while the next ones $4g_u$ and $8t_{1u}$ with high Au $6p$ contribution and separated by only 0.02 eV give rise to four different spinors which span an energy range of 0.44 eV.

I_h	I_h^2
A_g	$E_{1g}(1/2)$
T_{1g}	$E_{1g}(1/2) + G_g(3/2)$
T_{2g}	$I_g(5/2)$
G_g	$E_{2g}(7/2) + I_g(5/2)$
H_g	$G_g(3/2) + I_g(5/2)$
A_u	$E_{1u}(1/2)$
T_{1u}	$E_{1u}(1/2) + G_u(3/2)$
T_{2u}	$I_u(5/2)$
G_u	$E_{2u}(7/2) + I_u(5/2)$
H_u	$G_u(3/2) + I_u(5/2)$

Table 5.1 Resolution of the Irreducible Representations of the icosahedral group (I_h) in those of the icosahedral double group (I_h^2).

The electronic structure just considered will be necessary in the next section to discuss the electron excitations which take place during photoabsorption, however a direct comparison with the experiment could be possible in principle between the eigenvalues of the levels reported in Figure 5.1 and the measured Ionization Energies of the cluster. The latter are actually available only for the anion WAu_{12}^- , obtained from photodetachment measurement,^{5,8} so the comparison can be only qualitative. We may compare the eigenvalues

differences, with respect to the energy differences in the spectral experimental features: the experimental HOMO/LUMO gap (feature X and B of figure 1 of Ref. 5.8) of 1.8 eV is consistent with the SR and SO calculated values, which are 1.75 eV and 1.43 eV respectively. In the experimental spectrum the feature B (attributed to $7h_g$) is separated by about 0.9 eV from the next broad feature which can be ascribed to the beginning of ionization from the Au $5d$ band, such spacing is calculated to be 1.30 eV and 1.09 eV for SR and SO schemes respectively.

5.4.2. WAu₁₂ SR and SO TDDFT photoabsorption spectra

The TDDFT excitation spectra of WAu₁₂, calculated at both SR and SO level, have been reported in Figure 5.2 up to 6 eV of excitation energy, while the sketches of the spectra calculated up to 12 eV have been reported as insets inside the figure. Due to the high number of discrete lines it is not convenient to discuss them individually, however we have selected some important excitations (lines) of the spectra and analysed them in detail in Table 5.2 (reported at the end of the chapter) at both SR and SO level.

It is convenient to start the discussion with the SR low energy results (upper box of Figure 5.2) and Table 5.2: the spectrum is characterized by three well separated lines at low energy: 2.69 ($2T_{1u}$), 3.23 ($4T_{1u}$) and 3.81 eV ($9T_{1u}$), respectively, the intensity of the first excitation is roughly one half of the other two. In the last column of Table 5.2 we have reported also the excited state composition: in fact Casida^{5,14} has shown that at the TDDFT level each electron excitation is represented by a linear combination consisting of only one-electron ($1h - 1p$) excited configurations. This means that only one-electron excitations are present in the TDDFT spectrum, while multi-electron ones are absent. Therefore, still at the one-electron level, the TDDFT scheme allows mixing between one-electron configurations, taking into account the most important contribution of the configuration mixing. The inclusion of higher order multi-electron configurations within TDDFT in principle might be done at the exchange-correlation kernel level, this means in practice to go beyond the presently employed ALDA. However at the moment, although some progresses have appeared in the literature,^{5,26,5.27} there are no computer codes available to treat multi-electron excitations at the TDDFT level.

Going back to the discussion of the three $2T_{1u}$, $4T_{1u}$ and $9T_{1u}$ excited state compositions (last column of Table 5.2) we find that there is only one leader configuration which contributes to the excited states, in all cases for more than 80%. More precisely $2T_{1u}$ corresponds to the

transition from $7h_g$ HOMO to $5t_{2u}$ orbital, therefore it can be classified, in analogy of gold clusters,^{5,20} as mainly an $s \leftarrow s$ gold intraband transition, but including a 23% of W $5d$ contribution in the initial band.

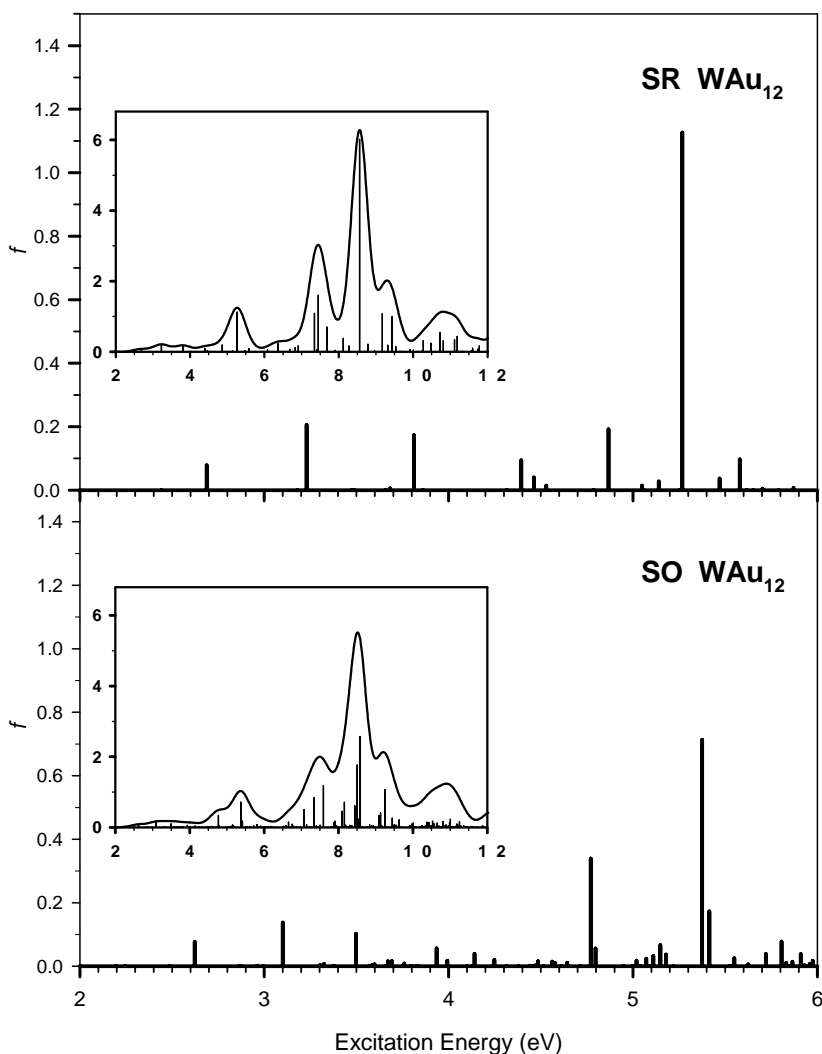


Figure 5.2 Scalar relativistic (SR, upper panel) and spin-orbit (SO, lower panel) TDDFT excitation spectrum of WAu_{12} , in the low energy region up to 6 eV. The spectra calculated up to 12 eV are reported as insets, together with the convolution of discrete lines with Gauss functions of 0.5 eV FWHM.

$4T_{1u}$ consists by 81% of a transition from $7t_{1u}$ MO belonging to the Au cage (Au $6s$ 40% and Au $5d$ 50%) to LUMO ($8h_g$) with W $5d$ 47% character, so a kind of charge transfer transition from gold cage to the central W atom. The next important transition $9T_{1u}$ consists again by 89% of a transition from $7t_{1u}$ MO to $6a_g$ final orbital, the latter has a 49% Au $6p$ contribution, so the transition may be classified mainly as a $p \leftarrow s$ gold interband transition. Going to higher energies, we encounter the $12T_{1u}$ transition at 4.39 eV, which is rather weak compared to the previous ones, and whose character is $8h_g$ (LUMO) $\leftarrow 4t_{2u}$ for 57%, it corresponds to a charge transfer from Au $5d$ to W $5d$. The next $18T_{1u}$ transition at 4.87 eV gains again more

intensity, and from its composition can be classified as a transition from HOMO to Au $6p$ virtual band. Next we find the strongest transition, namely the $24T_{1u}$ at 5.27 eV with an intensity more than five times higher than previous ones, also in this case its character is mainly from HOMO to Au $6p$ virtual band.

Now we will take into account the same energy range on the excitation spectrum calculated including the SO coupling, considered in the lower panel of Figure 5.2 and in Table 5.2. The three lowest energy SO transitions are the $8T_{1u}$ (at 2.62 eV), $13T_{1u}$ (3.10 eV) and $24T_{1u}$ (3.50), their composition indicates that they correspond to the SR $2T_{1u}$ (2.69 eV), $4T_{1u}$ (3.23 eV) and $9T_{1u}$ (3.81 eV) respectively, so the main effect of the SO coupling is a moderate red shift of 0.31 eV for the largest case, with a concomitant intensity reduction. The next important transition $77T_{1u}$ is calculated at 4.77 eV and can be assigned for 84% to the SR $18T_{1u}$, in this case a red shift of only 0.10 eV is calculated, but the intensity is almost doubled with respect to the SR calculation. The following strong line $90T_{1u}$ at 5.38 eV consists of a complete mixing of the SR $24T_{1u}$ (30%), $26T_{1u}$ (15%) and $22T_{1u}$ (7%) and is followed by the less intense $92T_{1u}$ (at 5.41 eV) assigned to the SR $26T_{1u}$. We can summarize these findings saying that the SO coupling with respect to a SR approach does not change the nature of the low lying transitions, giving a moderate red shifts of few tenths of eV and generally an intensity reduction, but for higher energy transition (above 5 eV) the SO coupling tends to mix different configurations so the nature of the transition is different.

In the two insets inside Figure 5.2 we have considered the excitation spectrum up to 12 eV, at both SR and SO levels, in this case the density of the transitions is quite high so we have convoluted the discrete lines with gaussian functions of FWHM = 0.5 eV to allow an easier comparison of the intensity distribution within the spectrum. At first sight we may say that although the discrete lines distribution appears quite different according to the scheme employed, on the other hand the convoluted profiles show only small differences, indicating that the intensity distribution is not strongly affected by the SO coupling.

In this case we will limit the discussion only to the energy range from 6 eV up to 12 eV, since the lower energy spectrum has been already considered, moreover it is worth discussing only the most intense lines, which are responsible for the salient features which can be observed in the convoluted profile. Starting with the SR results (see also Table 5.2) the strongest absorption is found at 8.56 eV assigned to the $63T_{1u}$ transition. Such transition is the result of many one-electron excited configurations, the leading term being $9h_g \leftarrow 3h_u$ (30%) and $9h_g \leftarrow 3g_u$ (21%), so it consists in a typical strong gold interband $p \leftarrow d$ transition, however the arrival gold p band is hybridized with an important (23%) contribution of W $5d$. Such strong

band is preceded by an important spectral feature in the energy range 7.35 - 7.68 eV, contributed by three different transitions: $45T_{1u}$, $48T_{1u}$ and $50T_{1u}$. From the inspection of the excited state contribution all of them can be assigned as main gold interband $p \leftarrow d$ transitions. Now let's consider the high energy region at the SO level: the strongest feature around 8.5 eV is now the result of two transitions, separated by only 0.07 eV, namely $226T_{1u}$ and $232T_{1u}$. By inspection of their compositions, it is surprising that neither of them has significant contribution from the SR $63T_{1u}$, although the character of gold interband $p \leftarrow d$ transitions is preserved. In fact at first sight one would have reasonably supposed that the SO lines could have been simply the result of a split of the SR transition in more components. We attribute the missing of correlation between the SR and SO feature around 8.5 eV to the very high density of state in this region: the quasi-degenerate state can completely mix as an effect of a perturbation, that is the difference in the hamiltonian passing from SR to SO. This holds for both excited state compositions in terms of one-electron excited configurations, as well as for spinor and orbitals. In fact from an analysis of the nature of the spinors (not reported in the table), it is found that they cannot be in general classified only simply as split components of the SR molecular orbitals according to Table 5.1. More precisely within the SO d band in the energy range between -11.65 eV to -14.56 eV the spinors are composed by several components having the same double group symmetry, but arising from different molecular orbitals. This effect prevents from a direct comparison between the SR and the SO schemes, however it is expected to be strong only for high energy transitions, starting from the gold d band which consists of many quasi-degenerate MOs, on the other hand the low energy part of the spectrum does not suffer this problem and the comparison between SR and SO schemes is more informative.

We can summarize the results saying that for the absorption spectrum of W_{Au}_{12} the SO coupling does not alter the nature of the transitions in the low energy spectral region (up to 6 eV), the main effect being a red shift in the lines and an intensity redistribution. For higher energies the nature of the transitions in terms of one electron excited configurations is strongly dependent on the computational scheme (SR or SO), however the convoluted profile shows only minor differences and also the character of the most intense feature in terms of gold interband $p \leftarrow d$ transition remains preserved. Therefore we may say that the inclusion of SO coupling in the calculations is needed to obtain accurate results for the lowest lying excitation, while for higher energy, where the analysis is not practicable at the level of a single discrete line, the simple SR can give an adequate description of the intensity distribution.

5.4.3. MoAu₁₂ electronic structure

MoAu₁₂ and WAu₁₂ are isoelectronic, so it can be reasonably expected that their electronic structure is similar. Therefore we assume that all the discussion already considered in previous section 5.4.1. remains in general valid, and we only point out the attention on the differences between the two clusters. Moreover it must be considered that the geometrical structure of the Au cage is in practice identical in WAu₁₂ and MoAu₁₂, therefore all the differences must be ascribed to the nature of the encapsulated atom. It is convenient to compare the correlation diagram relative to MoAu₁₂ at the SR level (left side of Figure 5.3) with previous Figure 5.1: notice that Mo 5*s* and 4*d* atomic orbitals are destabilized on average by more than 1 eV with respect to W 6*s* and 5*d*, moreover their energetic order is reversed, in Mo 4*d* is the most stable orbital, instead of 6*s* in W. This trend can be ascribed to a consequence of the lanthanide contraction effect: in W the completely filled 4*f*¹⁴ shell is less effective to shield the nuclear charge, as a consequence the tungsten atomic orbitals are stabilized with respect to Mo. Moreover also the inversion of the atomic *s* and *d* orbitals ordering between W and Mo can be ascribed to the poor shielding of the 4*f*¹⁴ shell and therefore stabilizes the 6*s* orbital of W more than 5*d* which is more diffuse due to the centrifugal barrier related to its angular momentum *l*=2.

The consequence of this different ordering of the encaged metal atomic orbitals has only a minor effect on the frontier orbitals of the cluster, in fact the HOMO does not change its energy while MoAu₁₂ LUMO is shifted by -0.15 eV. A more pronounced effect is observed for the molecular orbitals above the LUMO, in fact while in WAu₁₂ 5*t*_{2u} and 6*a*_g are almost degenerate (with eigenvalues -7.92 eV and -7.83 eV respectively) in MoAu₁₂ 5*t*_{2u} and 5*a*_g are separated by 0.52 eV (-7.90 eV and -7.38 eV respectively). Such effect must be attributed to the destabilization of the atomic Mo 5*s* orbital previously discussed.

If the SO coupling is considered (Figure 5.3, right side), we find another interesting difference with respect to WAu₁₂: in the latter the HOMO 7*h*_g splitting to give the 11*i*_g and 8*g*_g spinors is negligible (less than 0.01 eV), while in MoAu₁₂ a splitting of 0.09 eV is calculated. On the other hand the 8*h*_g LUMO splitting of WAu₁₂ (0.45 eV) is reduced to 0.38 eV in MoAu₁₂.

In summary we can conclude saying that the main differences in the electronic structure from WAu₁₂ to MoAu₁₂ are limited to the remove of an accidental quasi degeneracy of the pair of virtual molecular orbitals above the LUMO at the SR level, while the SO coupling introduces further a slight splitting of the HOMO (7*h*_g) which was negligible in WAu₁₂.

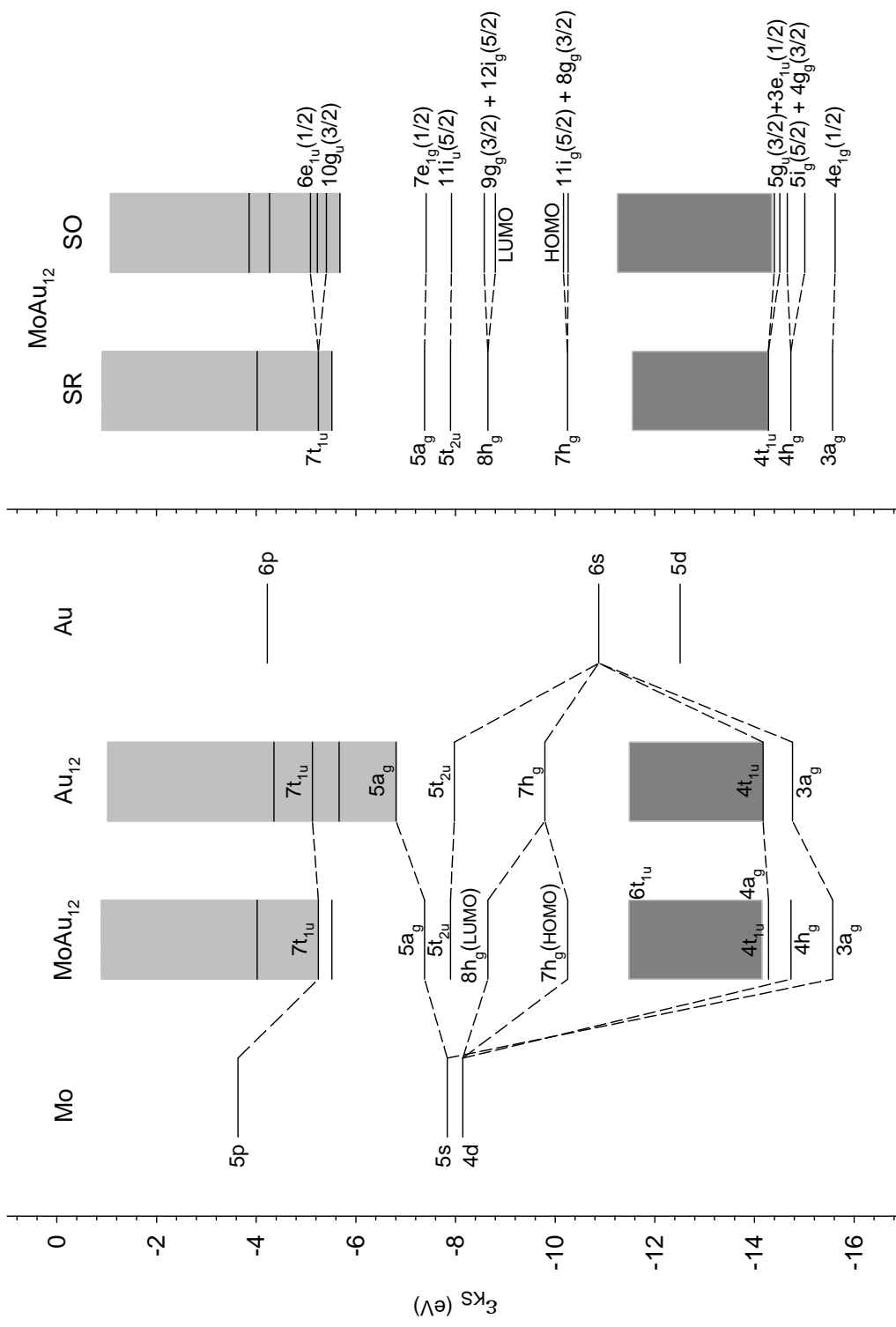


Figure 5.3 Left side: correlation diagram of the molecular orbitals of MoAu₁₂ in terms of Au₁₂ cage and Mo atom, scalar relativistic eigenvalues are reported, orbitals are classified according to I_h point group symmetry. Right side: correlation diagram between the scalar relativistic molecular orbitals and the spin orbit spinors of MoAu₁₂, orbitals and spinors are classified according to I_h and I_h² point group symmetry respectively.

5.4.4. MoAu₁₂ SR and SO TDDFT photoabsorption spectra

The TDDFT excitation spectra of MoAu₁₂, calculated at both SR and SO level, have been reported in Figure 5.4 up to 6 eV of excitation energy, in the small insets they are considered up to 12 eV. A selection of relevant excitations (lines) of the spectra is considered in Table 5.3 at both SR and SO level (reported at the end of the chapter). It is interesting to follow the results trying to identify the evolution of the photoabsorption spectrum when the central atom is changed: the SR results of the low energy spectrum of MoAu₁₂ (Figure 5.4, upper panel) appear quite different with respect to WAu₁₂ (Figure 5.2), the most relevant difference is that the spectrum of MoAu₁₂ is less rich in structures with respect to WAu₁₂.

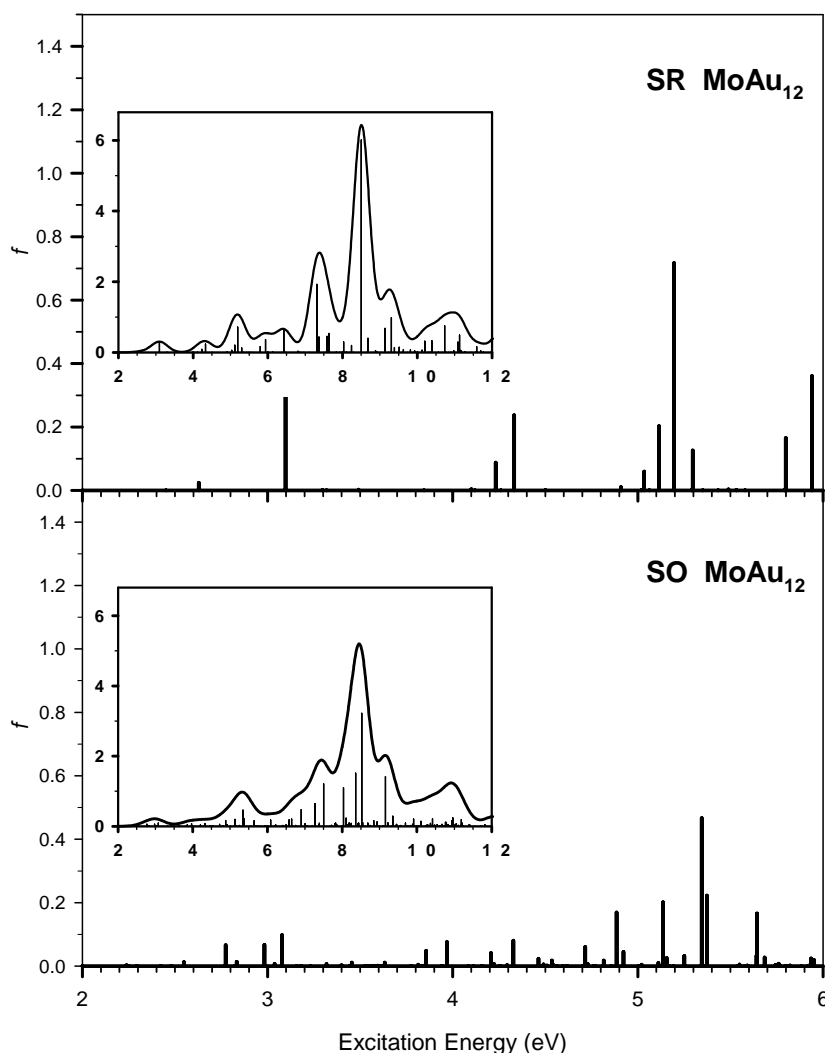


Figure 5.4 Scalar relativistic (SR, upper panel) and spin-orbit (SO, lower panel) TDDFT excitation spectrum of MoAu₁₂, in the low energy region up to 6 eV. The spectra calculated up to 12 eV are reported as insets, together with the convolution of discrete lines with Gauss functions of 0.5 eV FWHM.

In MoAu₁₂ the first relevant excitation is calculated at 3.10 eV (4T_{1u}), followed by two close lines at 4.23 and 4.33 (12 and 14T_{1u}) and then by a group of four lines between 5.03 and 5.30

eV (20, 22, 23 and 25T_{1u}). It is interesting to compare the nature of such intense excitations with those found in WAu₁₂: in fact we find a strong resemblance in terms of excited state composition (compare Table 5.3 with Table 5.2) between 4T_{1u} in both clusters, while 14T_{1u}, 23T_{1u} and 25T_{1u} of MoAu₁₂ correspond to 12T_{1u}, 24T_{1u} and 26T_{1u} of WAu₁₂ respectively. On the other hand in WAu₁₂ there are some intense excitations which loose their intensity going to MoAu₁₂, in particular 2T_{1u}, 9T_{1u} and 18T_{1u}. It is worth noting that the 9T_{1u} and 18T_{1u} excitations in WAu₁₂ are ascribed to transitions in which the final orbitals are 6a_g and 8t_{1u} respectively, (Table 5.2) with high W 6s and 6p contribution, the corresponding transitions in MoAu₁₂ have negligible intensity as a consequence of the different behaviour of Mo 5s and 5p orbitals. Moreover in MoAu₁₂ a pair of intense transitions is calculated at 5.80 eV (32T_{1u}) and 5.94 eV (33T_{1u}), they do not have counterparts with appreciable intensity in WAu₁₂. This is somehow surprising, because their nature is of mainly Au $p \leftarrow d$ and Au $s \leftarrow d$ interband type, therefore should not be strongly affected by the nature of the encapsulated metal.

In summary the comparison of the low energy region of the spectrum at SR level between WAu₁₂ and MoAu₁₂ suggests that the transitions involving the virtual orbitals belonging to the encapsulated metal are intense in WAu₁₂ and negligible in MoAu₁₂.

Now let's consider the effect of the SO coupling on the TDDFT low energy spectrum in the lower box of Figure 5.4: the result consists in many lines with comparable weak intensity, a very different picture with respect to WAu₁₂, where at least the first four SR lines do not split if the SO coupling is switched on. The nature of the calculated SO excitations is reported in Table 5.3, and by the inspection of the occupied and empty spinors involved in the leading excited configurations, we may try to identify which SR excitations are contained in the SO ones, such analysis allows to identify three groups of excitations in the SO spectrum as follows. The first group consists in the three SO transitions 10, 13 and 17T_{1u} which can be associated to the splitting of the SR 4T_{1u} line, the second group of SO excitations 43, 45, 50 and 56T_{1u} is assigned to the splitting of the SR pair 12 and 14T_{1u} and finally the third group consists of six SO transitions 71, 77, 86, 92, 94 and 105 T_{1u} which contain various amounts of contributions from the SR 20, 22, 23 and 25T_{1u} excitations.

The absorption spectrum up to 12 eV is considered in the two insets of Figure 5.4 at both SR and SO level: the high density of discrete lines prevents a detailed analysis, however the intensity distribution can be easily described following the convolution profile. As already noticed in WAu₁₂, for energy higher than 6 eV the SR description is generally adequate, since SO coupling changes dramatically the individual lines but do not affect the salient features present in the convoluted profile. As a general observation the convoluted SO profile appears

smoother than the SR one, as an effect of the line splitting, which in any case remain very similar to WAu_{12} .

5.5. CONCLUSIONS

In this work we have studied the photoabsorption spectrum of both WAu_{12} and MoAu_{12} , employing the TDDFT formalism at both SR and SO level to identify the role of spin-orbit coupling on the spectrum. While above roughly 6 eV of excitation energy the SO coupling does not affect the general intensity distribution, for lower energy it plays an important role to reassess the energy position and the intensity for the low lying excitations. In particular in WAu_{12} the lowest SR excitations are not split when SO is included, but shifted in energy with a concomitant intensity redistribution.

The comparison at the SR level between WAu_{12} and MoAu_{12} show that in the latter some lines are suppressed with respect to the former, as an effect of the different role played by the atomic *s* and *d* functions of the engaged atom on the virtual molecular orbital. On the other hand in MoAu_{12} the lowest SR lines are dramatically split in many contributions when the SO coupling is considered.

In summary we conclude that for an accurate theoretical description of the photoabsorption process in such systems, the inclusion of spin-orbit coupling is mandatory in the low energy region, where the discrete excitations are still well separated each other and can be properly characterized in terms of specific one-electron excitations between orbitals or spinors at the SR or SO level of theory respectively. On the other hand at higher energy, where the discrete lines becomes much denser, the analysis of each line in terms of one electron excited configurations becomes soon impractical and the convoluted intensity can be properly described already at the scalar relativistic level.

5.5.1. Acknowledgements

This work has been supported by grants from MIUR (Programmi di Ricerca di Interesse Nazionale PRIN 2006) of Italy and by INSTM (Progetto PRISMA 2004).

Table 5.2

Scalar Relativistic			
Excitation	E_{exc} (eV)	f	excited state composition (main configuration contributions)
2 T_{1u}	2.69	0.078	$7h_g$ (Au: 6s 31% 6p 15% 5d 29%, W: 5d 23%) \rightarrow $5t_{2u}$ (Au: 6s 78% 6p 14%)
4 T_{1u}	3.23	0.205	$7t_{1u}$ (Au: 6s 40% 5d 50%) \rightarrow $8h_g$ (Au: 6s 31% 6p 16%, W: 5d 47%)
9 T_{1u}	3.81	0.173	$7t_{1u}$ (Au: 6s 40% 5d 50%) \rightarrow $6a_g$ (Au: 6s 29% 6p 49%, W: 6s 20%)
12 T_{1u}	4.39	0.094	57% $4t_{2u}$ (Au: 5d) \rightarrow $8h_g$ (Au: 6s 31% 6p 16%, W: 5d 47%) 31% $2h_u$ (Au: 5d) \rightarrow $8h_g$ (Au: 6s 31% 6p 16%, W: 5d 47%)
18 T_{1u}	4.87	0.191	$7h_g$ (Au: 6s 31% 6p 15% 5d 29%, W: 5d 23%) \rightarrow $8t_{1u}$ (Au: 6s 24% 6p 55%, W: 6p 20%)
22 T_{1u}	5.14	0.027	$6t_{1u}$ (Au: 5d) \rightarrow $8h_g$ (Au: 6s 31% 6p 16%, W: 5d 47%)
24 T_{1u}	5.27	1.126	$7h_g$ (Au: 6s 31% 6p 15% 5d 29%, W: 5d 23%) \rightarrow $4g_u$ (Au: 6p 84% 5d 15%)
26 T_{1u}	5.47	0.037	$3t_{2u}$ (Au: 5d) \rightarrow $8h_g$ (Au: 6s 31% 6p 16%, W: 5d 47%)
45 T_{1u}	7.35	1.091	35% $6h_g$ (Au: 5d) \rightarrow $8t_{1u}$ (Au: 6s 24% 6p 55%, W: 6p 20%) 24% $6h_g$ (Au: 5d) \rightarrow $4g_u$ (Au: 6p 84% 5d 15%)
48 T_{1u}	7.45	1.601	$6h_g$ (Au: 5d) \rightarrow $8t_{1u}$ (Au: 6s 24% 6p 55%, W: 6p 20%)
50 T_{1u}	7.68	0.704	$7t_{1u}$ (Au: 6s 40% 5d 50%) \rightarrow $9h_g$ (Au: 6p 50% 5d 17%, W: 5d 23%)
63 T_{1u}	8.56	6.014	30% $3h_u$ (Au: 5d) \rightarrow $9h_g$ (Au: 6p 50% 5d 17%, W: 5d 23%) 21% $3g_u$ (Au: 5d) \rightarrow $9h_g$ (Au: 6p 50% 5d 17%, W: 5d 23%)
Spin Orbit			
Excitation	E_{exc} (eV)	f	excited state composition (main configuration contributions)
8 T_{1u}	2.62	0.076	41% $11i_g$ (5/2) ($7h_g$) \rightarrow $11i_u$ (5/2) ($5t_{2u}$) 33% $8g_g$ (3/2) ($7h_g$) \rightarrow $11i_u$ (5/2) ($5t_{2u}$)
13 T_{1u}	3.10	0.137	45% $10g_u$ (3/2) ($7t_{1u}$) \rightarrow $12i_g$ (5/2) ($8h_g$) 35% $6e_{1u}$ (1/2) ($7t_{1u}$) \rightarrow $9g_g$ (3/2) ($8h_g$)
24 T_{1u}	3.50	0.102	$10g_u$ (3/2) ($7t_{1u}$) \rightarrow $8e_{1g}$ (1/2) ($6a_g$)
77 T_{1u}	4.77	0.339	49% $8g_g$ (3/2) ($7h_g$) \rightarrow $7e_{1u}$ (1/2) ($8t_{1u}$) 35% $11i_g$ (5/2) ($7h_g$) \rightarrow $11g_u$ (3/2) ($8t_{1u}$)
90 T_{1u}	5.38	0.713	$11i_g$ (5/2) ($7h_g$) \rightarrow $4e_{2u}$ (7/2) ($4g_u$)
92 T_{1u}	5.41	0.172	$6i_u$ (5/2) ($3t_{2u}$) \rightarrow $9g_g$ (3/2) ($8h_g$)
226 T_{1u}	8.50	1.768	$6i_g$ (5/2) (75% $2g_g$ + 18% $5h_g$) \rightarrow $11g_u$ (3/2) ($8t_{1u}$)
232 T_{1u}	8.57	2.568	29% $7i_u$ (5/2) (56% $4t_{2u}$ + 26% $2h_u$ + 13% $2g_u$) \rightarrow $13i_g$ (5/2) ($9h_g$) 25% $6i_g$ (5/2) (75% $2g_g$ + 18% $5h_g$) \rightarrow $11g_u$ (3/2) ($8t_{1u}$)

Table 5.2 T_{1u} valence scalar relativistic and spin-orbit excitation spectrum of $W\text{Au}_{12}$. Excitation energy (E_{exc}), oscillator strength (f) and excited state composition in terms of monoexcited configurations are reported.

Table 5.3

Scalar Relativistic			
Excitation	E_{exc} (eV)	f	excited state composition (main configuration contributions)
4 T_{1u}	3.10	0.301	68% $6t_{1u}$ (Au: 6s 44% 5d 48%) \rightarrow $8h_g$ (Au: 6s 34% 6p 15%, Mo: 4d 45%) 21% $7h_g$ (Au: 6s 27% 6p 14% 5d 29%, Mo: 4d 28%) \rightarrow $5t_{2u}$ (Au: 6s 78% 6p 14%)
12 T_{1u}	4.23	0.088	$2h_u$ (Au: 5d) \rightarrow $8h_g$ (Au: 6s 34% 6p 15%, Mo: 4d 45%)
14 T_{1u}	4.33	0.237	28% $4t_{2u}$ (Au: 5d) \rightarrow $8h_g$ (Au: 6s 34% 6p 15%, Mo: 4d 45%) 27% $2h_u$ (Au: 5d) \rightarrow $8h_g$ (Au: 6s 34% 6p 15%, Mo: 4d 45%) 25% $6t_{1u}$ (Au: 6s 44% 5d 48%) \rightarrow $5a_g$ (Au: 6p 53%, Mo: 5s 47%)
20 T_{1u}	5.03	0.059	$6h_g$ (Au: 5d) \rightarrow $5t_{2u}$ (Au: 6s 78% 6p 14%)
22 T_{1u}	5.11	0.203	$7h_g$ (Au: 6s 27% 6p 14% 5d 29%, Mo: 4d 28%) \rightarrow $7t_{1u}$ (Au: 6s 24% 6p 64%, Mo: 5p 14%)
23 T_{1u}	5.20	0.717	$7h_g$ (Au: 6s 27% 6p 14% 5d 29%, Mo: 4d 28%) \rightarrow $4g_u$ (Au: 6p 85% 5d 13%)
25 T_{1u}	5.30	0.126	$3t_{2u}$ (Au: 5d) \rightarrow $8h_g$ (Au: 6s 34% 6p 15%, Mo: 4d 45%)
32 T_{1u}	5.80	0.165	70% $2g_g$ (Au: 5d) \rightarrow $5t_{2u}$ (Au: 6s 78% 6p 14%) 25% $4t_{1u}$ (Au: 6s 49% 5d 51%) \rightarrow $8h_g$ (Au: 6s 34% 6p 15%, Mo: 4d 45%)
33 T_{1u}	5.94	0.361	46% $1t_{2g}$ (Au: 5d) \rightarrow $4g_u$ (Au: 6p 85% 5d 13%) 22% $4t_{1u}$ (Au: 6s 49% 5d 51%) \rightarrow $8h_g$ (Au: 6s 34% 6p 15%, Mo: 4d 45%)
Spin Orbit			
Excitation	E_{exc} (eV)	f	excited state composition (main configuration contributions)
10 T_{1u}	2.77	0.066	43% $9g_u$ (3/2) ($6t_{1u}$) \rightarrow $12i_g$ (5/2) ($8h_g$) 23% $10i_u$ (5/2) ($61\% 3g_u + 30\% 3h_u$) \rightarrow $9g_g$ (3/2) ($8h_g$)
13 T_{1u}	2.98	0.067	50% $5e_{1u}$ (1/2) ($6t_{1u}$) \rightarrow $9g_g$ (3/2) ($8h_g$) 35% $10i_u$ (5/2) ($61\% 3g_u + 30\% 3h_u$) \rightarrow $12i_g$ (5/2) ($8h_g$)
17 T_{1u}	3.08	0.098	$10i_u$ (5/2) ($61\% 3g_u + 30\% 3h_u$) \rightarrow $12i_g$ (5/2) ($8h_g$)
43 T_{1u}	3.86	0.049	63% $9g_u$ (3/2) ($6t_{1u}$) \rightarrow $7e_{1g}$ (1/2) ($5a_g$) 22% $7i_u$ (5/2) ($53\% 4t_{2u} + 29\% 2h_u + 13\% 2g_u$) \rightarrow $9g_g$ (3/2) ($8h_g$)
45 T_{1u}	3.97	0.076	46% $7i_u$ (5/2) ($53\% 4t_{2u} + 29\% 2h_u + 13\% 2g_u$) \rightarrow $9g_g$ (3/2) ($8h_g$) 21% $7i_u$ (5/2) ($53\% 4t_{2u} + 29\% 2h_u + 13\% 2g_u$) \rightarrow $12i_g$ (5/2) ($8h_g$)
50 T_{1u}	4.21	0.041	$7i_u$ (5/2) ($53\% 4t_{2u} + 29\% 2h_u + 13\% 2g_u$) \rightarrow $12i_g$ (5/2) ($8h_g$)
56 T_{1u}	4.33	0.080	$5e_{1u}$ (1/2) ($6t_{1u}$) \rightarrow $7e_{1g}$ (1/2) ($5a_g$)
71 T_{1u}	4.72	0.060	50% $7g_u$ (3/2) ($46\% 5t_{1u} + 39\% 2h_u$) \rightarrow $12i_g$ (5/2) ($8h_g$) 21% $11i_g$ (5/2) ($7h_g$) \rightarrow $12i_u$ (5/2) ($4g_u$)
77 T_{1u}	4.89	0.169	$11i_g$ (5/2) ($7h_g$) \rightarrow $10g_u$ (3/2) ($7t_{1u}$)
86 T_{1u}	5.14	0.201	50% $7i_g$ (5/2) ($75\% 5h_g + 21\% 2g_g$) \rightarrow $11i_u$ (5/2) ($5t_{2u}$) 33% $8g_g$ (3/2) ($7h_g$) \rightarrow $6e_{1u}$ (1/2) ($7t_{1u}$)
92 T_{1u}	5.35	0.466	$6i_u$ (5/2) ($3t_{2u}$) \rightarrow $9g_g$ (3/2) ($8h_g$)
94 T_{1u}	5.37	0.223	$6i_u$ (5/2) ($3t_{2u}$) \rightarrow $9g_g$ (3/2) ($8h_g$)
105 T_{1u}	5.64	0.166	$3e_{1u}$ (1/2) ($75\% 4t_{1u} + 24\% 5t_{1u}$) \rightarrow $9g_g$ (3/2) ($8h_g$)

Table 5.3 T_{1u} valence scalar relativistic and spin-orbit excitation spectrum of MoAu₁₂. Excitation energy (E_{exc}), oscillator strength (f) and excited state composition in terms of monoexcited configurations are reported.

6. THEORETICAL STUDY ON THE PHOTOABSORPTION OF MAu_{12}^- ($M = \text{V, Nb, Ta}$)

Stener, M.; Nardelli, A.; Fronzoni, G., *Chem. Phys. Lett.* **2008**, *462*, 358–364.

The valence photoabsorption spectra of the series of the monoanionic closed shell icosahedral clusters MAu_{12}^- with $M = \text{V, Nb}$ and Ta have been calculated with the Time Dependent Density Functional Theory (TDDFT), employing the Zero Order Regular Approximation (ZORA) at both scalar relativistic and spin orbit coupling levels. The calculated photoabsorption spectra show interesting variations according to the nature of the encapsulated metal atom. Spin-orbit coupling plays an important role in these systems. The comparison with the neutral isoelectronic clusters WAu_{12} and MoAu_{12} suggests a curious relationship along the diagonal of the periodic table.

6.1. INTRODUCTION

The chemistry of gold is extremely rich and various, so that many experimental^{6.1} and theoretical^{6.2} aspects have been addressed and rationalized. Among many others, one of the most striking gold characteristic is its propensity to surround main-group atoms to form cage-like structure,^{6.3} like, for example, in the octahedral cluster $[(\text{LAu})_6\text{C}]^{2+}$,^{6.4,6.5} and in the protected cluster $[\text{Au}_{13}(\text{SCH}_3)_8]^{3+}$.^{6.6} A classical example of theory prediction is represented by the work of Pyykkö and Runeberg:^{6.7} they were able to predict the existence of the bimetallic cluster WAu_{12} before its laboratory production and characterization.^{6.8} WAu_{12} and its isoelectronic omologue MoAu_{12} have been characterized by mass spectrometry and photodetachment of their monoanions, and revealed almost identical spectral patterns. The exceptional stability of such systems has been attributed to the strong relativistic effects typical of gold,^{6.2} to the aurophilic attraction and, most important, to the 18 electrons closed shell electronic structure induced by the icosahedral symmetry of the gold cage surrounding the encapsulated metal atom. Soon after their discovery, the isoelectronic negative series

VAu_{12}^- , NbAu_{12}^- and TaAu_{12}^- have been produced and characterized as well,^{6,9} showing again very similar photoelectron spectra.

Recently we have performed a theoretical study on the photoabsorption of WAu_{12} and MoAu_{12} at the TDDFT level, including relativistic effects at both scalar and spin-orbit level;^{6,10} somehow surprisingly the photoabsorption spectra have proven to be much more sensitive to the nature of the encaged atom than photodetachment measurements, as a result of the complex role of spin-orbit coupling with electron excitations. Therefore we considered interesting to study in the present work valence photoabsorption of the isoelectronic negative series VAu_{12}^- , NbAu_{12}^- and TaAu_{12}^- , in order to identify possible trends and compare the results with previous neutral clusters.

These negative systems may be even more interesting than neutral ones because are potential building blocks for bulk nanomaterials, since the negative charge should prevent their alloy fusion, provided proper counterions are included in the system.^{6,9}

6.2. COMPUTATIONAL MODEL

All calculations have been performed with the ADF code,^{6,11} which employs the relativistic two-components Zeroth-Order Regular Approximation (ZORA) at both Scalar Relativistic (SR) and Spin Orbit (SO) levels, and Time-Dependent Density Functional Theory (TDDFT). Such schemes includes all the most relevant physics involved in the photoabsorption process, namely the one-electron configuration mixing of TDDFT and the SO coupling. Details of the relativistic two-components ZORA-TDDFT method can be found in the literature.^{6,11} The method furnishes the excitation energies, the intensities of the transitions for closed shell molecules as well as an analysis of the excited states in terms of singly excited configurations.^{6,12}

It is worth mentioning that one of the most salient optical spectral features of noble metal nanoparticles is the surface plasmon resonance, which stems from collective electron excitations and falls in the energy range considered in the present work.^{6,13} Such collective electron excitations can be properly described at the TDDFT level, in fact the TDDFT equations are obtained from linear response theory in order to describe free (collective) oscillations of electron density.^{6,12} A successful application of the TDDFT to plasmons of silver nanoclusters has been recently demonstrated by Schatz et al..^{6,14} The surface plasmon

band, however, starts to gain intensity in nanocluster with size larger than 2 nm (that is with more than roughly 100 atoms), so we expect that the surface plasmon resonance does not play any appreciable role in the present systems.

Basis sets consisting of Slater Type Orbitals (STO) have been employed, of triple-zeta plus polarization (TZP) size for valence, while core electrons have been kept frozen up to $4f$ for Au and Ta, up to $4p$ for Nb and up to $3p$ for V.

The geometries of the clusters have been optimized at the SR ZORA level employing the PW91^{6.15,6.16} exchange correlation energy functional and have been kept constrained to the I_h symmetry: the following optimised Au-Au bond lengths have been obtained: 2.878 Å, 2.923 Å, 2.919 Å for $M = V, Nb, Ta$ respectively. Since ADF does not support the complete I_h point group symmetry, the calculations have been performed within the D_{5d} subgroup, but the labels of the Irreducible Representations (IR) of the I_h point group and of the I_h^2 double group^{6.17} have been employed to classify orbitals and spinors for SR and SO calculations respectively. The most relevant effect of the SO coupling is the reduction of degeneracy going from the molecular orbitals to the spinors, the splitting takes place according to Table 1 in Ref. 6.10.

In the TDDFT calculations of the valence excitation spectra the LB94 exchange-correlation potential^{6.18} has been employed, since its correct coulombic asymptotic behaviour has proven crucial for an accurate description of virtual orbitals involved in the valence electron excitations.^{6.19}

6.3. RESULTS AND DISCUSSION

6.3.1. Electronic Structure

The electronic structures of the clusters, in terms of Kohn-Sham (KS) eigenvalues and at both SR and SO levels, are reported in Figure 6.1. We did not report all the levels belonging to the occupied Au 5d band, which is shown as a dark grey area, similarly a thin grey area shows the energy region of the virtual Au 6p band. For all the systems, the $7h_g$ molecular orbital [split in $11i_g(5/2) + 8g_g(3/2)$ spinors in presence of SO coupling] is the Highest Occupied Molecular Orbital (HOMO) and is responsible of most of the chemical bond between the encapsulated metal atom and the gold cage. In fact, as already pointed out in previous works^{6.7,6.10} it is

convenient to consider the formation of the present clusters as the inclusion of the metal atom in the center of the icosahedral Au_{12} cage. The HOMO of a icosahedral Au_{12} cage consists of a h_g molecular orbital partially filled by four electrons, therefore it interacts with the atomic d orbitals of the central atom which belongs to the same h_g IR of the I_h point group: if the atomic d orbitals contain six electrons a stable close shell h_g^{10} electron configuration is obtained. Such situation happens for W and Mo in the neutral clusters, but also for V, Nb and Ta when the cluster carries an extra single negative charge.

The occupied levels show only modest differences along the series, for example the HOMO ($7h_g$) is lowered by only 0.16 eV passing from VAu_{12}^- to NbAu_{12}^- , in good agreement with the corresponding difference of 0.09 eV between the photodetachment HOMO peaks.

The virtual orbitals show instead more pronounced energy variations along the series: in fact, at the SR level, in VAu_{12}^- there are three levels ($8h_g$, $5t_{2u}$ and $5a_g$) separated by 0.91 eV and 0.37 eV respectively, such separations changes to 0.28 eV and 0.53 eV in NbAu_{12}^- and to 0.07 eV and 0.15 eV in TaAu_{12}^- respectively. It is worth noting that it is this high sensitivity of the virtual orbitals energies to the nature of the encaged metal which introduces strong variations in the photoabsorption spectra along the series, much more than in photoionization spectra which depend essentially only on the occupied orbitals energies. Also the HOMO-LUMO gap increases regularly along the series, from 1.25 eV in VAu_{12}^- up to 1.82 eV in NbAu_{12}^- and 2.02 eV in TaAu_{12}^- .

The spin-orbit coupling effect can be easily identified by comparison between the SR and the SO calculation: the main change consists in a splitting of some of the levels, according to the resolution of the IR of the I_h group in those of the double I_h^2 group.^{6,10} From figure 6.1 we observe that the SO splitting for the HOMO is negligible, at most 0.05 eV in NbAu_{12}^- , while the Au $5d$ band is widened by about 0.4 eV in the three clusters. It is interesting to consider the effect of the SO on the LUMO ($8h_g$): this orbital is split by 0.13 eV, 0.12 eV and 0.34 eV for $M = \text{V, Nb and Ta}$ respectively. Such behaviours (small HOMO SO splitting and large LUMO SO splitting for the heaviest metal) have been already observed in our previous study on WAu_{12} and MoAu_{12} .^{6,10} Moreover, in TaAu_{12}^- the virtual levels are so close each other that the higher SO component $12i_g(5/2)$ from $8h_g$ orbital is even able to insert between the immediately successive lying spinors, changing the order of the spinors with respect the SR orbitals.

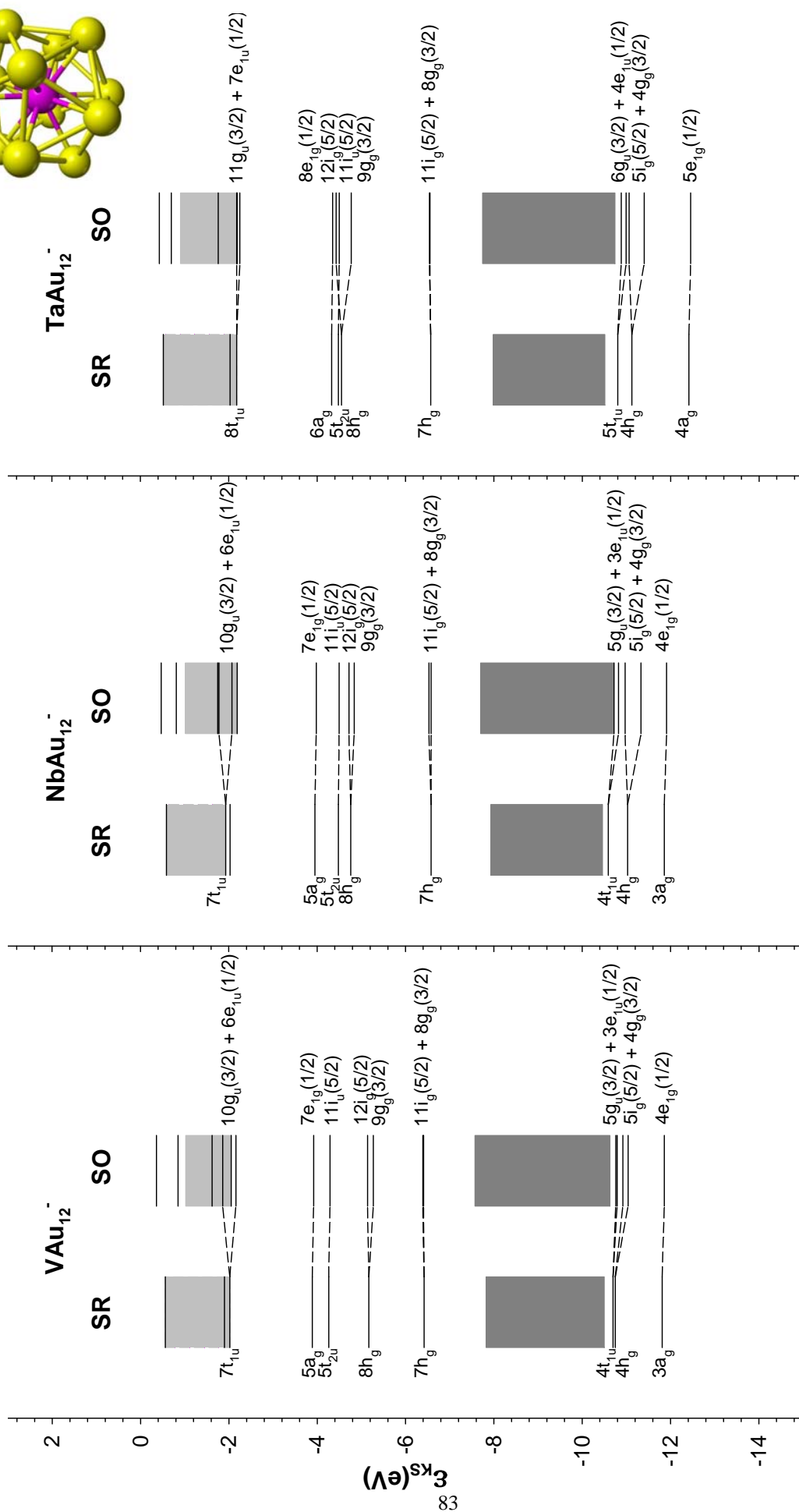
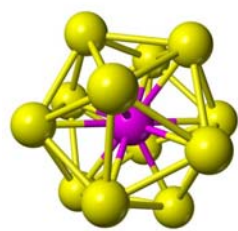


Figure 6.1 Energy levels (in terms of KS eigenvalues) relative to the three clusters VAu_{12}^- , $NbAu_{12}^-$ and $TaAu_{12}^-$. Scalar relativistic (SR) molecular orbitals and spin-orbit (SO) spinors are reported and classified according to I_h and I_h^2 point group symmetry respectively. The icosahedral geometry of the clusters is sketched at the figure top.

6.3.2. Photoabsorption Spectra

The photoabsorption spectra of the three clusters, calculated at both SR and SO levels, have been reported in Figure 6.2; the discrete lines furnished by the TDDFT calculations have been broadened with a gaussian function with FWHM = 0.2 eV to have an easier feeling of the intensity distribution. The energy position, absolute intensity and excited state composition of only the most relevant lines have been reported in Tables 6.1 – 6.3 (reported at the end of the chapter). It is more convenient, to discuss the calculated photoabsorption spectra, to start with the heaviest term TaAu_{12}^- and then passing to the other ones, in order to compare present results with the previous study on WAu_{12} and MoAu_{12} .^{6,10}

In the following we will employ two different notations to denote electron transitions. A specific component of an electron transition consisting of a one-electron excited configuration from an occupied molecular orbital to a virtual one is indicated as $\varphi_{occ} \rightarrow \varphi_{virt}$ (right arrow). Instead the character of an electron transition in terms of atomic components is designated with a left arrow, like for example in the intraband Au $s \leftarrow s$ transition, as it is customary in solid state physics.

The SR results for TaAu_{12}^- are considered in the upper left panel of Figure 6.2: four well resolved structures can be identified, the nature of the involved transitions can be found in Table 6.1. The first peak at 2.60 eV ($2T_{1u}$ transition) has a main intraband Au $s \leftarrow s$ character: more precisely the excitation arises from the HOMO whose Au $6s$ leading contribution (38%) is mixed with Au $5d$ (26%) as a result of the relativistic effects which favour $s-d$ gold hybridization, also Ta $5d$ contributes to the HOMO (20%) due to the presence of the metal-cage chemical bond. The second structure consists of two close transitions: the rather weak $3T_{1u}$ is attributed to Ta $5d \leftarrow \text{Au } 5d$ charge transfer from the cage to the metal, while $6T_{1u}$ consists in a mainly interband $p \leftarrow d$ belonging to the gold cage. The next structure is found at 4.53 eV ($13T_{1u}$) whose character is mainly interband $p \leftarrow s$ within the gold cage. Next we find the most intense spectral feature (between 5 and 6 eV), which is contributed by many lines, the most intense is the $22T_{1u}$ at 5.19 eV, whose nature is strongly mixed between gold interband $s \leftarrow d$ and $p \leftarrow s$. All the next lines ($23, 25$ and $28 T_{1u}$) corresponds to transitions arising from the Au $5d$ band going to Ta $5d$ or Au $6s$.

It is worth mentioning that the experimental vertical photodetachment energies of the present clusters^{6,9} range between 3.8 and 3.9 eV, so the photoabsorption process above these energies produces excited states which are actually coupled with a free electron in the continuum in the

potential field of a neutral cluster. This coupling is neglected in the present formalism and therefore it is important to consider the possible effects of such coupling on the calculated spectra.

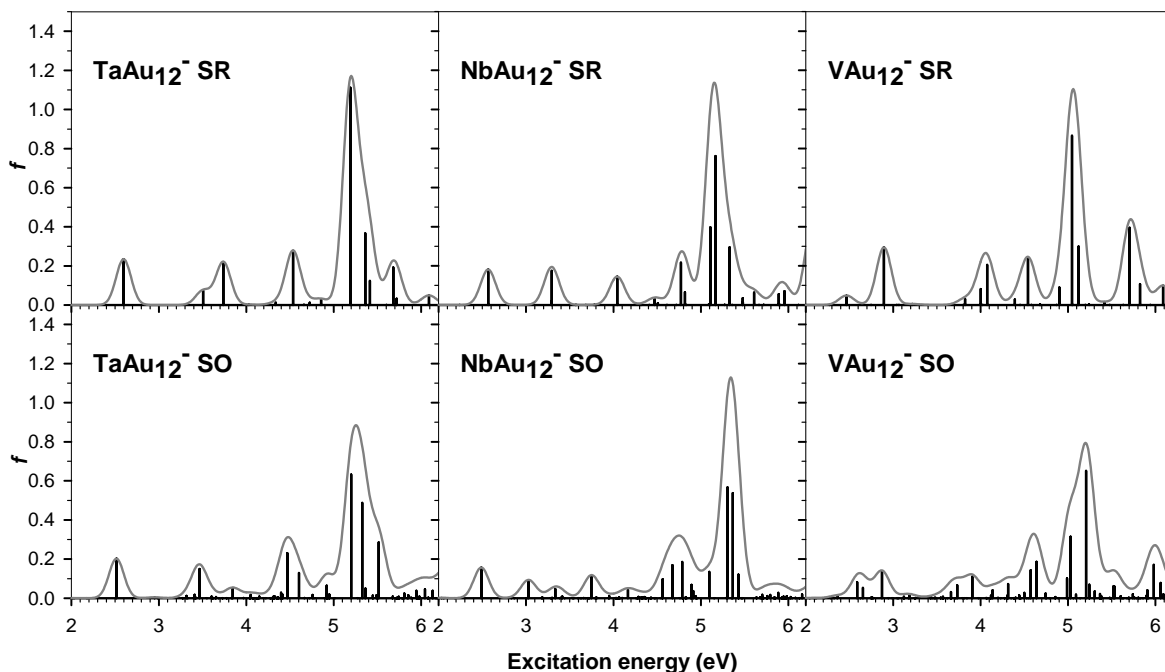


Figure 6.2 Scalar relativistic (SR, upper panels) and spin-orbit (SO, lower panels) TDDFT excitation spectrum of TaAu_{12}^- , NbAu_{12}^- and VAu_{12}^- . The discrete lines have been convoluted with Gauss functions of 0.2 eV FWHM.

Usually continuum cross sections are smooth functions of the photon energy, at least we do not expect large variations on the scale of few eVs as considered in the present work. Therefore we expect that above 4 eV a smooth background due to the photoelectron continuum spectrum should be added to the present calculated spectra for a better comparison with the experiment. By the way, other interesting effects typical of the electron continuum, like for example shape resonances characteristic of cage molecules, may be observed in experiments at higher photon energy, namely several tens of eV above the photodetachment threshold and may be described with a proper continuum TDDFT formalism.^{6,20}

Now let us consider what happens when the SO coupling is switched on the TaAu_{12}^- cluster (lower left panel of Figure 6.2 and Table 6.1): the first structure (now at 2.62 eV) does not change appreciably its energy position with respect to the SR case, only a slight intensity decrease (-14%) is observed and it retains its main intraband Au $s \leftarrow s$ character. Then at 3.47 eV the SO $17T_{1u}$ transition is found, which is contributed by roughly equal amounts of SR 3 and 6 T_{1u} , the overall effect is a slight red shift of this peak (by less than 0.3 eV) with respect to the SR one. The SO $32T_{1u}$ transition has the same nature of the SR $6T_{1u}$ one, but the intensity

is strongly reduced. The next feature in the SO spectrum consists of two close transitions, quite interestingly the first line (70 T_{1u} in the SO spectrum) corresponds to the SR 13 T_{1u} , which is almost unaffected by the SO coupling as concerns both energy position and intensity, while the second one (72 T_{1u} in the SO spectrum) is contributed by 52% from $7h_g \rightarrow 4g_u$ one-electron excited configuration. This finding shows that the role of the SO coupling on the photoabsorption spectrum can be very different on the various lines, in some cases it can be negligible, in other cases it can remix the configurations which contribute the excitation giving strong energy shift and intensity redistribution. Finally the SO spectrum in the range 5.20 - 5.52 eV carries three lines whose compositions is largely similar to that found for the SR 23, 25 and 28 T_{1u} , slightly shifted at lower energy (by about 0.2 eV) and roughly doubled in intensity.

The $NbAu_{12}^-$ SR results are considered in the upper central panel of Figure 6.2 and Table 6.2: the spectrum is characterized by four well separated lines (2, 4, 10 and 18 T_{1u}) at 2.57, 3.29, 4.04 and 4.77 eV respectively, each of them with comparable intensity. A comparison of their excited state compositions with those of the Ta cluster (tables 6.2 and 6.1), shows that they are the exact counterparts of the 2, 3, 6 and 13 T_{1u} transitions in $TaAu_{12}^-$, however while 3 and 6 T_{1u} in $TaAu_{12}^-$ are very close in energy (0.23 eV), 4 and 10 T_{1u} in $NbAu_{12}^-$ are well separated by even 0.75 eV. This is a consequence of the different energy separation of the final virtual orbitals involved in such transitions: in fact the $5a_g$ and the $8h_g$ unoccupied molecular orbitals in $NbAu_{12}^-$ are separated by 0.81 eV while $6a_g$ and the $8h_g$ molecular orbitals in $TaAu_{12}^-$ by only 0.22 eV, and this characteristic of the electronic structure is well reflected in the calculated spectrum. Finally the three strongest lines above 5 eV show also pronounced resemblance with those of $TaAu_{12}^-$ in the same energy region. Now let us consider the SO spectrum of $NbAu_{12}^-$ in the lower central panel of Figure 6.2: the first peak at 2.49 eV corresponds to the SR 2 T_{1u} transition, while the next two peaks at 3.03 and 3.34 eV are the results of the spin-orbit splitting of the SR 4 T_{1u} transition. The next feature in the SO spectrum (33 T_{1u} at 3.75 eV) has the same nature of the SR 10 T_{1u} , therefore in this case the SO coupling shifts the peak by 0.29 eV to lower energy. At 4.17 eV we find a weak feature (SO 50 T_{1u}) which is another component of the SR 10 T_{1u} split by the SO coupling. Starting at 4.56 eV and at higher energy seven lines with moderate intensity are calculated at the SO level, they are dominated by only one excited configuration, however the involved spinors have contributions from different molecular orbitals so it is not easy to assess a clear derivation

from the SR lines. In this energy range we may qualitatively say that the SO transitions are mainly contributed by the SR ones, but with strong remixing already at the orbital - spinor level so the individual character is collectively lost.

The SR spectrum of the VAu_{12}^- cluster is considered in the right upper panel of Figure 6.2 and in Table 6.3: a weak transition at 2.47 eV ($2T_{1u}$) is followed by another one, six times more intense, at 2.89 eV ($4T_{1u}$). The nature of this transitions pair is the same as already found in NbAu_{12}^- ($2T_{1u}$ and $4T_{1u}$) as well as in TaAu_{12}^- ($2T_{1u}$ and $3T_{1u}$), in fact the lower transition consists in a $s \leftarrow \text{HOMO}$ excitation and the second one has mainly $\text{LUMO} \leftarrow \text{Au } 5d$ character. However, two important differences are now observed with respect to the previous two clusters: first the transitions are now much closer in energy (0.4 eV with respect to 0.7 and 0.9 eV), second the excitations are actually contributed by both excited configurations so their nature is strongly mixed, at variance with the corresponding excitations in the other clusters which are properly described by a single excited configuration. The next spectral features, essentially contributed by $14T_{1u}$ at 4.08 eV and $17T_{1u}$ at 4.54 eV, are assigned to $\text{Au } 6p \leftarrow \text{Au } 5d$ interband and $\text{Au } 6p \leftarrow \text{HOMO}$ transitions respectively, analogue transitions were found in the other two clusters in the same energy range. The most intense transition $23T_{1u}$ is contributed for 49% by a $\text{Au } p \leftarrow \text{HOMO}$ excitation, which is present in the most intense excitation of the other two clusters as well, but in the latter its contribution is at most 30%. In the previous two clusters this most intense peak was followed by only weak lines, but in VAu_{12}^- a rather intense line is found at 5.71 eV ($32T_{1u}$), its nature can be classified as charge transfer $\text{V } 3d \leftarrow \text{Au } 5d$.

Finally, let us consider the effect of the SO coupling on the spectrum of the VAu_{12}^- cluster (right lower panel of Figure 6.2 and Table 6.3): in this case the effect of the SO coupling is much more violent with respect to the other clusters, in fact the intensity is redistributed over many weak lines in a wide energy range. The lines below 3 eV keep to some extent the nature of the SR $2T_{1u}$ and $4T_{1u}$ ones, but the SO transition at 2.65 eV has not a SR counterpart with appreciable intensity. Then the SO transition at 3.91 eV has only a partial contribution in common with the $12T_{1u}$ and $14T_{1u}$ SR excitations, while the SO transition at 4.64 eV is the only partial counterpart of the most intense SR $23T_{1u}$, which is therefore shifted by even 0.41 eV as an effect of the SO coupling. The most intense SO spectral feature just above 5 eV is contributed by two lines (at 5.03 and 5.21 eV), whose nature can be related to the SR $32T_{1u}$ excitation located at 5.71 eV, also in this case strongly red-shifted by the SO coupling.

6.3.3. Comparison with isoelectronic clusters WAu_{12} and MoAu_{12}

It is interesting to compare the calculated spectra of NbAu_{12}^- and VAu_{12}^- with those of the isoelectronic clusters WAu_{12} and MoAu_{12} considered in the previous work^{6,10} and reported on Figure 6.3 at the SR level.

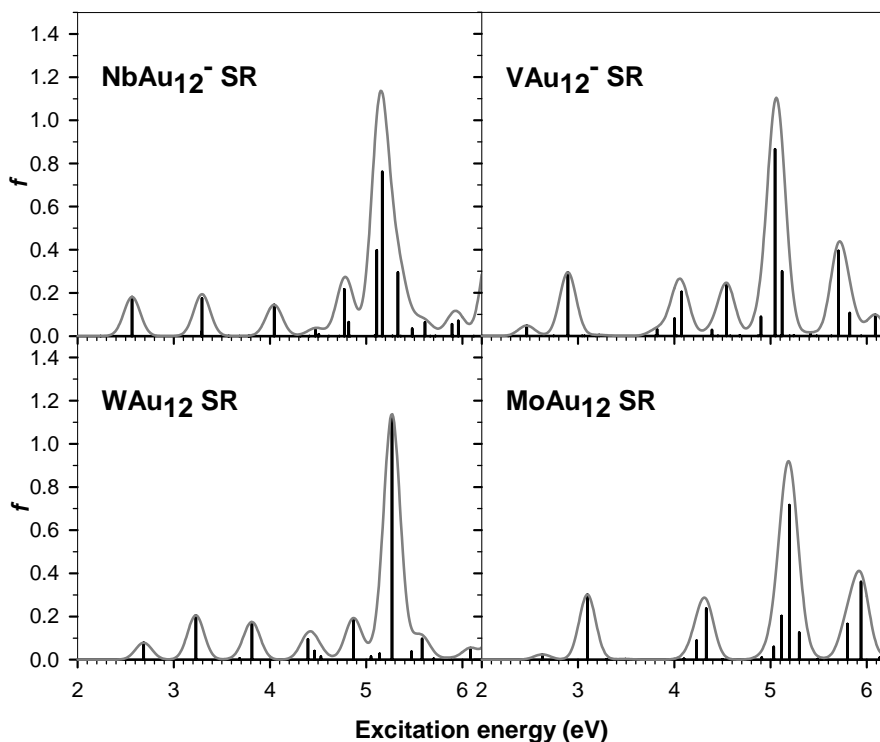


Figure 6.3 Scalar relativistic TDDFT excitation spectrum of NbAu_{12}^- and VAu_{12}^- (present work) compared with those of WAu_{12} and MoAu_{12} taken from ref. 6.10. The discrete lines have been convoluted with Gauss functions of 0.2 eV FWHM.

From a qualitative inspection of the figures of the spectra at the SR level, there is a strong resemblance between WAu_{12} and NbAu_{12}^- , in particular the three lowest transitions of the former at 2.69, 3.23 and 3.81 eV correspond closely to those found in the latter at 2.57, 3.29 and 4.04 eV respectively, moreover also the nature of the transitions is the same in the two clusters, as well as the transitions at higher energies have similar nature. The SO coupling of course introduce some extra mixing, however the two clusters retain strong similarities both in the spectra appearance and nature of the transitions.

Another strong similarity is found between MoAu_{12} and VAu_{12}^- : in particular the very low intensity of the first transition with respect to the second one is a common feature of both clusters, these features are followed by an energy gap of about 1 eV before to find, at around 4 eV, a pair of very close transitions with the same nature in both clusters. Also in this case

the SO coupling introduces some differences but the qualitative analogies between the two clusters are kept to large extent.

In summary, we have found strong W - Nb and Mo - V analogies, this is somehow surprising since it is a "diagonal" relationship in the periodic table. Actually, "diagonal" relationships inside the periodic table are well known, but they are usually ascribed to cancellation effects between atomic radius contraction along the period (row) and expansion along the group (column). We do not find these relationships between atomic radii for the pairs W - Nb and Mo - V, so the origin of the present "diagonal" relationships must be found elsewhere. In fact, we may try to identify these relationships from the cluster electronic structures, in particular there are two characteristics of the clusters which are very sensitive to the nature of the encapsulated metal: 1) the HOMO-LUMO gap and 2) the energy range spanned by the three lowest virtual levels, which corresponds, for example, to the $8h_g - 5a_g$ energy gap in VAu_{12}^- . Consider now the two gaps in the series of isoelectronic clusters reported in Table 6.4: the clusters pairs $MoAu_{12} - VAu_{12}^-$ and $WAu_{12} - NbAu_{12}^-$ are found to have almost the same $8h_g - na_g$ energy gap, the maximum difference being only 0.14 eV for $WAu_{12} - NbAu_{12}^-$. Moreover, also the HOMO-LUMO gaps are very similar in WAu_{12} and $NbAu_{12}^-$, while in VAu_{12}^- , the HOMO-LUMO gap is just 0.35 eV narrower than in $MoAu_{12}$. These analogies in the electronic structure are probably the causes of the observed "diagonal" relationships.

	$\varepsilon(8h_g) - \varepsilon(7h_g)$	$\varepsilon(na_g) - \varepsilon(8h_g)$
WAu_{12}	1.75	0.67
$MoAu_{12}$	1.60	1.27
$TaAu_{12}^-$	2.02	0.22
$NbAu_{12}^-$	1.82	0.81
VAu_{12}^-	1.25	1.28

Table 6.4 HOMO - LUMO gaps [$\varepsilon(8h_g) - \varepsilon(7h_g)$] and energy range spanned by the three lowest virtual levels [$\varepsilon(na_g) - \varepsilon(8h_g)$] in a series of isoelectronic neutral and anionic MAu_{12} clusters. Values in eV.

In Table 6.4 the reported HOMO/LUMO gaps have been obtained as KS eigenvalues differences, however we have also calculated at the SR level the dipole forbidden HOMO \rightarrow LUMO transitions. The so obtained singlet-singlet excitation of lowest energy is the T_{2g} for all the clusters considered in the table, and its energy is in practice equal to the HOMO/LUMO eigenvalues difference within 0.01 eV. Although the HOMO/LUMO transitions do not play a particular role in the present systems, they are more interesting for $W\text{Au}_{12}$ and MoAu_{12} , since they may be directly compared with the photodetachment experiment on the *negative* $W\text{Au}_{12}^-$ and MoAu_{12}^- . In fact the energy difference between the X and A features in the photodetachment measurement reported in Figure 1 of Ref. 6.8 have been assigned to the excitation energy to the first excited state of the neutral cluster. For $W\text{Au}_{12}$ and MoAu_{12} we have calculated the first excited state at the SR TDDFT level, which for both systems has resulted to be the HOMO \rightarrow LUMO singlet-triplet with A_{1g} symmetry. The corresponding calculated excitation energies are 1.39 eV and 1.15 eV for $W\text{Au}_{12}$ and MoAu_{12} , while the experimental values are 1.68 and 1.48 eV respectively, so the agreement between theory and experiment is nice, with an absolute error of only 0.3 eV. Moreover, the theory reproduces very well the observed energy decrease of 0.20 eV for this excitation going from $W\text{Au}_{12}$ to MoAu_{12} , whose calculated value is 0.24 eV in excellent agreement with the experiment and therefore confirming the good accuracy of the present formalism to treat the photoabsorption process in these systems.

6.4. CONCLUSIONS

The calculated photoabsorption spectra of the present clusters have proven rather sensitive to the nature of the encapsulated atom. This finding suggests that the optical properties of such systems might be tuned by a proper selection of the element to be inserted. The SO effects play an important role, so a theoretical description of the valence electron excitations must include SO if an accurate description is required. A comparison with the neutral isoelectronic clusters $W\text{Au}_{12}$ and MoAu_{12} suggests a somehow unexpected relationship along the diagonal of the periodic table, which can be related to the wideness of the three lowest virtual molecular orbitals involved in the excitations. Such results suggest that future efforts to perform experimental photoabsorption measurements on these systems would be very useful to have a better understanding of their optical properties. Of course also alternative methods

of production, for example using proper counterions, would help to discover new materials and to furnish macroscopic sample quantities for spectroscopic characterization.

6.4.1. Acknowledgements

This work has been supported by grants from MIUR (Programmi di Ricerca di Interesse Nazionale PRIN 2006) of Italy and by INSTM (Progetto PRISMA 2004).

Table 6.1

Scalar Relativistic			
Excitation	E_{exc} (eV)	f	excited state composition (main configuration contributions)
2 T_{1u}	2.60	0.235	$7h_g$ (Au: 6s 38% 6p 16% 5d 26%, Ta: 5d 20%) \rightarrow $5t_{2u}$ (Au: 6s 79% 6p 13%)
3 T_{1u}	3.51	0.073	$7t_{1u}$ (Au: 6s 41% 5d 48%) \rightarrow $8h_g$ (Au: 6s 27% 6p 14%, Ta: 5d 53%)
6 T_{1u}	3.74	0.220	$7t_{1u} \rightarrow 6a_g$ (Au: 6s 36% 6p 45%, Ta: 6s 17%)
13 T_{1u}	4.53	0.277	$7h_g \rightarrow 8t_{1u}$ (Au: 6s 31% 6p 44%, Ta: 6p 25%)
22 T_{1u}	5.19	1.111	39% $5h_g$ (Au: 5d) \rightarrow $5t_{2u}$ 30% $7h_g \rightarrow 4g_u$ (Au: 6p 85% 5d 16%)
23 T_{1u}	5.36	0.367	32% $6t_{1u}$ (Au: 5d) \rightarrow $8h_g$ 31% $5h_g \rightarrow 5t_{2u}$
25 T_{1u}	5.42	0.123	61% $6t_{1u} \rightarrow 8h_g$ 23% $5h_g \rightarrow 5t_{2u}$
28 T_{1u}	5.68	0.192	52% $2g_g$ (Au: 5d) \rightarrow $5t_{2u}$ 20% $6t_{1u} \rightarrow 6a_g$
Spin Orbit			
Excitation	E_{exc} (eV)	f	excited state composition (main configuration contributions)
6 T_{1u}	2.62	0.202	48% $8g_g$ (3/2) ($7h_g$) \rightarrow $11i_u$ (5/2) ($5t_{2u}$) 43% $11i_g$ (5/2) ($7h_g$) \rightarrow $11i_u$ (5/2) ($5t_{2u}$)
17 T_{1u}	3.47	0.150	30% $6e_{1u}$ (1/2) ($7t_{1u}$) \rightarrow $9g_g$ (3/2) ($8h_g$) 29% $10g_u$ (3/2) ($7t_{1u}$) \rightarrow $8e_{1g}$ (1/2) ($6a_g$)
32 T_{1u}	3.84	0.052	$6e_{1u}$ (1/2) ($7t_{1u}$) \rightarrow $8e_{1g}$ (1/2) ($6a_g$)
70 T_{1u}	4.47	0.231	40% $8g_g$ (3/2) ($7h_g$) \rightarrow $7e_{1u}$ (1/2) ($8t_{1u}$) 27% $11i_g$ (5/2) ($7h_g$) \rightarrow $11g_u$ (3/2) ($8t_{1u}$)
72 T_{1u}	4.60	0.129	30% $11i_g$ (5/2) ($7h_g$) \rightarrow $4e_{2u}$ (7/2) ($4g_u$) 22% $11i_g$ (5/2) ($7h_g$) \rightarrow $12i_u$ (5/2) ($4g_u$) 22% $7i_u$ (5/2) ($59\% 4t_{2u} + 21\% 2h_u + 14\% 2g_u$) \rightarrow $12i_g$ (5/2) ($8h_g$)
85 T_{1u}	5.20	0.633	$8g_u$ (3/2) ($49\% 6t_{1u} + 37\% 2h_u$) \rightarrow $12i_g$ (5/2) ($8h_g$)
87 T_{1u}	5.33	0.488	$8g_u$ (3/2) ($49\% 6t_{1u} + 37\% 2h_u$) \rightarrow $8e_{1g}$ (1/2) ($6a_g$)
93 T_{1u}	5.52	0.286	43% $5e_{1u}$ (5/2) ($77\% 6t_{1u} + 16\% 5t_{1u}$) \rightarrow $9g_g$ (3/2) ($8h_g$) 42% $6g_g$ (3/2) ($6h_g$) \rightarrow $11i_u$ (5/2) ($5t_{2u}$)

Table 6.1 T_{1u} valence scalar relativistic and spin-orbit excitation spectrum of TaAu_{12}^- . Excitation energy (E_{exc}), oscillator strength (f) and excited state composition in terms of monoexcited configurations are reported.

Table 6.2

Scalar Relativistic			
Excitation	E_{exc} (eV)	f	excited state composition (main configuration contributions)
2 T_{1u}	2.57	0.181	$7h_g$ (Au: 6s 35% 6p 14% 5d 26%, Nb: 4d 23%) \rightarrow $5t_{2u}$ (Au: 6s 78% 6p 14%)
4 T_{1u}	3.29	0.175	$6t_{1u}$ (Au: 6s 46% 5d 47%) \rightarrow $8h_g$ (Au: 6s 31% 6p 16%, Nb: 4d 47%)
10 T_{1u}	4.04	0.145	$6t_{1u} \rightarrow 5a_g$ (Au: 6s 29% 6p 49% 5d 10%, Nb: 5s 20%)
18 T_{1u}	4.77	0.216	$7h_g \rightarrow 7t_{1u}$ (Au: 6s 25% 6p 54%, Nb: 5p 20%)
22 T_{1u}	5.11	0.397	52% $5t_{1u}$ (Au : 5d) \rightarrow $8h_g$ 21% $5h_g$ (Au : 5d) \rightarrow $5t_{2u}$
23 T_{1u}	5.17	0.761	42% $5t_{1u} \rightarrow 8h_g$ 20% $7h_g \rightarrow 4g_u$ (Au: 6p)
25 T_{1u}	5.33	0.295	$5h_g \rightarrow 5t_{2u}$
Spin Orbit			
Excitation	E_{exc} (eV)	f	excited state composition (main configuration contributions)
6 T_{1u}	2.49	0.157	51% $11i_g$ (5/2) ($7h_g$) \rightarrow $11i_u$ (5/2) ($5t_{2u}$) 36% $8g_g$ (3/2) ($7h_g$) \rightarrow $11i_u$ (5/2) ($5t_{2u}$)
10 T_{1u}	3.03	0.092	$9g_u$ (3/2) ($6t_{1u}$) \rightarrow $12i_g$ (5/2) ($8h_g$)
17 T_{1u}	3.34	0.047	$5e_{1u}$ (1/2) ($6t_{1u}$) \rightarrow $9g_g$ (3/2) ($8h_g$)
33 T_{1u}	3.75	0.112	$9g_u$ (3/2) ($6t_{1u}$) \rightarrow $7e_{1g}$ (1/2) ($5a_g$)
50 T_{1u}	4.17	0.042	$5e_{1u}$ (1/2) ($6t_{1u}$) \rightarrow $7e_{1g}$ (1/2) ($5a_g$)
72 T_{1u}	4.56	0.097	$11i_g$ (5/2) ($7h_g$) \rightarrow $10g_u$ (3/2) ($7t_{1u}$)
73 T_{1u}	4.67	0.169	$11i_g$ (5/2) ($7h_g$) \rightarrow $4e_{2u}$ (7/2) ($4g_u$)
75 T_{1u}	4.79	0.186	$8g_g$ (3/2) ($7h_g$) \rightarrow $6e_{1u}$ (1/2) ($7t_{1u}$)
86 T_{1u}	5.10	0.135	$4e_{1u}$ (1/2) (67% $5t_{1u}$ + 29% $4t_{1u}$) \rightarrow $9g_g$ (3/2) ($8h_g$)
89 T_{1u}	5.30	0.567	$6g_u$ (3/2) (60% $2h_u$ + 36% $5t_{1u}$) \rightarrow $9g_g$ (3/2) ($8h_g$)
91 T_{1u}	5.37	0.537	$6g_u$ (3/2) (60% $2h_u$ + 36% $5t_{1u}$) \rightarrow $9g_g$ (3/2) ($8h_g$)
92 T_{1u}	5.43	0.120	$6g_g$ (3/2) (82% $6h_g$ + 10% $5h_g$) \rightarrow $11i_u$ (5/2) ($5t_{2u}$)

Table 6.2 T_{1u} valence scalar relativistic and spin-orbit excitation spectrum of NbAu_{12}^- . Excitation energy (E_{exc}), oscillator strength (f) and excited state composition in terms of monoexcited configurations are reported.

Table 6.3

Scalar Relativistic			
Excitation	E_{exc} (eV)	f	excited state composition (main configuration contributions)
2 T_{1u}	2.47	0.048	65% $7h_g$ (Au: 6s 36% 6p 14% 5d 22%, V: 3d 28%) \rightarrow $5t_{2u}$ (Au: 6s 78% 6p 14%) 34% $6t_{1u}$ (Au: 6s 37% 6p 13% 5d 49%) \rightarrow $8h_g$ (Au: 6s 32% 6p 11%, V: 3d 54%)
4 T_{1u}	2.89	0.295	61% $6t_{1u}$ \rightarrow $8h_g$ 26% $7h_g$ \rightarrow $5t_{2u}$
12 T_{1u}	4.00	0.081	61% $2h_u$ (Au : 5d) \rightarrow $8h_g$ 34% $6t_{1u}$ \rightarrow $5a_g$ (Au: 6s 29% 6p 52, V: 4s 20%)
14 T_{1u}	4.08	0.204	39% $6t_{1u}$ \rightarrow $5a_g$ 36% $2h_u$ \rightarrow $8h_g$
17 T_{1u}	4.54	0.240	$7h_g$ \rightarrow $7t_{1u}$ (Au: 6s 33% 6p 44%, V: 4p 25%)
22 T_{1u}	4.90	0.089	$6h_g$ (Au: 5d) \rightarrow $5t_{2u}$
23 T_{1u}	5.05	0.866	49% $7h_g$ \rightarrow $4g_u$ (Au: 6p 84% 5d 16%) 21% $3t_{2u}$ (Au: 5d) \rightarrow $8h_g$
26 T_{1u}	5.12	0.299	$3t_{2u}$ \rightarrow $8h_g$
32 T_{1u}	5.71	0.394	54% $4t_{1u}$ (Au : 6s 31% 5d 53%, V: 4p 16%) \rightarrow $8h_g$ 27% $2g_g$ (Au: 5d) \rightarrow $5t_{2u}$
Spin Orbit			
Excitation	E_{exc} (eV)	f	excited state composition (main configuration contributions)
10 T_{1u}	2.59	0.081	41% $10i_u$ (5/2) (59% $3g_u$ + 31% $3h_u$) \rightarrow $9g_g$ (3/2) ($8h_g$) 36% $9g_u$ (3/2) ($6t_{1u}$) \rightarrow $12i_g$ (5/2) ($8h_g$)
12 T_{1u}	2.65	0.053	$10i_u$ (5/2) (59% $3g_u$ + 31% $3h_u$) \rightarrow $9g_g$ (3/2) ($8h_g$)
17 T_{1u}	2.87	0.137	$5e_{1u}$ (1/2) ($6t_{1u}$) \rightarrow $9g_g$ (3/2) ($8h_g$)
45 T_{1u}	3.73	0.066	38% $7i_u$ (5/2) (43% $4t_{2u}$ + 40% $2h_u$ + 11% $2g_u$) \rightarrow $9g_g$ (3/2) ($8h_g$) 26% $7i_u$ (5/2) (43% $4t_{2u}$ + 40% $2h_u$ + 11% $2g_u$) \rightarrow $12i_g$ (5/2) ($8h_g$) 22% $9g_u$ (3/2) ($6t_{1u}$) \rightarrow $7e_{1g}$ (1/2) ($5a_g$)
49 T_{1u}	3.91	0.110	$7i_u$ (5/2) (43% $4t_{2u}$ + 40% $2h_u$ + 11% $2g_u$) \rightarrow $12i_g$ (5/2) ($8h_g$)
63 T_{1u}	4.31	0.072	$11i_g$ (5/2) ($7h_g$) \rightarrow $10g_u$ (3/2) ($7t_{1u}$)
78 T_{1u}	4.57	0.143	$8g_g$ (3/2) ($7h_g$) \rightarrow $6e_{1u}$ (1/2) ($7t_{1u}$)
79 T_{1u}	4.64	0.186	$11i_g$ (5/2) ($7h_g$) \rightarrow $4e_{2u}$ (7/2) ($4g_u$)
86 T_{1u}	4.99	0.101	$6g_u$ (3/2) (57% $2h_u$ + 40% $5t_{1u}$) \rightarrow $12i_g$ (5/2) ($8h_g$)
88 T_{1u}	5.03	0.315	$7i_g$ (5/2) (73% $5h_g$ + 20% $2g_g$) \rightarrow $11i_u$ (5/2) ($5t_{2u}$)
93 T_{1u}	5.21	0.651	$7i_g$ (5/2) (73% $5h_g$ + 20% $2g_g$) \rightarrow $11i_u$ (5/2) ($5t_{2u}$)

Table 6.3 T_{1u} valence scalar relativistic and spin-orbit excitation spectrum of VAu_{12}^- . Excitation energy (E_{exc}), oscillator strength (f) and excited state composition in terms of monoexcited configurations are reported.

7. THEORETICAL STUDY ON THE X-RAY ABSORPTION AT THE SULPHUR K-EDGE IN GOLD NANOPARTICLES

Nardelli, A.; Fronzoni, G.; Stener, M. *J. Phys. Chem.*, **2009**, submitted.

A Time Dependent Density Functional Theory method has been employed to study the XANES sulphur K-edge spectra in a series of gold methylthiolate clusters, taken as molecular models for gold nanoparticles protected by dodecanethiol. The calculated spectra of all the clusters here considered show two intense maxima, separated by 2 - 3 eV, preceded by a weak feature. This latter is sensitive to the nature of the S-Au coordination geometry. On the basis of the calculations, we have proposed a revised interpretation of the experimental spectrum: the intense experimental maximum is actually contributed by the two intense maxima found in the calculations, which are not resolved in the measurement. The weak experimental feature at low energy suggests that in the real gold nanoparticle a bridge S-Au coordination geometry is present.

7.1. INTRODUCTION

One of the most important goal of nanoscience is to understand the strict interplay between structure and electronic properties of nano-sized metallic clusters. For such systems, two main contributions are important to assess their properties with respect to bulk metals: the quantum confinement of electrons and the surface effects. A typical class of such systems are the gold clusters (nanoparticles) which have recently attracted much interest, both experimentally and theoretically.^{7.1} Gold nanoparticles exhibit peculiar optical properties, and can be synthesized controlling to some extent their size and shape, with a conventional chemical synthesis.^{7.2-7.5} Therefore it has become possible to produce samples of gold nanoparticles having defined shape and size distributions, whose structures can be characterized with conventional electron microscope techniques. Such syntheses are performed in solutions, so gold nanoparticles must be stabilized with proper ligands, which can be surfactants or more chemically specific ones

such as thiolates. These latter are probably the most common stabilizing agents for gold clusters, due to the specific and relatively strong Au-S chemical bond. Besides structural characterization by electron microscope, gold nanoparticles can be characterized by a series of electron spectroscopic techniques, ranging from UV-visible (where Surface Plasmon Band represents the most salient spectral feature) up to X-Ray absorption spectroscopy. In particular X-Ray Absorption Near-Edge Spectroscopy (XANES) is a very appealing technique since it probes selectively a specific atomic site, a very useful advantage especially for complex systems like the present ones, and from the intensity distribution a map of the unoccupied virtual orbitals lying on that specific site can be obtained. More precisely, given a specific atomic edge the XANES intensity maps the dipole-allowed atomic contribution of the unoccupied orbitals on that site. In the present work we have considered the S K-edge, so the intensity will map the S $2p$ contribution of the virtual orbitals. Such edge is particularly interesting, because S $2p$ orbitals are involved in the Au-S covalent bond, and therefore we expect that S K-edge XANES may help to clarify the nature of the interaction between gold and sulphur as well as the interplay between the geometrical and the electronic structure of the nanoparticles. For these reasons XANES experimental studies on gold nanoparticles have recently started to appear in the literature, such works have identified interesting phenomena, like for example the interplay between size and surface effects^{7.6} and the selective capping^{7.7} to tailor the electronic behaviour. Therefore we have considered interesting to supplement the available experimental findings with a theoretical study, in order to have a more grounded interpretation of the spectral features in terms of electronic structure. In particular with this study we want to elucidate the nature of the observed spectral features in terms of electronic structure, more precisely we employ the theory to give an assignment to the core electron excitations observed in the spectra. Of course this is not an easy task due to the large number of transitions present in the spectra of these large systems.

It is worth noting that the structure of the nanoparticles is not known, therefore we have been forced to employ a series of gold clusters stabilized by thiolates, whose structures have been taken from the literature, as possible molecular models for the nanoparticles. Since the clusters of the series differ by shape and size, we have considered interesting to try to identify specific spectral features which can be correlated to the shape of the cluster.

Finally it is important to consider that the theoretical study of core electron excitations in large systems has become now feasible thanks to recent computational developments. We have employed the Time Dependent Density Functional Theory (TDDFT) formalism to calculate electronic excitation spectra, with the modified scheme specifically designed for core

excitations. Relativistic effects have been considered in the calculation as well within the Zero Order Regular Approximation (ZORA),^{7,8} due to the presence of gold atom whose chemistry is strongly affected by relativity.^{7,9} Finally it must be considered that the efficient parallel implementation of the TDDFT algorithm made practicable the calculations of large systems, like the clusters considered in this work.

7.2. THEORETICAL METHOD

The first step consists in a conventional Scalar Relativistic (SR) Self-Consistent Field (SCF) Kohn-Sham (KS) calculation, employing a Slater Type Orbitals (STO) basis set with the ADF code.^{7,10,7.11} Relativistic effects are included at the Scalar Relativistic (SR) level within the Zero Order Regular Approximation (ZORA) formalism.

The results of the SR-KS calculation (KS eigenvalues and orbitals) are then used as input for the following TDDFT section. The TDDFT approach for electron excitations and its implementation in the ADF code has been described in detail in the literature,^{7.12} so here we just recall the salient steps.

The general problem is cast in the following eigenvalue equation:

$$\Omega \mathbf{F}_I = \omega_I^2 \mathbf{F}_I \quad (7.1)$$

where Ω is a four indexes matrix with elements $\Omega_{ia\sigma, jb\tau}$, the indexes consist of products of occupied-virtual (ia and jb) KS orbitals, while σ and τ refer to the spin variable. The eigenvalues ω_I^2 correspond to squared excitation energies while the oscillator strengths are extracted from the eigenvectors \mathbf{F}_I .^{7.13} The Ω -matrix elements can be expressed in terms of KS eigenvalues (ε) and the coupling matrix K :

$$\Omega_{ia\sigma, jb\tau} = \delta_{\sigma\tau} \delta_{ij} \delta_{ab} (\varepsilon_a - \varepsilon_i)^2 + 2\sqrt{(\varepsilon_a - \varepsilon_i)} K_{ia\sigma, jb\tau} \sqrt{(\varepsilon_b - \varepsilon_j)} \quad (7.2)$$

the elements of the coupling matrix K are given by:

$$K_{ij\sigma,kl\tau} = \int d\mathbf{r} \int d\mathbf{r}' \varphi_{i\sigma}(\mathbf{r}) \varphi_{j\sigma}(\mathbf{r}) \left[\frac{1}{|\mathbf{r}-\mathbf{r}'|} + f_{xc}^{\sigma\tau}(\mathbf{r}, \mathbf{r}', \omega) \right] \varphi_{k\tau}(\mathbf{r}') \varphi_{l\tau}(\mathbf{r}') \quad (7.3)$$

where φ are the KS orbitals and $f_{xc}^{\sigma\tau}(\mathbf{r}, \mathbf{r}', \omega)$ is the exchange-correlation kernel. In this work the kernel is approximated according to the Adiabatic Local Density Approximation (ALDA).^{7.14}

In order to extract efficiently core electron excitations, we solve equation (7.1) over a reduced space of occupied-virtual pairs, where the index of the occupied ones (i or j) is limited to run only on the core orbital under study (S 1s in present case).^{7.15}

7.3. COMPUTATIONAL DETAILS

The geometries of the clusters have been optimized with the scalar relativistic ZORA formalism^{7.8} implemented in the ADF program.^{7.10,7.11} To this end we have employed the ZORA Triple Zeta Polarized basis set, designed by the acronym ZORA TZ2P in the ADF basis set database, with frozen core up to 4*f* for Au, 2*p* for S and 1*s* for C, and the PW91 exchange correlation functional.^{7.16,7.17}

The TDDFT calculations have been performed at the optimized geometries, the basis set employed was the same as for the geometry optimization for Au, C and H, while for S a larger all electron basis set has been chosen (referenced as ET-QZ3P-1DIFFUSE in the ADF database). For the TDDFT calculations the LB94^{7.18} exchange correlation potential has been employed. We have chosen LB94 since it has the correct asymptotic behaviour, namely the Coulomb tail at large distances, which has proven very important for an accurate description of electron excitations calculated at the TDDFT level.^{7.19}

7.4. RESULTS AND DISCUSSION

The main goal of the present work is to rationalize the S K-edge XANES data reported in a previous experimental study, performed on a series of gold nanoparticles of increasing size,

protected by *n*-dodecanethiol.^{7.6} Therefore, we have two different problems to deal with in reaching this objective: first we do not know the exact structure of the gold nanoparticle, so we must choose some molecular models hopefully able to simulate to some extent the geometrical and the electronic structure of the nanoparticle, second we have to calculate and interpret the spectra for the model systems, compare with the experiment and rationalize it.

7.4.1. Model clusters

In order to simulate the nanoparticle we have chosen four possible model systems consisting of gold clusters protected by thiolates, adopting the following criteria: (i) only SCH₃ thiolates are considered for sake of computational economy, (ii) only gold thiolates clusters already studied in the literature have been chosen in order to work with realistic systems, (iii) the model series must contain a sufficient number of terms in order to cover all the possible coordination geometries of the SCH₃ group over the gold surfaces, namely the on-top, bridge and three-fold coordination.

Keeping in mind these three criteria and from a literature survey, we have decided to select four systems of increasing size, in particular we have chosen: the *O_h* [Au₁₃(SCH₃)₈]³⁺ (**1**),^{7.20} the FCC1 (**2**) and FCC2 (**3**) *D_{3d}* isomers of [Au₂₅(SCH₃)₁₈]⁺,^{7.21} the *O_h* isomer of [Au₁₄[(AuSCH₃)₄]₆]²⁺ (**4**).^{7.22} The optimized geometries of all the clusters are reported in Figure 7.1. Notice the different coordination geometry of the SCH₃ moiety with respect to the surface of the gold core: it is three-fold in (**1**), in (**2**) are present both on-top and three-fold coordination geometries, in (**3**) two kinds of non-equivalent bridge coordination are present, in (**4**) the coordination is of bridge type. The 'diameters' of the clusters, defined as the maximum Au-Au distances, are 7.04 Å, 10.56 Å, 10.59 Å and 11.02 Å going in order from (**1**) to (**4**). For all clusters the optimized S-C distances are between 1.84 Å and 1.85 Å, the optimized Au-S distances are between 2.33 Å and 2.38 Å, with the only exception of a single Au-S distance in three-fold coordination of (**2**) which we found to be 2.54 Å. It is worth noting that the 2+ charge of (**4**) considered in this work is different with respect to the literature neutral charge.^{7.22} We have done so in order to avoid quasi-degeneracy in the HOMO/LUMO gap which would have given an open shell electronic structure, which cannot be treated in the following TDDFT calculations of core electron excitations. It is important to remark that our choice of the cluster models does not pretend to be exhaustive, in fact at the moment there is a lot of research activity to try to assess the most stable structures of gold thiolate clusters, as in the case, for example, of Au₃₈(SCH₃)₂₄.^{7.23,7.24}

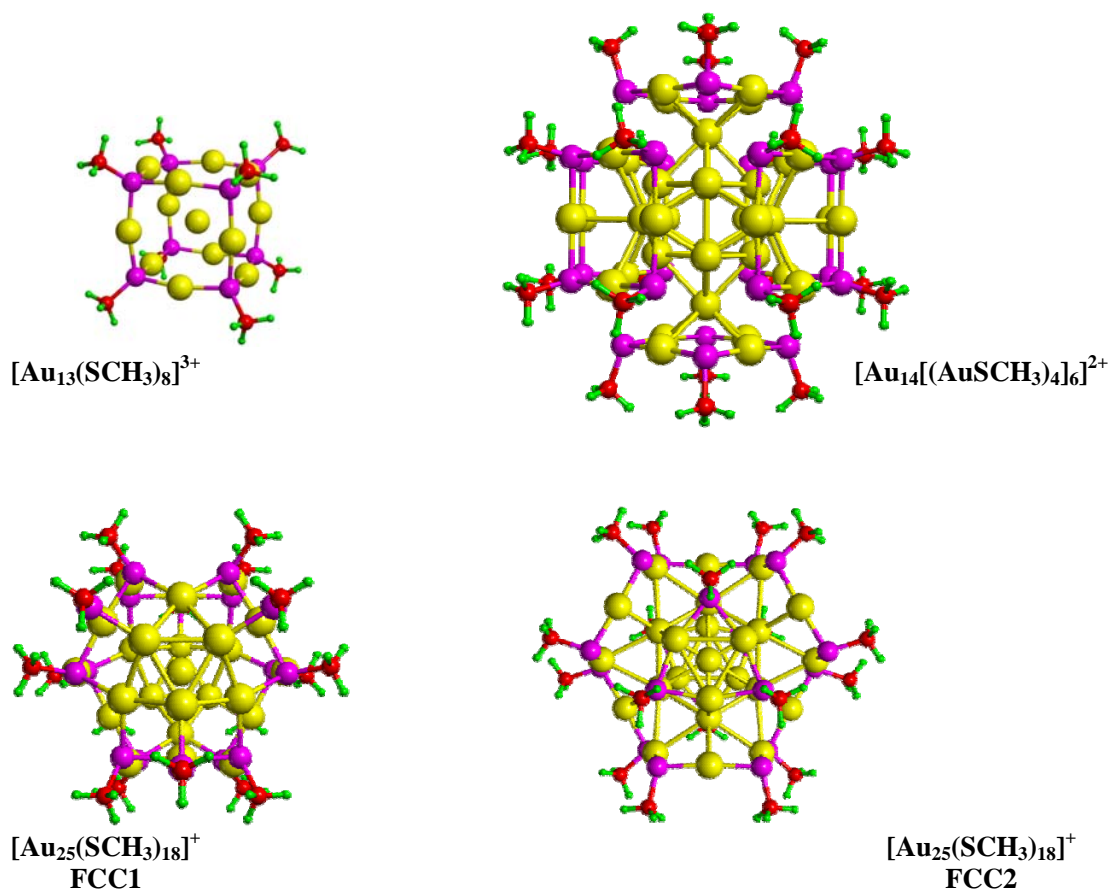


Figure 7.1 Images of the optimized geometries of the four model clusters.

7.4.2. $[\text{Au}_{13}(\text{SCH}_3)_8]^{3+}$ S K-edge calculated XANES

The TDDFT calculated S K-edge XANES spectrum of $[\text{Au}_{13}(\text{SCH}_3)_8]^{3+}$ has been reported in Table 7.1 (reported at the end of the chapter) and Figure 7.2. Only spin allowed (singlet - singlet) and dipole allowed (T_{1u} in O_h point group symmetry) transitions are considered.

Besides excitation energy and oscillator strength, we have also reported the excited state composition in terms of relevant one-electron excited configurations. Moreover, for each excited configuration which contributes to a given excited state, we also considered the composition of the virtual orbital which becomes occupied upon excitation. This analysis is inherent to the TDDFT method, in fact it can be shown^{7.13} in general that the electron excitations calculated by the TDDFT formalism can be represented by a linear combination of one-electron excited determinants (1h-1p), obtained promoting only one electron from the original Kohn-Sham determinant to all possible virtual orbitals. Therefore two-electron and higher excitations are not included in the TDDFT formalism. In the present TDDFT scheme for core excitations^{7.15}, all the excited configurations are constrained to originate from the

core S 1s orbitals. In Figure 7.2 we have reported the calculated XANES spectrum of $[\text{Au}_{13}(\text{SCH}_3)_8]^{3+}$, in terms of discrete lines. Since such lines are very dense, and for larger clusters they become even denser and denser, we have also convoluted them with Gauss functions having a Full Width Half Maximum (FWHM) of 1 eV. This procedure allows to identify more easily the spectral regions where the intensity tends to accumulate.

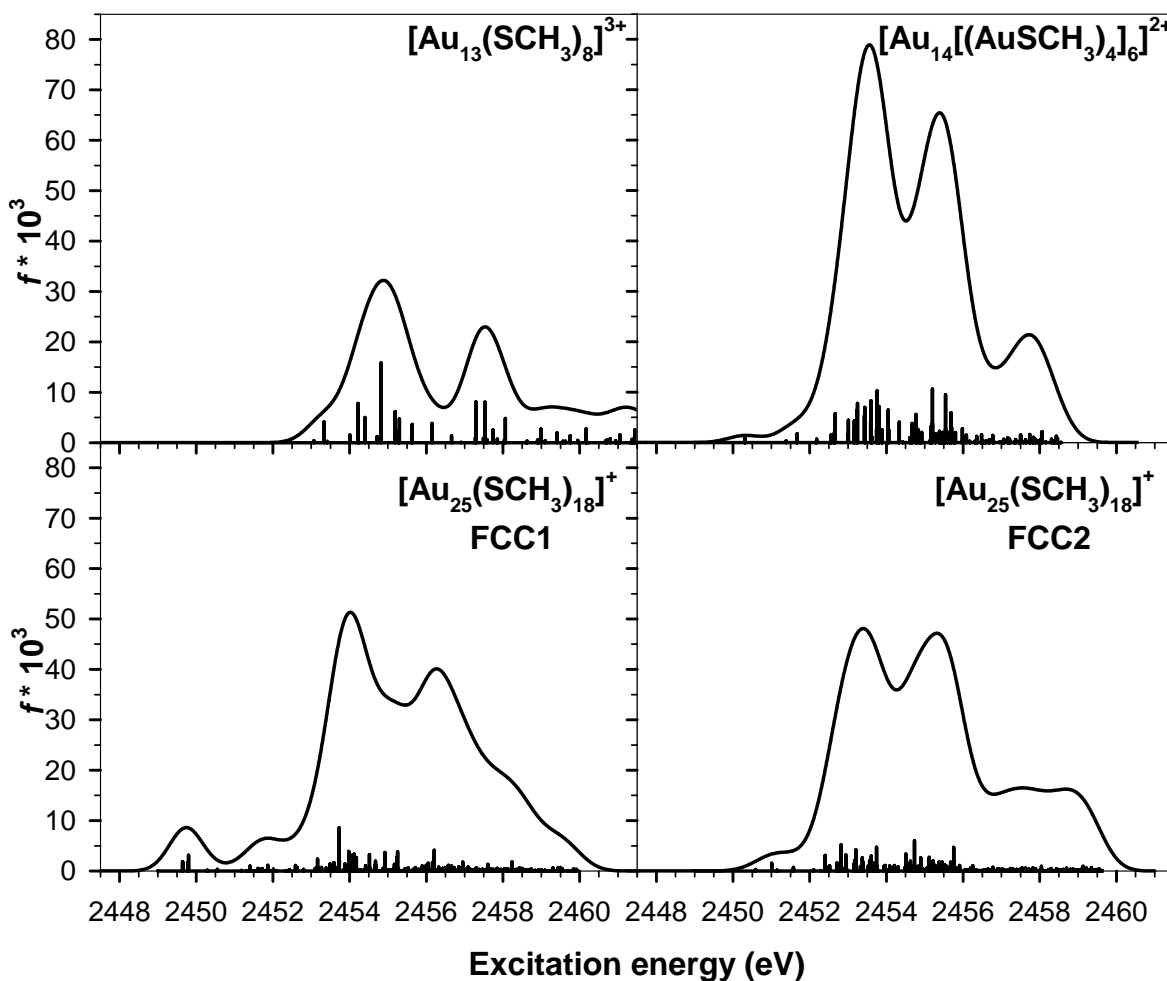


Figure 7.2 TDDFT calculated XANES S K-edge spectra of the four clusters (discrete lines). Solid line: convolution with gaussian functions with FWHM = 1 eV.

The convoluted profile is characterized by two distinct maxima, well separated by 2.7 eV, followed by a smooth tail. It is worth noting that the first maximum is preceded by a weak shoulder, which can be attributed to a single discrete line calculated at 2453.33 eV, which corresponds to 1.5 eV before the first maximum. Although this first cluster is still too small to be a good model for the nanoparticles, it is interesting to recall the shape and the interpretation of the experimental XANES spectra,^{7,6} in order to see if present calculations may add something in this respect. The experiment has been performed on a series of

nanoparticles, with diameters from 1.6 nm up to 4.0 nm, therefore we may reasonably hope that our larger models whose dimensions are around 1.1 nm can mimic at least qualitatively the XANES of the 1.6 nm nanoparticle, while $[\text{Au}_{13}(\text{SCH}_3)_8]^{3+}$ is only 0.7 nm large. In any case the experiment of the 1.6 nm species consists in a wide and intense absorption peak, preceded by a much weaker feature visible as a thin shoulder, separated by 2.9 eV from the intense maximum. The strong absorption has been ascribed to transitions to antibonding S-C states, while the shoulder at lower energy to transitions to antibonding S-Au states. It has also been observed in the experiment that the weak shoulder at lower energy gains intensity when the cluster size increases from 1.6 nm up to 4.0 nm. So at first sight, the simplest interpretation of the experiment would be to assign the experimental features separated by 2.9 eV to the two calculated maxima separated by 2.7 eV. Although the energy separation fits very well with this assumption, the intensity distribution does not support this one, in fact the calculation predicts very similar intensities for the two features, while in the experiment the first feature is much weaker. Moreover the experimental trend with respect to cluster size suggests that smaller clusters like the present one should exhibit even weaker intensity for the first feature, and this is a second argument against the previous assignment. Therefore we are led to give the following alternative interpretation of the experiment: the strong experimental maximum corresponds actually to the two calculated maxima which are not resolved in the experiment, while the experimental shoulder would be rather ascribed to the first calculated line with appreciable intensity (transition $2T_{1u}$ in Table 7.1). We will adopt this alternative interpretation also with the larger models presently considered, in order to check if this assumption will be consistent also with respect to cluster size enlargement.

Another interesting aspect of the S K-edge XANES is the previous attribution of the two experimental features to excitation to S-Au and S-C antibonding orbitals. Our excited state analysis reported in Table 7.1 gives a definite attribution to the discrete absorption lines, so we can analyse in detail the excitation spectrum. The $2T_{1u}$ transition, by now tentatively attributed to the weak experimental shoulder, corresponds to a combination of two excited configurations, which differ only by the initial symmetrized core orbital, while the final orbital ($19t_{1u}$) is the same for both excited configurations. The analysis of the final orbital shows its very mixed nature, with relevant contributions from many atomic functions, however the main component comes from Au so we can classify qualitatively this transition as mainly $S\ 1s \rightarrow \sigma^*(\text{S-Au})$, the σ character is deduced from the 12% of S $3s$ participation, which should be formally absent for π orbitals involving the S atom. This attribution is

consistent with the experimental interpretation of the weak shoulder as a transition to the S-Au antibonding state. We refer to σ and π S-Au interaction according to the local S symmetry: for on-top coordination only σ interaction is present, for bridge coordination σ and π are simultaneously present and for hollow site one σ and two π interactions take place.

Now let's consider all the remaining transitions which lie below the first maximum of the convoluted profile, starting with $6T_{1u}$ up to $16T_{1u}$. The excited state analysis shows that they can be almost all classified as mainly $S\ 1s \rightarrow \pi^*(S-Au)$ transitions, in fact the Au contribution in the final orbitals is always preponderant with respect to the C one, moreover the absence of the S $3s$ component identifies the π nature of the final state. The $16T_{1u}$ represents the only exception, in fact in this case the C contribution is larger than the Au one and the attribution is $S\ 1s \rightarrow \sigma^*(S-C)$.

Below the second convoluted maximum, we find two lines of comparable intensity (21 and $23T_{1u}$) which can be attributed to the $S\ 1s \rightarrow \sigma^*(S-C)$ transitions, they carry most of the intensity in this energy region. $17T_{1u}$ and $30T_{1u}$ do not contain C contributions, but are less important due to their lower intensity.

In summary, we can describe the assignment of the calculated S K-edge XANES in $[Au_{13}(SCH_3)_8]^{3+}$ as follows: two maxima of comparable intensity separated by 2.7 eV are obtained, the first structure is contributed mainly by $S\ 1s \rightarrow \pi^*(S-Au)$ excitations, the second one by $S\ 1s \rightarrow \sigma^*(S-C)$ transitions, the weak shoulder before the first maximum is instead ascribed to a transition whose main character is $S\ 1s \rightarrow \sigma^*(S-Au)$.

7.4.3. $[Au_{25}(SCH_3)_{18}]^+$ (FCC1 isomer) S K-edge calculated XANES

The TDDFT calculated S K-edge XANES spectrum of the FCC1 isomer of $[Au_{25}(SCH_3)_{18}]^+$ has been reported in Table 7.2 (reported at the end of the chapter) and Figure 7.2. It is worth bearing in mind that the high number of excitations makes impracticable a complete analysis as for the previous cluster, so we will consider only the most intense excitations, useful for the discussion of the calculated spectra. This cluster belongs to the D_{3d} point group, so now two different excitation symmetries A_{2u} and E_u are dipole allowed. Moreover, there are two different sets of non equivalent S $1s$ core orbitals, according to the coordination of the eighteen SCH_3 moieties, which are six on-top and twelve three-fold coordinated hollow sites, therefore we have also indicated in the table near the excitation a number (6) (on-top) or (12) (hollow) according to the nature of the excited core orbital. The convoluted spectrum (Figure

7.2) is characterized by two unresolved maxima separated by 2.0 eV in the range between 2454 and 2457 eV, preceded by two weak features at 2449.8 eV and 2451.5 eV. The two most intense features of the spectrum resemble closely the ones already seen in the previous cluster $[\text{Au}_{13}(\text{SCH}_3)_8]^{3+}$, although in the latter their separation is much larger (2.7 eV), while the low energy part differs because the weak shoulder of $[\text{Au}_{13}(\text{SCH}_3)_8]^{3+}$ is replaced by the two weak features. This suggests that the weak region at low energy is more sensitive to the cluster size and/or shape. In fact this can be better understood by an analysis of the most relevant transitions reported in Table 7.2: the main contribution of the first feature is attributed to the $4E_u$ transition at 2449.80 eV, which consists of a $S\ 1s \rightarrow \sigma^*(\text{S-Au})$ excitation of the on-top ligands. In this case the σ^* nature of the virtual orbital comes from the fact that only one gold atom is bound to S, while π interaction arises when multiple Au-S bonds interest one single sulphur atom. The second weak feature around 2452 eV contains many contributions, the most relevant is attributed to the $8E_u$ excitation from hollow sites $S\ 1s$ core states, and ends in a virtual orbital with S-Au character, this is the same nature observed for the threshold at low energy in $[\text{Au}_{13}(\text{SCH}_3)_8]^{3+}$. Then let's consider the nature of the transitions below the two intense maxima: below the first maximum the $16A_{2u}$ is the most intense transition, and is attributed to an excitation from the hollow-site $S\ 1s$ to S-Au antibonding virtual orbitals. The second maximum, instead, is characterized by transitions for $S\ 1s$ at hollow sites up to S-C virtual orbitals with antibonding character, well represented by the $120E_u$ excitation. Therefore also the nature of the two intense maxima is the same as in the previous cluster $[\text{Au}_{13}(\text{SCH}_3)_8]^{3+}$. A closer inspection to all the transitions reveals that the nature of the transitions is the same also for the weaker ones, only occasional exceptions are found but they do not change the essence of the interpretation of the spectrum.

7.4.4. $[\text{Au}_{25}(\text{SCH}_3)_{18}]^+$ (FCC2 isomer) S K-edge calculated XANES

This model is an isomer of the previous one, the most salient difference is that now the SCH_3 ligands are all coordinated to two gold atoms with a bridge geometry. Also in this case the cluster belongs to the D_{3d} point group symmetry, and the total number of 18 SCH_3 moieties is further split in two sets of 6 and 12 symmetry equivalent fragments, in the table near each excitation entry we have indicated to which group (6) or (12) the core excited orbital belongs. In this case the convoluted calculated spectrum resembles the results found for $[\text{Au}_{13}(\text{SCH}_3)_8]^{3+}$, that is two strong maxima preceded by a weak shoulder. Also the attribution

is the same, see Table 7.3 (reported at the end of the chapter) and also in this case only the most intense excitations will be considered: the $2E_u$ contributes to the shoulder and is an excitation to S-Au antibonding orbital, $17E_u$ lies below the first strong maximum and consists in a transition to S-Au orbitals, finally the high energy maximum is well represented by the $86E_u$ excitation to a S-C level. It is interesting to compare the present spectrum with respect to the FCC1 isomer, the difference being ascribed only to SCH_3 ligand coordination and not to size effects. The most interesting difference consists in the first spectral feature around 2450 eV in FCC1 which is ascribed to excitation from on-top S $1s$ core orbitals, missing completely in FCC2 due to the absence of on-top coordination in the latter. This feature appears to be specific of on-top ligand coordination and therefore can be employed as a fingerprint to identify such coordination type.

7.4.5. $[Au_{14}[(AuSCH_3)_4]_6]^{2+}$ S K-edge calculated XANES

The spectrum of this octahedral cluster is presented in Figure 7.2 as well, in Table 7.4 (reported at the end of the chapter) the usual selection of transitions is considered. This is the largest cluster we have considered in this work. Here there are few and more intense lines in the spectrum with respect to the previous smaller FCC1 and FCC2 ones, this is an effect of the higher symmetry which tends to collect intensity over fewer lines. The first transition at low energy corresponds to the $5T_{1u}$ excitation, and is responsible for a weak feature, this is followed by the $12T_{1u}$ one which appears as a tiny shoulder of the next maximum, whose leading contribution come from the $65T_{1u}$ transition. All these correspond to excitations to S-Au antibonding orbitals. The next maximum (separated by about 2.0 eV with respect to the previous one) is instead mainly contributed by $122T_{1u}$ and $139T_{1u}$, which consist in transitions towards S-C antibonding orbitals. From the complete list of excitations reported in Table 7.4 some minor exceptions can be found to the previous simplified assignment grounded only on five individual transitions, however we can say that in general the second intense maximum is mainly contributed by S-C virtual final states, the remaining features are all ascribed to excitations to S-Au antibonding orbitals.

7.4.6. Comparison with experimental data

In Figure 7.3 we compare the calculated spectra of the three largest clusters presently investigated, with the experimental S K-edge XANES measured on a sample of gold

nanoparticle with diameter of 1.6 nm protected by dodecanethiol.^{7,6} Before to start the discussion one remark is important about the energy scale: it is well known that, although the absolute TDDFT core electron excitation energies show large errors (tens of eV) with respect to the experiment, the calculated spectrum is usually in very good agreement with the experiment (in terms of intensity and relative energy), provided it is shifted by a constant value along the energy scale.^{7,15} Therefore in Figure 7.3 we have shifted the experimental profile in order to fit the maximum of the absorption profile with the calculated profile. In Figure 7.3 only the calculated profiles convoluted with a gaussian function with 1.5 eV of FWHM have been reported. The intensity scale of the experimental profile is not absolute, so it has been normalized with respect to the calculation.

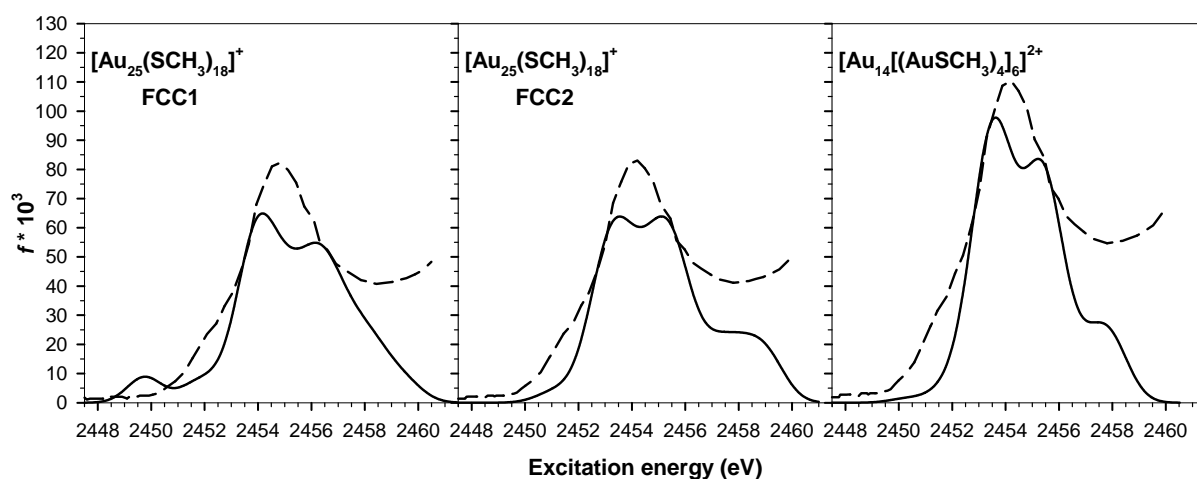


Figure 7.3 Comparison between the convoluted (FWHM = 1.5 eV) TDDFT calculated XANES S K-edge spectra of the three larger clusters (solid line) with experimental data^{7,6} for gold nanoparticles with diameter of 1.6 nm (dashed line).

The experimental profile is characterized by an intense maximum, preceded by a weak shoulder 2.9 eV below it. Our assignment consists to attribute to the experimental maximum both pair of intense calculated maxima, which are characteristic of all the model clusters here considered. With this choice the experimental weak shoulder fits properly with the weak counterparts in the calculated spectra. More interestingly, the weak feature at low energy is strongly dependent on the chosen model, and this can be profitably employed to discriminate the sulphur coordination geometry present in the nanoparticle according to the XANES spectra. In particular the FCC1 model does not fit the experimental pattern, since the calculated feature at low energy is too intense and at too low energy (roughly 5 eV), so we are led to exclude the presence of on-top sulphur coordination at gold. FCC2 and

$[\text{Au}_{14}[(\text{AuSCH}_3)_4]_6]^{2+}$ fit much better the experiment, these model clusters have both bridge (two-fold) coordination of S on Au, this supports the hypothesis that the thiol assumes this coordination in the nanoparticle. The shoulder is more pronounced in the calculated FCC2 cluster, so this seems more appropriate to simulate the nanoparticle than the larger one. Actually the shoulder is still too weak, however from the experimental data it is found that the shoulder gains intensity as cluster size increases, so in this respect present models are still too small to obtain a proper intensity ratio of the shoulder with respect to the stronger feature. Another remark pertains the attribution of the measured features to specific excitations, in the experimental work the shoulder had been assigned to excitation towards S-Au antibonding orbitals and the intense maximum to S-C states. The present calculations confirm the S-Au nature of the shoulder, but suggest that the intense maximum actually consists in a pair of unresolved bands, the first contributed by excitation to S-Au antibonding orbitals, the second to S-C ones. This also suggests that further experimental S K-edge XANES investigations with higher energy resolution on samples of well characterized gold nanoparticles protected by thiols, may allow the resolution of the intense band in two peaks, giving even more information for example from energy separation and relative intensity of the two peaks.

7.5. CONCLUSIONS

In this work we have employed a TDDFT method to study the XANES sulphur K-edge spectra in a series of gold methylthiolate clusters, with the aim to reproduce and rationalize the experimental spectra measurements on a sample of gold nanoparticles protected by dodecanethiol. The model clusters have been taken from the literature, in order to employ realistic systems although the real structures of these clusters are still debated. The molecular models have been selected in order to present different types of sulphur coordination to gold, namely on-top, bridge and hollow site in order to identify possible relationships between S-Au coordination and spectral features. All the clusters here considered show two intense maxima, separated by 2 - 3 eV, preceded by weak features. The two maxima have been ascribed to excitations of S 1s electrons to S-Au and S-C antibonding orbitals. The two maxima remain rather similar in the series, instead the weak features are very sensitive to the cluster shape. In presence of S-Au on top coordination, the weak feature appears more intense and shifted to lower energy with respect to the next strong maximum. For all the considered

clusters the weak feature at low energy is ascribed to excitations from S $1s$ to S-Au antibonding states. On the basis of the calculations, we have proposed a revised interpretation of the experimental spectrum: the intense experimental maximum is actually contributed by the two intense maxima found in the calculations, which are not resolved in the measurement. The weak experimental feature at low energy has a counterpart in the FCC2 model cluster and therefore suggests the bridge S-Au coordination in the real nanoparticle. This work also suggests that further measurements with higher spectral resolution and on monodispersed samples may allow the resolution of the strong maximum in its two components and therefore extract more complete information for example from the direct measurement of the energy shift between the two bands and their intensity ratio.

7.5.1. Acknowledgements

We thank Professor Katsuyuki Nobusada for having sent to us the coordinates of the FCC1 and the FCC2 clusters we have employed as starting points in our geometry optimizations.

This work has been supported by MIUR (Programmi di Ricerca di Interesse Nazionale PRIN 2006) of Italy, by INSTM (Progetto PRISMA 2004) and by INFM DEMOCRITOS National Simulation Center, Trieste, Italy. A generous INSTM grant of computer time on the IBM SP5 and BCX of CINECA (Bologna, Italy) is gratefully acknowledged.

Table 7.1

Excitation	E_{exc} (eV)	f	Excited state composition (main configuration contributions)
2 T_{1u}	2453.33	$4.098 \cdot 10^{-3}$	67% $1a_{1g} \rightarrow 19t_{1u}$ (Au: 6s 28% 5d 9%, C: 2p 17%, S: 3s 12% 3p 10%)
6 T_{1u}	2454.22	$7.809 \cdot 10^{-3}$	33% $1t_{2g} \rightarrow 19t_{1u}$ 66% $1a_{2u} \rightarrow 18t_{2g}$ (Au: 6s 24%, S: 3p 20% 3d 9%) 33% $1t_{1u} \rightarrow 18t_{2g}$
8 T_{1u}	2454.40	$4.992 \cdot 10^{-3}$	99% $1t_{1u} \rightarrow 11e_g$ (Au: 6s 19% 6p 20%, S: 3p 14% 3d 24%)
10 T_{1u}	2454.82	0.01583	99% $1t_{2g} \rightarrow 11t_{2u}$ (Au: 6s 23%, S: 3p 27% 3d 14% 4d 9%)
11 T_{1u}	2455.19	$6.162 \cdot 10^{-3}$	99% $1t_{1u} \rightarrow 12e_g$ (Au: 6s 9% 6p 34%, S: 3p 12%, 3d 27%)
13 T_{1u}	2455.30	$4.704 \cdot 10^{-3}$	33% $1a_{2u} \rightarrow 19t_{2g}$ (Au: 6p 21%, C: 2p 12%, S: 3p 20% 3d 9% 4d 11%) 66% $1t_{1u} \rightarrow 19t_{2g}$
16 T_{1u}	2456.16	$3.852 \cdot 10^{-3}$	100% $1t_{2g} \rightarrow 9a_{2u}$ (C: 2p 34%, S: 3p 38%, 4d 11%)
17 T_{1u}	2456.66	$1.373 \cdot 10^{-3}$	100% $1t_{1u} \rightarrow 9t_{1g}$ (Au: 6p 42%, S: 3d 28%, 5p 11%)
21 T_{1u}	2457.29	$8.079 \cdot 10^{-3}$	56% $1t_{2g} \rightarrow 22t_{1u}$ (Au ^c : 6p 13%, Au: 6p 12%, C: 2p 26%, S: 3p 22% 3d 9% 4d 11%) 28% $1a_{1g} \rightarrow 22t_{1u}$
23 T_{1u}	2457.53	$8.034 \cdot 10^{-3}$	32% $1a_{2u} \rightarrow 20t_{2g}$ (C: 2p 27%, H: 1s 39% 2s 31%, S: 3p 12% 4s 10%) 63% $1t_{1u} \rightarrow 20t_{2g}$
30 T_{1u}	2458.06	$4.821 \cdot 10^{-3}$	66% $t_{1u} \rightarrow 21t_{2g}$ (Au: 6p 23%, H: 1s 32%, 2s 19%) 33% $1a_{2u} \rightarrow 21t_{2g}$

Table 7.1 T_{1u} core S 1s excitation spectrum of $[\text{Au}_{13}(\text{SCH}_3)_8]^{3+}$. Excitation energy (E_{exc}), oscillator strength (f) and excited state composition in terms of monoexcited configurations are reported. Only the most intense excitations, whose oscillator strength is $f > 1.0 \cdot 10^{-3}$ are reported.

Table 7.2

Excitation	E_{exc} (eV)	f	Excited state composition (main configuration contributions)
2 E _u (6)	2449.65	$1.838 \cdot 10^{-3}$	50% 3e _g → 74e _u (Au: 6s 30% 5d 9%, S: 3p 26%) 49% 2a _{1g} → 74e _u
3 E _u (6)	2449.79	$1.839 \cdot 10^{-3}$	50% 2a _{2u} → 75e _g (Au: 6s 29% 6p 11%, S: 3p 27%) 50% 3e _u → 75e _g
4 E _u (6)	2449.80	$3.152 \cdot 10^{-3}$	49% 2a _{2u} → 75e _g 49% 3e _u → 75e _g
8 E _u (12)	2451.87	$1.145 \cdot 10^{-3}$	46% 1a _{1u} → 75e _g 47% 1e _u → 75e _g
4 A _{2u} (12)	2451.87	$7.338 \cdot 10^{-4}$	85% 2e _u → 75e _g
32 E _u (6)	2452.59	$1.119 \cdot 10^{-3}$	50% 2a _{1g} → 78e _u (Au: 6p 12%, C: 2p 18%, S: 3p 24%) 50% 3e _g → 78e _u
41 E _u (6)	2453.16	$2.374 \cdot 10^{-3}$	46% 2a _{2u} → 81e _g (Au: 6s 23%, S: 3p 11%, H: 1s 11% 2s 11%) 46% 3e _u → 81e _g
31 E _u (12)	2453.73	$1.220 \cdot 10^{-3}$	34% 1e _g → 76e _u (Au: 6s 23% 6p 12%, S: 3p 21%) 25% 1a _{2g} → 76e _u 14% 2e _g → 30a _{1u} (Au: 6s 24%, S: 30 3p 20% 3d 10%) 12% 1a _{1g} → 76e _u
16 A _{2u} (12)	2453.73	$8.567 \cdot 10^{-3}$	43% 1e _g → 76e _u 32% 2e _g → 76e _u
28 A _{2u} (6)	2453.73	$2.152 \cdot 10^{-3}$	59% 3e _g → 81e _u (Au: 6p 11%, S: 3d 11%, H: 1s 22% 2s 28%) 34% 2a _{1g} → 51a _{2u} (Au: 6p 11%, S: 3p 12% 3d 13%, H: 1s 18% 2s 28%)
44 E _u (12)	2453.98	$3.896 \cdot 10^{-3}$	45% 1e _u → 52a _{1g} (Au: 6s 24%, S: 3p 22% 3d 16%)
48 E _u (12)	2454.08	$3.174 \cdot 10^{-3}$	25% 1a _{2g} → 77e _u (Au: 6s 23%, S: 3p 25% 3d 11%) 22% 1a _{1u} → 79e _g (Au: 6s 10% 6p 19%, C: 2p 16%, S: 3p 18%) 22% 1e _u → 79e _g 21% 2e _g → 77e _u
51 E _u (12)	2454.12	$3.350 \cdot 10^{-3}$	25% 2e _u → 79e _g 15% 1a _{2u} → 79e _g 13% 1e _g → 49a _{2u} (Au: 6s 12% 6p 28%, C: 2p 11%, S: 3p 17%) 12% 1a _{1u} → 79e _g 11% 1a _{1g} → 77e _u
52 E _u (12)	2454.12	$2.912 \cdot 10^{-3}$	25% 1e _u → 79e _g 15% 1a _{1u} → 79e _g 13% 2e _g → 49a _{2u} 12% 1a _{2u} → 79e _g 11% 1a _{2g} → 77e _u
36 A _{2u} (6)	2454.15	$1.697 \cdot 10^{-3}$	52% 2a _{2u} → 56a _{1g} (Au: 6p 10%, C: 2p 22%, S: 4s 40% 3p 13%, H: 1s 27% 2s 27%) 37% 3e _u → 84e _g (C: 2p 21%, S: 3p 25%, H: 1s 13% 2s 10%)
53 E _u (12)	2454.17	$2.642 \cdot 10^{-3}$	83% 2e _g → 49a _{2u}
30 A _{2u} (12)	2454.52	$3.262 \cdot 10^{-3}$	94% 1e _u → 80e _g (Au: 6p 24%, S: 3p 13% 3d 20%)

50 A_{2u} (6)	2454.92	$3.666 \cdot 10^{-3}$	68% $3e_g \rightarrow 88e_u$ (C: 2p 17%, S: 3p 13% 3d 10%, H: 1s 35% 2s 23%) 25% $2a_{1g} \rightarrow 55a_{2u}$ (Au: 6p 15%, C: 2p 21%, S: 3p 16%, H: 1s 30%)
40 A_{2u} (12)	2455.23	$2.757 \cdot 10^{-3}$	34% $1a_{2u} \rightarrow 53a_{1g}$ (Au: 6s 17% 6p 11%, S: 3p 11% 3d 13%, H: 2s 14%) 32% $1e_u \rightarrow 81e_g$ 28% $2e_u \rightarrow 81e_g$
56 A_{2u} (6)	2455.24	$1.779 \cdot 10^{-3}$	95% $3e_u \rightarrow 90e_g$ (Au: 6p 12%, C: 2p 18% S: 3p 12%, H: 1s 37%)
82 E_u (12)	2455.25	$3.808 \cdot 10^{-3}$	93% $1e_u \rightarrow 29a_{2g}$ (C: 2p 27%, S: 3p 40%, 4d 10%)
73 A_{2u} (6)	2456.05	$1.532 \cdot 10^{-3}$	53% $3e_u \rightarrow 96e_g$ (C: 3p 18%, S: 4p 68% 3d 12%) 43% $3e_g \rightarrow 96e_u$ (C: 2p 13%, S: 4p 33% 3d 16%, H: 1s 23%)
75 A_{2u} (6)	2456.16	$1.725 \cdot 10^{-3}$	57% $2a_{2u} \rightarrow 63a_{1g}$ (Au: 6p 16%, S: 4p 25% 3d 24% 5s 10%) 42% $3e_u \rightarrow 97e_g$ (Au: 6p 18%, C: 2p 11%, S: 4p 31%, H: 1s 21%)
120 E_u (12)	2456.21	$4.126 \cdot 10^{-3}$	27% $1e_u \rightarrow 84e_g$ 26% $1a_{1u} \rightarrow 84e_g$ 13% $1a_{2g} \rightarrow 84e_u$ (Au: 6p 17%, C: 2p 20%, S: 3p 23% 3d 24%, H: 1s 10%)
166 E_u (12)	2456.95	$1.762 \cdot 10^{-3}$	42% $1a_{1u} \rightarrow 88e_g$ (Au: 6p 12%, S: 4p 21% 3d 13%, H: 1s 16%, 2s 21%) 23% $1e_u \rightarrow 88e_g$ 22% $2e_u \rightarrow 88e_g$
217 E_u (12)	2457.61	$1.343 \cdot 10^{-3}$	93% $2e_u \rightarrow 61a_{1g}$ (Au: 6p 15% 5s 29%, C: 3p 14%, S: 3p 12%)
270 E_u (12)	2458.24	$1.799 \cdot 10^{-3}$	49% $1e_u \rightarrow 97e_g$ 43% $1a_{1u} \rightarrow 97e_g$

Table 7.2 E_u and A_{2u} core S 1s excitation spectrum of $[\text{Au}_{25}(\text{SCH}_3)_{18}]^+$ FCC1. Excitation energy (E_{exc}), oscillator strength (f) and excited state composition in terms of monoexcited configurations are reported. Only the most intense excitations, whose oscillator strength is $f > 1.0 \cdot 10^{-3}$ are reported (exclusive of $4A_{2u}(12)$).

Table 7.3

Excitation	E_{exc} (eV)	f	Excited state composition (main configuration contributions)
2 E _u (6)	2450.59	$3.066 \cdot 10^{-4}$	50% 2a _{2u} → 75e _g (Au: 6s 39% 6p 21%, S: 3p 11%) 50% 3e _u → 75e _g
2 A _{2u} (12)	2451.01	$1.549 \cdot 10^{-3}$	100% 1e _u → 75e _g
4 A _{2u} (12)	2451.58	$7.309 \cdot 10^{-4}$	95% 1a _{2u} → 48a _{1g} (Au: 6s 29% 6p 27% 5d 11%, S: 3p 10%)
8 E _u (6)	2452.41	$3.131 \cdot 10^{-3}$	49% 2a _{2u} → 76e _g (Au: 6s 13% 6p 15%, S: 3p 25%) 49% 3e _u → 76e _g
17 E _u (6)	2452.82	$5.183 \cdot 10^{-3}$	49% 2a _{1g} → 76e _u (Au: 6s 15% 6p 11%, S: 3p 31% 3d 11%) 49% 3e _g → 76e _u
13 A _{2u} (12)	2452.94	$1.973 \cdot 10^{-3}$	53% 2e _g → 75e _u (Au: 6s 23%, S: 3p 24%) 29% 1a _{2u} → 50a _{1g} (Au: 6s 13% 6p 14%, S: 3p 21% 4s 18%) 12% 1e _g → 75e _u
25 E _u (12)	2452.94	$3.198 \cdot 10^{-3}$	33% 1a _{2g} → 75e _u 30% 2e _g → 75e _u 17% 1e _u → 50a _{1g} 12% 2e _u → 50a _{1g}
15 A _{2u} (12)	2453.17	$2.086 \cdot 10^{-3}$	85% 1e _u → 77e _g (Au: 6s 21%, S: 3p 19%) 10% 2e _g → 76e _u
17 A _{2u} (12)	2453.20	$4.215 \cdot 10^{-3}$	85% 2e _g → 76e _u
27 E _u (6)	2453.37	$2.626 \cdot 10^{-3}$	94% 3e _g → 49a _{2u} (Au: 6p 21%, S: 3p 14% 3d 15%, H: 1s 11%)
44 E _u (12)	2453.56	$2.038 \cdot 10^{-3}$	47% 1a _{1u} → 78e _g (Au: 6s 15% 6p 14%, S: 3p 20% 3d 13%) 47% 2e _u → 78e _g
45 E _u (12)	2453.61	$2.982 \cdot 10^{-3}$	81% 2e _u → 51a _{1g} (Au: 6s 16% 6p 12%, S: 3p 22% 3d 15%) 12% 1e _u → 51a _{1g}
52 E _u (12)	2453.74	$4.722 \cdot 10^{-3}$	38% 1e _g → 78e _u (Au: 6s 22%, S: 3p 19% 3d 18%) 37% 1a _{2g} → 78e _u 11% 1a _{1g} → 78e _u
28 A _{2u} (6)	2454.51	$3.354 \cdot 10^{-3}$	98% 3e _g → 81e _u (C: 2p 14%, S: 3p 25%, H: 1s 10% 2s 12%)
80 E _u (12)	2454.63	$1.976 \cdot 10^{-3}$	42% 1a _{2g} → 80e _u (Au: 6p 15%, C: 2p 13%, S: 3p 22%) 38% 1e _g → 80e _u
86 E _u (12)	2454.74	$6.012 \cdot 10^{-3}$	38% 1a _{1u} → 82e _g (Au: 6p 12%, C: 2p 14%, S: 3p 21%) 35% 2e _u → 82e _g 10% 2e _u → 54a _{1g} (Au: 6s 17%, C: 2p 23%, S: 3p 29%)
92 E _u (12)	2454.90	$2.640 \cdot 10^{-3}$	89% 1e _g → 50a _{2u} (Au: 6p 11%, C: 2p 21%, S: 3p 32% 3d 11%)
94 E _u (12)	2455.12	$2.734 \cdot 10^{-3}$	96% 1e _g → 32a _{1u} (Au: 6p 21%, C: 2p 31%, S: 3p 36%)
99 E _u (12)	2455.22	$2.026 \cdot 10^{-3}$	48% 1a _{1g} → 82e _u (Au: 6p 26%, C: 2p 16%, S: 3p 24% 4s 13%, H: 1s 14% 2s 16%) 43% 2e _g → 82e _u
105 E _u (12)	2455.37	$1.776 \cdot 10^{-3}$	48% 1a _{1g} → 83e _u (Au: 6p 13%, C: 2p 16%, S: 3p 16%, H: 1s 25% 2s 32%) 48% 2e _g → 83e _u
42 A _{2u} (6)	2455.44	$1.836 \cdot 10^{-3}$	94% 2a _{1g} → 54a _{2u} (Au: 6p 16%, C: 2p 17%, S: 3p 13%, H: 1s 27% 2s 12%)

129 E _u (12)	2455.67	1.766*10 ⁻³	25% 1e _u → 31a _{2g} (C: 2p 16%, H: 1s 56% 2s 55%) 25% 1a _{2u} → 85e _g (Au: 6p 13%, S: 3p 13% 3d 11%, H: 1s 14% 2s 24%)
48 A _{2u} (6)	2455.76	4.712*10 ⁻³	19% 2e _u → 31a _{2g} 87% 3e _u → 87e _g (C: 2p 19%, S: 3p 15%, H: 1s 38% 2s 32%)
147 E _u (12)	2455.91	1.108*10 ⁻³	49% 1a _{1g} → 86e _u (Au: 6p 15%, S: 4p 15%, H: 1s 28% 2s 37%) 47% 2e _g → 86e _u
57 A _{2u} (6)	2456.25	1.048*10 ⁻³	57% 3e _u → 90e _g (C: 2p 16%, S: 3d 16% 4p 11%, H: 1s 49%) 42% 3e _g → 90e _u (S: 4p 27%, H: 1s 48% 2s 26%)
199 E _u (12)	2456.78	7.744*10 ⁻⁴	50% 1a _{2u} → 91e _g (Au: 6p 16% 7s 11%, S: 3d 14% 4p 27%, H: 1s 22%) 48% 2e _u → 91e _g
89 A _{2u} (6)	2458.04	9.659*10 ⁻⁴	100% 3e _u → 101e _g (C: 2p 10%, S: 3d 16% 4p 57%, H: 1s 20%)

Table 7.3 E_u and A_{2u} core S 1s excitation spectrum of [Au₂₅(SCH₃)₁₈]⁺ FCC2. Excitation energy (E_{exc}), oscillator strength (*f*) and excited state composition in terms of monoexcited configurations are reported. Only the most intense excitations, whose oscillator strength is *f* > 1.0·10⁻³ are reported (exclusive of 2E_u(6), 4A_{2u}(12), 199E_u(12) and 89A_{2u}(6)).

Table 7.4

Excitation	E_{exc} (eV)	f	Excited state composition (main configuration contributions)
5 T_{1u}	2450.31	$1.030 \cdot 10^{-3}$	32% $1a_{2u} \rightarrow 43t_{2g}$ (Au: 6s 27% 6p 27% 5d 14%) 36% $1t_{1u} \rightarrow 43t_{2g}$ 17% $1e_u \rightarrow 43t_{2g}$
12 T_{1u}	2451.67	$1.777 \cdot 10^{-3}$	13% $2t_{1u} \rightarrow 43t_{2g}$ 47% $1t_{1g} \rightarrow 49t_{1u}$ (Au: 6s 33% 6p 26%) 18% $2t_{2g} \rightarrow 49t_{1u}$ 17% $1t_{2g} \rightarrow 49t_{1u}$ 16% $1e_g \rightarrow 49t_{1u}$
27 T_{1u}	2452.67	$5.739 \cdot 10^{-3}$	48% $1t_{1g} \rightarrow 50t_{1u}$ (Au: 6s 24% 5d 9%, S: 3p 24%) 36% $2t_{2g} \rightarrow 50t_{1u}$ 10% $1e_g \rightarrow 50t_{1u}$
35 T_{1u}	2453.01	$4.452 \cdot 10^{-3}$	60% $1t_{2u} \rightarrow 33e_g$ (Au: 6s 20%, S: 4s 10% 3p 23%, H: 1s 8% 2s 11%) 15% $1t_{1u} \rightarrow 33e_g$ 7% $2t_{1u} \rightarrow 33e_g$ 7% $1t_{2g} \rightarrow 51t_{1u}$ (Au: 6p 37%, C: 2p 10%, S: 3p 10% 3d 9%) 6% $1a_{1g} \rightarrow 51t_{1u}$
38 T_{1u}	2453.17	$4.310 \cdot 10^{-3}$	32% $1a_{2u} \rightarrow 44t_{2g}$ (Au: 6s 23%, S: 3p 29% 3d 11%) 29% $1t_{1u} \rightarrow 44t_{2g}$ 20% $2t_{1u} \rightarrow 44t_{2g}$ 16% $1e_u \rightarrow 44t_{2g}$
40 T_{1u}	2453.17	$2.634 \cdot 10^{-3}$	31% $1a_{2u} \rightarrow 44t_{2g}$ 31% $1t_{1u} \rightarrow 44t_{2g}$ 16% $2t_{1u} \rightarrow 44t_{2g}$ 16% $1e_u \rightarrow 44t_{2g}$
45 T_{1u}	2453.23	$6.473 \cdot 10^{-3}$	32% $1t_{1g} \rightarrow 52t_{1u}$ (Au: 6s 20% 6p 8%, S: 3p 21% 3d 17%, H: 2s 8%) 28% $1t_{2g} \rightarrow 52t_{1u}$ 21% $1e_g \rightarrow 52t_{1u}$ 9% $1a_{1g} \rightarrow 52t_{1u}$
48 T_{1u}	2453.25	$7.761 \cdot 10^{-3}$	40% $2t_{1u} \rightarrow 34e_g$ (Au: 6s 14% 6p 31%, S: 3p 19%, 3d 17%) 28% $1t_{1u} \rightarrow 34e_g$ 23% $1t_{2u} \rightarrow 34e_g$
50 T_{1u}	2453.42	$5.337 \cdot 10^{-3}$	48% $1e_u \rightarrow 33t_{1g}$ (Au: 6s 22%, S: 3p 25% 3d 14%) 36% $1t_{1u} \rightarrow 33t_{1g}$ 14% $2t_{1u} \rightarrow 33t_{1g}$
52 T_{1u}	2453.44	$6.984 \cdot 10^{-3}$	47% $1e_u \rightarrow 33t_{1g}$ 38% $1t_{1u} \rightarrow 33t_{1g}$ 11% $2t_{1u} \rightarrow 33t_{1g}$
55 T_{1u}	2453.59	$4.126 \cdot 10^{-3}$	47% $1t_{2g} \rightarrow 38t_{2u}$ (Au: 6s 18% 6p 8%, S: 3p 27% 3d 10%) 43% $1e_g \rightarrow 38t_{2u}$ 6% $1t_{1g} \rightarrow 38t_{2u}$
56 T_{1u}	2453.59	$8.308 \cdot 10^{-3}$	33% $2t_{2g} \rightarrow 38t_{2u}$ 26% $1t_{1g} \rightarrow 38t_{2u}$ 23% $1e_g \rightarrow 38t_{2u}$ 16% $1t_{2g} \rightarrow 38t_{2u}$

65	T _{1u}	2453.76	1.030*10 ⁻²	37% 1t _{1g} → 39t _{2u} (Au: 6s 24%, S: 3p 26%, 3d 16%) 31% 2t _{2g} → 39t _{2u} 15% 1t _{2g} → 39t _{2u} 10% 1e _g → 39t _{2u}
68	T _{1u}	2453.81	7.160*10 ⁻³	40% 2t _{1u} → 35e _g (Au: 6s 11% 6p 33%, S: 3p 14% 3d 21%) 28% 1t _{1u} → 35e _g 23% 1t _{2u} → 35e _g
78	T _{1u}	2454.04	6.474*10 ⁻³	94% 1t _{2u} → 11a _{2g} (Au: 6s 27%, S: 3p 28%, 3d 16%)
86	T _{1u}	2454.34	4.053*10 ⁻³	62% 1e _u → 46t _{2g} (Au: 6p 16%, C: 2p 20%, S: 3p 26% 3d 9% 4d 10%) 28% 1a _{2u} → 46t _{2g} 7% 1t _{2u} → 46t _{2g}
94	T _{1u}	2454.67	3.812*10 ⁻³	37% 1e _g → 54t _{1u} (Au: 6s 9% 6p 8%, C: 2p 22%, S: 3p 26%, H: 1s 8% 2s 10%) 31% 1a _{1g} → 54t _{1u} 23% 2t _{2g} → 54t _{1u}
98	T _{1u}	2454.77	5.578*10 ⁻³	90% 1t _{2g} → 23e _u (C: 2p 23%, S: 3p 44% 4d 11%, H: 2s 8%)
117	T _{1u}	2455.16	3.134*10 ⁻³	18% 2t _{2g} → 41t _{2u} (Au: 6p 21%, C: 2p 18%, S: 3p 25% 3d 14%) 17% 1t _{1g} → 41t _{2u} 16% 1t _{1g} → 55t _{1u} (Au: 6p 15%, C: 2p 26%, S: 3p 23%, H: 1s 19% 2s 18%) 14% 2t _{2g} → 55t _{1u}
122	T _{1u}	2455.20	1.064*10 ⁻²	32% 1t _{1g} → 55t _{1u} 26% 2t _{2g} → 55t _{1u}
123	T _{1u}	2455.20	3.754*10 ⁻³	27% 1t _{2g} → 55t _{1u} 21% 1a _{1g} → 55t _{1u}
139	T _{1u}	2455.54	9.476*10 ⁻³	45% 1t _{2u} → 35t _{1g} (Au: 6p 20%, C: 2p 27%, S: 3p 31%) 35% 2t _{1u} → 35t _{1g} 11% 1t _{1u} → 35t _{1g}
152	T _{1u}	2455.68	5.914*10 ⁻³	44% 1e _u → 49t _{2g} (Au: 6p 13%, C: 2p 21%, S: 3p 17%, H: 1s 26% 2s 31%) 25% 1t _{2u} → 49t _{2g} 10% 1a _{2u} → 49t _{2g}
155	T _{1u}	2455.70	2.108*10 ⁻³	41% 2t _{2g} → 42t _{2u} (Au: 6p 10%, S: 3d 11% 4s 19%, H: 1s 35% 2s 46%) 37% 1t _{1g} → 42t _{2u}
156	T _{1u}	2455.70	2.986*10 ⁻³	41% 1t _{2g} → 42t _{2u} 37% 1e _g → 42t _{2u}
275	T _{1u}	2457.50	1.509*10 ⁻³	59% 2t _{1u} → 55t _{2g} (Au: 6p 22%, C: 2p 10% 3p 16%, S: 3d 14% 4p 29%) 22% 1a _{2u} → 55t _{2g} 17% 1t _{2u} → 55t _{2g}
288	T _{1u}	2457.74	1.623*10 ⁻³	61% 1e _u → 56t _{2g} (C: 3p 11%, S: 4p 64% 5s 20%) 26% 1a _{2u} → 56t _{2g} 11% 1t _{2u} → 56t _{2g}
292	T _{1u}	2457.76	1.364*10 ⁻³	48% 1t _{1g} → 48t _{2u} (C: 3p 18%, S: 3d 18% 4p 70%, H: 1s 18%) 43% 2t _{2g} → 48t _{2u}
319	T _{1u}	2458.06	2.177*10 ⁻³	44% 2t _{1u} → 42e _g (Au: 6s 13% 6p 16%, S: 4p 34%) 31% 1t _{1u} → 42e _g 25% 1t _{2u} → 42e _g

Table 7.4 T_{1u} core S 1s excitation spectrum of [Au₁₄(AuSCH₃)₄]₆²⁺. Excitation energy (E_{exc}), oscillator strength (f) and excited state composition in terms of monoexcited configurations are reported. Only the most intense excitations, whose oscillator strength is f > 1.0 · 10⁻³ are reported.

8. CONCLUSIONS

During these three years of Ph. D. gold clusters in different situations and environments have been studied.

The main topic is the study of optical properties of gold nanoparticles through the TDDFT theory applied to electronic spectroscopy. The results obtained have shown that within the efficient parallel implementation of the ADF code this theory is a valuable investigative tool for nanoparticles allowing both the simulation and the interpretation of absorption phenomena. With our work we wanted to test and optimize computational schemes that have proven competitive. We have been able to study the core and valence absorption with both scalar and spin-orbit formalism on systems functionalized with ligands, pure and bi-metal systems, respectively, and to reach sizes that are close to those of the smallest real nanoparticles.

We can say that now there is a computational limit: the large size ($> 1\text{nm}$). Introduction of new improvements in the TDDFT algorithm would be welcome if much longer clusters are to be considered in the future. Nevertheless, the good versatility of the computational schemes explored in this thesis makes them good candidates for new applications in the field.

BIBLIOGRAPHY

Chapter 1

- ^{1.1} Li, J.; Li, X.; Zhai, H.-J.; Wang, L.-S. *Science* **2003**, 299, 864-867.
- ^{1.2} Woehrle, G. H.; Warner, M. G.; Hutchison, J. E. *J. Phys. Chem. B* **2002**, 106(39), 9979-9981.
- ^{1.3} Burda, C.; Chen, X.; Narayanan, R.; El-Sayed, M. A. *Chem. Rev.* **2005**, 105(4), 1025-1102.
- ^{1.4} Spivey, K.; Williams, J. I.; Wang, L. *Chem. Phys. Lett.* **2006**, 432, 163-166.
- ^{1.5} Palpant, B.; Prével, B.; Lermé, J.; Cottancin, E.; Pellarin, M.; Treilleux, M.; Perez, A.; Vialle, J. L.; Broyer, M. *Phys. Rev. B* **1998**, 57(3), 1963-1970.
- ^{1.6} Zhang, J. Z.; Noguez, C. *Plasm.* **2008**, 3(4), 127-150.
- ^{1.7} Zhang, P.; Sham, T. K. *Phys. Rev. Lett.* **2003**, 90, 245502 1-4.
- ^{1.8} Yamamoto, Y.; Miura, T.; Suzuki, M.; Kawamura, N.; Miyagawa, H.; Nakamura, T.; Kobayashi, K.; Teranishi, T.; Hori, H. *Phys. Rev. Lett.* **2004**, 93(11), 116801.
- ^{1.9} Nobusada, K. *J. Phys. Chem. B* **2004**, 108(32), 11904-11908.
- ^{1.10} Ikeda, K.; Kobayashi, Y.; Negishi, Y.; Seto, M.; Iwasa, T.; Nobusada, K.; Tsukuda, T.; Kojima, N. *J. Am. Chem. Soc.* **2007**, 129, 7230-7231.
- ^{1.11} Iwasa, T.; Nobusada, K. *J. Phys. Chem. C* **2007**, 111(1), 45-49.
- ^{1.12} Zhang, P.; Sham, T. K. *Phys. Rev. Lett.* **2003**, 90 (24), 245502.
- ^{1.13} Crespo, P.; Litrán, R.; Rojas, T. C.; Multigner, M.; de la Fuente, J. M.; Sánchez-López, J. C.; García, M. A.; Hernando, A.; Penadés, S.; Fernández, A. *Phys. Rev. Lett.* **2004**, 93 (8), 087204.
- ^{1.14} Schwerdtfeger, P. *Heteroatom Chem.* **2002**, 13 (6), 578-584.
- ^{1.15} Häkkinen, H.; Moseler, M.; Landman, U.; *Phys. Rev. Lett.* **2002**, 89 (3), 033401.
- ^{1.16} Pyykkö, P. *Angew. Chem. Int. Ed.* **2004**, 43, 4412-4456.

Chapter 2

- ^{2.1} Noguez, C. *J. Phys. Chem. C* **2007**, 111(10), 3806-3819.
- ^{2.2} Hollas, J. M. *Modern Spectroscopy*, J. Wiley & Sons, ed. (World Scientific, England,

- 1999) p. 175.
- ^{2.3} Ögüt, S.; Idrobo, J. C.; Jellinek J.; Wang, J. *J. Cl. Sc.* **2006**, *17(4)*, 609-626.
- ^{2.4} Schwarz, W. H. *Angew. Chem. internat, Edit.* **1974**, *13 (7)*, 454.
- ^{2.5} De Francesco, R. *Ph.D. thesis*, University of Trieste, **2007**, Fronzoni, G..
- ^{2.6} Stör, J. *NEXAFS spectroscopy*, Springer Series in Surface Sciences, Vol. 25, Springer-Verlag, Berlin – New York, **1992**.
- ^{2.7} Bianconi, A. *X-ray absorption: principles, applications, techniques of EXAFS, SEXAFS and XANES*, Koningsberger D. C., Prins R. (Eds.), John Wiley, New York, **1988**, p. 573.
- ^{2.8} Bianconi, A.; Garcia, J.; Benfatto, M. *Synchrotron radiation in chemistry and biology. 1*, Topics in Current Chemistry, Vol. 145, Mandelkow E., Bazin D. (Eds.), Springer-Verlag, Berlin Heidelberg, **1988**, p. 29.

Chapter 3

- ^{3.1} van Gisbergen, S. J. A. *Ph.D. thesis*, University of Vrije, **1998**, Snijders, J. G.; Baerends, E. J..
- ^{3.2} Parr, R. G.; Yang, W. *Density-functional theory of atoms and molecules*, Oxford University Press, New York, **1989**.
- ^{3.3} Hohenberg, P.; Kohn, W. *Phis. Rev. B* **1964**, *136*, 864.
- ^{3.4} Levy, M. *Proc. Natl. Acad. USA* **1979**, *76*, 6062.
- ^{3.5} van Gisbergen, S. J. A.; Snijders, J. G.; Baerends, E. J. *Comp. Phys. Comm.* **1999**, *118*, 119-138.
- ^{3.6} De Francesco, R. *Ph.D. thesis*, University of Trieste, **2007**, Fronzoni, G..
- ^{3.7} Gross, E. K. U.; Kohn, W. *Adv. Quantum. Chem.* **1990**, *21*, 255.
- ^{3.8} Görling, A. *Phys. Rev. A* **1996**, *54*, 3912.
- ^{3.9} Görling, A. *Phys. Rev. Lett.* **2000**, *85*, 4229.
- ^{3.10} Casida, M. E. *Recent Advances in Density-Functional Methods*, D. P. Chong, ed. (World Scientific, Singapore, **1995**) p. 155.
- ^{3.11} Stener, M.; Fronzoni, G.; de Simone, M. *Chem. Phys. Lett.* **2003**, *373*, 115.
- ^{3.12} Te Velde, G.; Bickelhaupt, F. M.; Baerends, E. J.; Fonseca Guerra, C.; van Gisbergen, S. J. A.; Snijders, J. G.; Ziegler, T. *J. Comput. Chem.* **2001**, *22 (9)*, 931-967.
- ^{3.13} Wang, F.; Ziegler, T.; van Lenthe, E.; van Gisbergen, S.; Baerends, E.J. *J. Chem. Phys.* **2005**, *122 (20)*, 204103.

- 3.14 Davidson, E. R. *J. Comput. Phys.* **1975**, *17*, 87.
- 3.15 van Lenthe, E.; Baerends, E. J. *J. Comput. Chem.* **2006**, *24* (9), 1142-1156.

Chapter 4

- 4.1 Burda, C.; Chen, X.; Narayanan, R.; El-Sayed, M. A. *Chem. Rev.* **2005**, *105*, 1025-1102.
- 4.2 Sau, T. K.; Murphy, C. J. *Langmuir* **2004**, *20*, 6414-6420.
- 4.3 Nikoobakht, B.; El-Sayed, M. A. *Chem. Mater.* **2003**, *15*, 1957-1962.
- 4.4 Tsunoyama, H.; Nickut, P.; Negishi, Y.; Al-Shamery, K.; Matsumoto, Y.; Tsukuda, T. *J. Phys. Chem. C* **2007**, *111*, 4153-4158.
- 4.5 Price, R. C.; Whetten, R. L. *J. Am. Chem. Soc.* **2005**, *127*, 13750-13751.
- 4.6 Noguez, C.; *J. Phys. Chem. C* **2007**, *111*, 3806-3819.
- 4.7 Kunz, K. S.; Luebbers, R. J. *The Finite Difference Time Domain Method for Electromagnetics*, CRC Press, LLC, Boca Raton, **1993**, pp.123–162.
- 4.8 Draine, B. T.; Flatau, P.J. *J Opt Soc Am A—Opt Image Sci Vis* **1994**, *11*, 1491–1499.
- 4.9 Palpant, B.; Prével, B.; Lermé, J.; Cottancin, E.; Pellarin, M.; Treilleux, M.; Perez, A.; Vialle, J. L.; Broyer, M. *Phys. Rev. B* **1998**, *57*, 1963-1970.
- 4.10 Prodan, E.; Nordlander, P.; Halas, N. J.; *Chem. Phys. Lett.* **2003**, *368*, 94-101.
- 4.11 Nobusada, K. *J. Phys. Chem. B* **2004**, *108*, 11904-11908.
- 4.12 Iwasa, T.; Nobusada, K. *J. Phys. Chem. C* **2007**, *111*, 45-49.
- 4.13 Häkkinen, H.; Walter, M.; Grönbeck, H. *J. Phys. Chem. B* **2006**, *110*, 9927-9931.
- 4.14 Wang, F.; Ziegler, T. *J. Chem. Phys.* **2004**, *121*, 12191-12196.
- 4.15 Li, J.; Li, X.; Zhai, H.-J.; Wang, L.-S. *Science* **2003**, *299*, 864-867.
- 4.16 Wu, K.; Li, J.; Lin, C; *Chem. Phys. Lett.* **2004**, *388*, 353-357.
- 4.17 Baerends, E. J.; Ellis, D. E.; Ros, P. *Chem. Phys.* **1973**, *2*, 41-51.
- 4.18 Fonseca Guerra, C.; Snijders, J. G.; te Velde, G.; Baerends, E. J.; *Theor. Chem. Acc.* **1998**, *99*, 391-403.
- 4.19 Pyykkö, P. *Angew. Chem. Int. Ed.* **2004**, *43*, 4412-4456.
- 4.20 van Lenthe, E.; Baerends, E. J.; Snijders, J. G. *J. Chem. Phys.* **1993**, *99*, 4597-4610.
- 4.21 van Gisbergen, S. J. A.; Snijders, J. G.; Baerends, E. J. *Comp. Phys. Comm.* **1999**, *118*, 119-138.
- 4.22 Casida, M. E. *Recent Advances in Density-Functional Methods*, D. P. Chong, ed. (World Scientific, Singapore, **1995**) p. 155.

- ^{4.23} Gross, E. K. U.; Kohn, W. *Adv. Quantum. Chem.* **1990**, *21*, 255-291.
- ^{4.24} Parr, R. G.; Yang, W. *Density Functional Theory of Atoms and Molecules*, Oxford University Press, New York **1989**.
- ^{4.25} Vosko, S. H.; Wilk, L.; Nusair, M. *Can. J. Phys.* **1980**, *58*, 1200-1211.
- ^{4.26} Häberlen, O.; Chung, S. C.; Stener, M.; Rösch, N. *J. Chem. Phys.* **1997**, *106*, 5189-5201.
- ^{4.27} Van Leeuwen, R.; Baerends E. J. *Phys. Rev. A* **1994**, *49*, 2421-2431.
- ^{4.28} Schipper, P. R. T.; Gritsenko, O. V.; van Gisbergen, S. J. A.; Baerends, E. J. *J. Chem. Phys.* **2000**, *112*, 1344-1352.
- ^{4.29} van Gisbergen, S. J. A.; Kootstra, F.; Schipper, P. R. T.; Gritsenko, O. V.; Snijders J. G.; Baerends, E. J.; *Phys. Rev. A* **1998**, *57*, 2556-2571.
- ^{4.30} Grüning, M.; Gritsenko, O.V.; van Gisbergen, S.J.A.; Baerends, E. J. *J. Chem. Phys.* **2001**, *114*, 652-660.
- ^{4.31} Serra, L.; Rubio, A. *Phys. Rev. Lett.* **1997**, *78*, 1428-1431.
- ^{4.32} Cleveland, C. L.; Landman, U.; Shafigullin, M. N.; Stephens, P. W.; Whetten, R. L. *Zeit. Physik D* **1997**, *40*, 503-508.
- ^{4.33} Spivey, K.; Williams, J. I.; Wang, L.; *Chem. Phys. Lett.* **2006**, *432*, 163-166.
- ^{4.34} Garzón, I. L.; Rovira, C.; Michaelian, K.; Beltrán, M. R.; Ordejón, P.; Junquera, J.; Sánchez-Portal, D.; Artacho, E.; Soler, J. M. *Phys. Rev. Lett.* **2000**, *85*, 5250-5251.
- ^{4.35} Collings, B. A.; Athanassenas, K.; Lacombe, D.; Rayner, D. M.; Hackett, P. A. *J. Chem. Phys.* **1994**, *101*, 3506-3513.
- ^{4.36} Schaaff, T. G.; Shafigullin M. N.; Khoury J. T.; Vezmar I.; Whetten R. L. *J. Phys. Chem. B* **2001**, *105*, 8785-8796.
- ^{4.37} Schaaff, T. G.; Shafigullin M. N.; Khoury J. T.; Vezmar I.; Whetten R. L.; Cullen W. G.; First P. N.; Gutiérrez-Wing C.; Ascensio J.; Jose-Yacamán M. J. *J. Phys. Chem. B* **1997**, *101*, 7885-7891.
- ^{4.38} Alvarez, M. M.; Khourny, J. T.; Schaaff T. G.; Shafigullin, M. N.; Vezmar, I.; Whetten, R. L. *J. Phys. Chem. B* **1997**, *101*, 3706-3712.
- ^{4.39} Walker, B.; Saitta, A. M.; Gebauer, R.; Baroni, S. *Phys. Rev. Lett.* **2006**, *96*, 113001 1-4.
- ^{4.40} Görling, A.; Heinze, H. H.; Ruzankin, S. Ph.; Staufer, M.; Rösch, N. *J. Chem. Phys.* **1999**, *110*, 2785-2799.

Chapter 5

- 5.1 *Gold. Progress in Chemistry, Biochemistry and Technology* (Ed.: H. Schmidbaur) **1999**, Wiley, Chichester.
- 5.2 Pyykkö, P. *Angew. Chem. Int. Ed.* **2004**, *43*, 4412.
- 5.3 Aprà, E.; Ferrando, R.; Fortunelli, A. *Phys. Rev. B* **2006**, *73*, 205414.
- 5.4 Schmidbaur, H. *Gold Bull.* **1990**, *23*, 11.
- 5.5 Scherbaum, F.; Grohmann, A.; Huber, B.; Krüger, C.; Schmidbaur, H. *Angew. Chem, Int. Ed. Engl.* **1988**, *27*, 1544.
- 5.6 Häberlen, O. H.; Schmidbaur, H.; Rösch, N. *J. Am. Chem. Soc.* **1994**, *116*, 8241.
- 5.7 Pyykkö, P.; Runeberg, N. *Angew. Chem. Int. Ed.* **2002**, *41*, 2174.
- 5.8 Li, X.; Kiran, B.; Li, J.; Zhai, H.-J.; Wang, L.-S. *Angew. Chem. Int. Ed.* **2002**, *41*, 4786.
- 5.9 Shichibu, Y.; Negishi, Y.; Watanabe, T.; Chaki, N. K.; Kawaguchi, H.; Tsukuda, T. *J. Phys. Chem. C* **2007**, *111*, 7845.
- 5.10 Burda, C.; Chen, X.; Narayanan, R.; El-Sayed, M. A. *Chem. Rev.* **2005**, *105*, 1025.
- 5.11 Pyykkö, P.; Desclaux, J. P. *Acc. Chem. Res.* **1979**, *12*, 276.
- 5.12 Gagliardi, L.; Roos, B. O. *Nature* **2005**, *433*, 848.
- 5.13 Wang, F.; Ziegler, T.; van Lenthe, E.; van Gisbergen, S.; Baerends, E. J. *J. Chem. Phys.* **2005**, *122*, 204103.
- 5.14 Casida, M. E. *Recent Advances in Density-Functional Methods*, D. P. Chong, ed. (World Scientific, Singapore, **1995**) p. 155
- 5.15 van Gisbergen, S. J. A.; Snijders, J. G.; Baerends, E. J. *J. Chem. Phys.* **1999**, *118*, 19.
- 5.16 Guerra, C. F.; Snijders, J. G.; te Velde, G.; Baerends, E. J. *Theor. Chemm. Acc.* **1998**, *99*, 391.
- 5.17 Van Leeuwen, R.; Baerends, E. J. *Phys. Rev. A* **1994**, *49*, 2421.
- 5.18 van Gisbergen, S. J. A ; Osinga, V. P.; Gritsenko, O. V.; van Leeuwen, R.; Snijders, J. G.; Baerends, E. J. *J. Chem. Phys.* **1996**, *105*, 3142.
- 5.19 Schipper, P. R. T.; Gritsenko, O. V.; van Gisbergen, S. J. A.; Baerends, E. J. *J. Chem. Phys.* **2000**, *112*, 1344.
- 5.20 Stener, M.; Nardelli, A.; De Francesco, R.; Fronzoni, G. *J. Phys. Chem. C* **2007**, *111*, 11862.
- 5.21 Pierloot, K.; van Besien, E.; van Lenthe, E.; Baerends, E. J. *J. Chem. Phys.* **2007**, *126*, 194311.
- 5.22 Yanai, T.; Tew, D. P.; Handy, N. C. *Chem. Phys. Lett.* **2004**, *393*, 51.

- 5.23 Kobayashi, R.; Amos, R. D. *Chem. Phys. Lett.* **2006**, 420, 106.
- 5.24 Autschbach, J.; Hess, B. A.; Johansson, M. P.; Neugebauer, J.; Patzschke, M.; Pyykkö, P.; Reiher, M.; Sundholm, D. *Chem. Phys.* **2004**, 6, 11.
- 5.25 Balasubramanian, K. *Chem. Phys. Lett.* **1996**, 260, 476.
- 5.26 Görling, A. *Int. J. of Quantum Chem.* **1998**, 69, 265.
- 5.27 Casida, M. E. *J. Chem. Phys.* **2005**, 122, 054111.

Chapter 6

- 6.1 *Gold. Progress in Chemistry, Biochemistry and Technology* (Ed.: H. Schmidbaur) **1999**, Wiley, Chichester.
- 6.2 Pyykkö, P. *Angew. Chem. Int. Ed.* **2004**, 43, 4412.
- 6.3 Schmidbaur, H. *Gold Bull.* **1990**, 23, 11.
- 6.4 Scherbaum, F.; Grohmann, A.; Huber, B.; Krüger, C.; Schmidbaur, H. *Angew. Chem, Int. Ed. Engl.* **1988**, 27, 1544.
- 6.5 Häberlen, O. H.; Schmidbaur, H.; Rösch, N. *J. Am. Chem. Soc.* **1994**, 116, 8241.
- 6.6 Nobusada, K. *J. Phys. Chem. B* **2004**, 108, 11904.
- 6.7 Pyykkö, P.; Runeberg, N. *Angew. Chem. Int. Ed.* **2002**, 41, 2174.
- 6.8 Li, X.; Kiran, B.; Li, J.; Zhai, H.-J.; Wang, L.-S. *Angew. Chem. Int. Ed.* **2002**, 41, 4786.
- 6.9 Zhai, H.-J.; Li, J.; Wang, L.-S. *J. Chem. Phys.* **2004**, 121, 8369.
- 6.10 Stener, M.; Nardelli, A.; Fronzoni, G. *J. Chem. Phys.* **2008**, 128, 134307.
- 6.11 Wang, F.; Ziegler, T.; van Lenthe, E.; van Gisbergen, S.; Baerends, E. J. *J. Chem. Phys.* **2005**, 122, 204103.
- 6.12 Casida, M. E. *Recent Advances in Density-Functional Methods*, D. P. Chong, ed. (World Scientific, Singapore, **1995**) p. 155
- 6.13 Noguez, C. *J. Phys. Chem. C* **2007**, 111, 3806.
- 6.14 Aikens, C. M.; Li, S.; Schatz, G. C. *J. Phys. Chem. C* **2008**, 000, 0000 (in press), ASAP Article; DOI: [10.1021/jp802707r](https://doi.org/10.1021/jp802707r)
- 6.15 Perdew, J. P.; Wang, Y. *Phys. Rev. B* **1992**, 45, 13244.
- 6.16 Perdew, J. P.; Chevary, J. A.; Vosko, S. H.; Jackson, K. A.; Pederson, M. R.; Singh, D. J.; Foilhais, C. *Phys. Rev. B* **1992**, 46, 6671.
- 6.17 Balasubramanian, K. *Chem. Phys. Lett.* **1996**, 260, 476.
- 6.18 Van Leeuwen, R.; Baerends, E. J. *Phys. Rev. A* **1994**, 49, () 2421.

- ^{6.19} van Gisbergen, S. J. A.; Osinga, V. P.; Gritsenko, O. V.; van Leeuwen, R.; Snijders J. G.; Baerends, E. J. *J. Chem. Phys.* **1996**, *105*, 3142.
- ^{6.20} Stener, M.; Fronzoni, G.; Decleva, P. *J. Chem. Phys.* **2005**, *122*, 234301.

Chapter 7

- 7.1 Burda, C.; Chen, X.; Narayanan, R.; El-Sayed, M. A. *Chem. Rev.* **2005**, *105*, 1025-1102.
- 7.2 Sau, T. K.; Murphy, C. J. *Langmuir* **2004**, *20*, 6414-6420.
- 7.3 Nikoobakht, B.; El-Sayed, M. A. *Chem. Mater.* **2003**, *15*, 1957-1962.
- 7.4 Tsunoyama, H.; Nickut, P.; Negishi, Y.; Al-Shamery, K.; Matsumoto, Y.; Tsukuda, T. *J. Phys. Chem. C* **2007**, *111*, 4153-4158.
- 7.5 Price, R. C.; Whetten, R. L. *J. Am. Chem. Soc.* **2005**, *127*, 13750-13751.
- 7.6 Zhang, P.; Sham, T. K. *Phys. Rev. Lett.* **2003**, *90*, 245502 1-4.
- 7.7 Zhang, P.; Sham, T. K. *Appl. Phys. Lett.* **2002**, *81*, 736.
- 7.8 van Lenthe, E.; Baerends, E. J.; Snijders, J. G. *J. Chem. Phys.* **1993**, *99*, 4597-4610.
- 7.9 Pyykkö, P. *Angew. Chem. Int. Ed.* **2004**, *43*, 4412-4456.
- 7.10 Baerends, E. J.; Ellis, D. E.; Ros, P. *Chem. Phys.* **1973**, *2*, 41-51.
- 7.11 Fonseca Guerra, C.; Snijders, J. G.; te Velde, G.; Baerends, E. J.; *Theor. Chem. Acc.* **1998**, *99*, 391-403.
- 7.12 van Gisbergen, S. J. A.; Snijders, J. G.; Baerends, E. J. *Comp. Phys. Comm.* **1999**, *118*, 119-138.
- 7.13 Casida, M. E. *Recent Advances in Density-Functional Methods*, D. P. Chong, ed. (World Scientific, Singapore, **1995**) p. 155.
- 7.14 Gross, E. K. U.; Kohn, W. *Adv. Quantum. Chem.* **1990**, *21*, 255-291.
- 7.15 Stener, M.; Fronzoni, G.; De Simone, M. *Chem. Phys. Lett.* **2003**, *373*, 115.
- 7.16 Perdew J. P.; Wang Y. *Phys. Rev. B* **1992**, *45*, 13244.
- 7.17 Perdew, J. P.; Chevary, J. A.; Vosko, S. H.; Jackson, K. A.; Pederson, M. R.; Singh, D. J.; Foilhais, C. *Phys. Rev. B* **1992**, *46*, 6671.
- 7.18 Van Leeuwen, R.; Baerends E. J. *Phys. Rev. A* **1994**, *49*, 2421-2431.
- 7.19 van Gisbergen, S. J. A.; Kootstra, F.; Schipper, P. R. T.; Gritsenko, O. V.; Snijders J. G.; Baerends, E. J.; *Phys. Rev. A* **1998**, *57*, 2556-2571.
- 7.20 Nobusada, K. *J. Phys. Chem. B* **2004**, *108*, 11904-11908.

- 7.21 Iwasa, T.; Nobusada, K. *J. Phys. Chem. C* **2007**, *111*, 45 - 49.
- 7.22 Häkkinen, H.; Walter, M.; Grönbeck, H. *J. Phys. Chem. B* **2006** *110* 9927 - 9931.
- 7.23 Jiang, D.; Luo, W.; Tiago, M. L.; Dai, S. *J. Phys. Chem. C* **2008** *112* 13905 - 13910.
- 7.24 Pei, Y.; Gao, Y.; Zeng, X. C. *J. Am. Chem. Soc.* **2008**, *130*, 7830 - 7832

Ringraziamenti

Arrivati alla conclusione di una tesi che coincide con quella di un ciclo di studi, sembra “doveroso” passare ai ringraziamenti. Ecco, in questo caso, i ringraziamenti sono tutt’altro che “doverosi”!

Solo grazie all’aiuto e al contributo prezioso del mio relatore, Mauro Stener (dovrei dire prof., ma non viene spontaneo, avendo instaurato da subito un rapporto lavorativo “a tu per tu”), ho potuto avvicinarmi e apprezzare qualche aspetto di quella che viene ritenuta la branca più ostica e oscura della chimica. Grazie alla tua presenza costante, alla tua pazienza, alla tua capacità di spiegare e insegnare in modo chiaro e comprensibile, ho avuto l’opportunità di studiare e di appassionarmi, più del previsto!, ad argomenti molto distanti dalla mia formazione universitaria.

E che dire del mio “collega crodigo” per eccellenza? GRAZIE Renato!! sei stato il mio primo collega, quello che sarà davvero insostituibile: i tuoi consigli, le tue spiegazioni, il tuo supporto tecnico e morale, nonché la tua amicizia e simpatia, hanno reso questi tre anni di dottorato un’esperienza di vita ed un percorso formativo che ricorderò con entusiasmo (ed è anche per “colpa tua” che il distacco da qui è più duro di quello che avrei immaginato!).

Grazie infinite a tutte le persone che qui, al C11, ho conosciuto e con le quali ho condiviso momenti divertenti e spensierati (pause caffè, pranzi in osmiza, aperitivi, feste di compleanno, di laurea, di dottorato, partite di calcio...)...menzionandone solo alcune...il Gontino, la Cristy, la piccola Mary, il Pi, il Franzete, Alice, Simone, Rug, Ulma, Daniele...e tutti gli altri! Grazie a tutti quelli che mi hanno sempre salutato col sorriso e con cordialità: dai docenti e i ricercatori del gruppo di chimica-fisica (in particolare Giovanna Fronzoni e Sonia Coriani), a quelli degli altri gruppi, agli studenti. Posso affermare che ho respirato un’aria distesa e gioviale in un edificio non proprio “confortevole” (macchinetta del caffè a parte!).

Spostandoci all’esterno, il mio grazie va in primis alla mia famiglia (la mia pupetta, i miei e le nonne), che ha appoggiato e sostenuto la scelta del proseguimento degli studi, alla mia stellina Cri, la cui amicizia è stata fondamentale, alla band della palestra (il caro Lorenz, Manu, Max, Carmine, Roby, Diego, Micky,...) con cui ho condiviso momenti e serate allegre e divertenti, scoprendo e riscoprendo affetti veri. Grazie alle mie ex-compagne di corso, ma amiche presenti, Silvia, Lor e Silvietta, grazie a Elena, Ragno, Sandro e a chi all’epoca aveva creduto in me e che, nonostante tutto, è stato sempre presente.

E l’ultimo grazie a me, perché, finalmente, HO FINITO di ringraziare!